Engineering Porous Electrodes for Advanced Redox Flow Batteries

Liu, Baichen

Publication date:
2023

Document Version
Publisher's PDF, also known as Version of record

Citation (APA):
Liu, B. (2023). *Engineering Porous Electrodes for Advanced Redox Flow Batteries*. Technical University of Denmark.

Engineering Porous Electrodes for Advanced Redox Flow Batteries

Ph.D. Thesis

By Baichen Liu

October, 2023

Section of Low Temperature Electrochemistry
Department of Energy Conversion and Storage
Technical University of Denmark

Author

Baichen Liu
Department of Energy Conversion and Storage
Technical University of Denmark
E-mail: baili@dtu.dk

Supervisor

Professor: Johan Hjelm
Department of Energy Conversion and Storage
Technical University of Denmark
E-mail: johh@dtu.dk

Co-Supervisors

Senior Researcher: Søren Bredmose Simonsen
Department of Energy Conversion and Storage
Technical University of Denmark
E-mail: sobrs@dtu.dk

Associate Professor: Antoni Forner-Cuenca
Department of Chemical Engineering and Chemistry
Eindhoven University of Technology
E-mail: a.forner.cuenca@tue.nl

Department of Energy Conversion and Storage
Technical University of Denmark
Anker Engelunds Vej
Building 310
2800 Kongens Lyngby, Denmark
Phone +45 46 77 58 00
www.energy.dtu.dk

Preface

This thesis is submitted in candidacy for the PhD degree from Technical University of Denmark (DTU). The work was carried out at the Department of Energy Conversion and Storage from October 2020 to September 2023 under the supervision of Professor Johan Hjelm, and the co-supervision of Senior researcher Søren Bredmose Simonsen, and Associate Professor Antoni Forner-Cuenca. Part of the work was carried out at the Department of Chemical Engineering and Chemistry in Eindhoven University of Technology (from October 2022 to March 2023) during the Ph.D. external stay under the supervision of Associate Professor Antoni Forner-Cuenca. The Ph.D. project was partially supported by EUDP through RED-BATS (project no 64020-2095) and by Innovation Fund Denmark through DanFlow (file no. 9090-00059B). The external stay was funded by the travel grants from DTU Beyond Borders and Otto Mønsted Fonden.

Baichen Liu

Baichen Liu

October 2023, Kongens Lyngby, Denmark

Acknowledgements

I would like to express my profound gratitude to those who contributed to this thesis and my Ph.D. project over the past three years.

First and foremost, I would like to thank my principal supervisor, Johan Hjelm, for his unwavering support over the past three years. I appreciate the opportunity to join the flow battery group and initiate explorations in the field of electrochemistry. Johan's consistent encouragement, cheerful disposition, and resourcefulness have been invaluable, especially during challenging periods in my research.

Similar gratitude goes out to my co-supervisors, Søren Bredmose Simonsen and Antoni Forner-Cuenca. Thanks Søren for his invaluable feedback and engagement in this process. His insights, especially concerning X-ray computed tomography, have enhanced my research quality. Thanks Antoni for facilitating my external stay, which led to an enriching six-month experience at Eindhoven University of Technology in the Netherlands. His enthusiasm and in-depth knowledge, particularly about phase separation techniques, significantly enriched my thesis.

My heartfelt gratitude goes to my colleagues at DTU Energy who played a pivotal role in my journey. I owe special thanks to Salvatore De Angelis for his invaluable assistance with Lattice Boltzmann Methods, to Vedrana Andersen Dahl for her expertise in fiber orientation analysis, to Vanesa Muñoz for her support in COMSOL, to Mikkel Rykær Kraglund for his unwavering support in the laboratory. I'm also profoundly grateful to Jette Iversen, Berit Herstrøm, June Ruddie Flittner, Carsten Gundlach, Mike Wichmann, Andreas Franz-Josef Kaiser, Peter Lipman, Gerrit Fimerius or their significant contributions.

My colleagues at DTU have been integral to my journey. The flow battery group, including Alexandros, Mads, Mahsa, Doris, and David, alongside members of the LTE Section, have been pillars of support. Many thanks to the group members from EMS in TU/e during my external stay, including Rémy, Simona, Kiran, Emre, Mert, Inmaculada, Jesse, and Maxime. My experience at TU/e was made memorable by all of you. Specific thanks to my officemates, Thu, Sarmad, Elena, Nikola, Lisa, Franz, Mathias, and Jing-Jing, who added joy to my daily routines. I am grateful to all my friends and colleagues here, especially Shu, Kun, Yifan, Zhongtao, Gaoyuan, Zoe, Xingling, Sanser, Yi-Lin, Yichen, Raquel, Dmytro, William, Xiaosheng, Kai, Zhipeng, Hua, Yihao, Quan, Yijing, Haiwu, Lujin, Jiarui, Songyu, Hongying, Andreas, Paolo, David, Song, Jiawei, Yucheng, Yang, Wong, Kaihao, and others. Their friendship made Denmark feel even more special.

Concluding, I reserve my deepest gratitude for my family. Their faith and support have been the cornerstone throughout this doctoral journey.

Abstract

The escalating adoption of renewable energy sources underscores the pressing need for efficient and scalable energy storage systems to ensure consistent energy supply and grid stability. Within energy storage technologies, redox flow batteries have been regarded as promising solutions for stationary grid-scale energy storage. However, the path to their widespread commercialization has been restricted due to the high capital costs, and one of the key solutions to cost reduction lies in enhancing the battery performance.

Porous electrodes are crucial components of redox flow battery system, which are closely related to the reactor internal resistance and battery performance. The main focus of this thesis is the development of engineering porous electrodes with a balance between the active surface area and effective electrolyte transport pathways for advanced redox flow batteries. Efforts are devoted to three aspects: i) unveiling the relationship between the morphological properties and electrochemical performance of three distinct carbon-fiber electrodes, including carbon felt, carbon paper, and carbon cloth. Investigating the optimal compression condition for the three electrode in redox flow battery system; ii) developing a dual-layer electrode configuration to simultaneously meet the requirement of high active surface area and low mass transfer resistance; iii) Tailoring the electrode microstructure using non-solvent induced phase separation as well as integrating a micro-flow field into the electrode architecture for improved mass transfer performance.

First, the 3D electrode morphology of the three commercially available carbon-fiber electrodes was characterized through X-ray computed tomography at 0-50% compression ratios. The electrochemical performance was evaluated at the same compression range in a lab-scale full-cell vanadium redox flow battery. It was found that the cloth possessed a bimodal pore size distribution. However, its distinct microstructure and the associated advantageous mass transfer properties were deteriorated significantly at applied high compression (e.g., >30% compression ratios). The optimal trade-off between the pressure drop and the electrochemical performance occurs at the compression ratios of 30%, 20%, and 20% for the felt, paper, and cloth, respectively.

Secondly, the carbon cloth electrode was combined with a sub-layer consisting of carbon paper to assemble a dual-layer electrode configuration. Quantitative analysis of contributions from each type of polarization was investigated under both V^{2+}/V^{3+} and VO^{2+}/VO_2^+ redox couples in one-container symmetric cells with flow-through flow fields. The results showed that the proposed strategy was effective to obtain decreased overall kinetic and mass transport resistances. At the current density of 100 mA/cm^2, a decrease of ~35% and ~17% of the overall cell overpotential was achieved compared to single-layer carbon cloth and paper, respectively.

Finally, the non-solvent induced phase separation technique was used to fabricate tailored non-fibrous porous electrodes. Inspired by the flow field designs in redox flow batteries for low pressure drop and uniform electrolyte distribution, a strategy to imprint micro-patterned flow fields directly into the electrode architecture during the phase exchange process was explored. Two micro-patterned designs (i.e., groove and pillar patterns) were selected and the electrochemical measurements were conducted using the Fe^{2+}/Fe^{3+} redox couple in a symmetric cell. It was found that the pillar-patterned electrodes combined with an external interdigitated flow field showed the best performance. At an electrolyte velocity of 10 cm/s, the total resistances for kinetic and mass transfer are less than 0.1 $\Omega\cdot cm^2$ in symmetric iron cell tests, corresponding to a reduction of ~60% when comparing to the activated carbon paper electrode.

Resumé

Den voksende anvendelse af vedvarende energikilder understreger behovet for effektive og skalerbare energilagringsystemer for at sikre en konstant energiforsyning og netværksstabilitet. Inden for energilagringsteknologier betragtes redox flow-batterier som lovende løsninger til stationær netværksskala energilagring. Men vejen til deres udbredte kommercialisering har været begrænset på grund af de høje kapitalomkostninger, og en af de vigtige løsninger til omkostningsreduktion ligger i at forbedre batteriets ydeevne.

Poreelektroder er afgørende komponenter i redox flow-batterisystemet, som er tæt relateret til reaktorens interne modstand og batteriets ydeevne. Dette speciales primære fokus er udviklingen af ingeniørporøse elektroder med en balance mellem det aktive overfladeareal og effektive elektrolyttransportveje til avancerede redox flow-batterier. Der er gjort en indsats inden for tre aspekter: i) afsløring af forholdet mellem morfologiske egenskaber og elektrokemisk ydeevne af tre forskellige carbonfiber-elektroder, herunder carbonfilt, carbonpapir og carbonklud. Undersøgelse af den optimale kompressionstilstand for de tre elektroder i redox flow-batterisystemet; ii) udvikling af en dobbeltlags elektrodekonfiguration for samtidigt at opfylde kravet om højt aktivt overfladeareal og lav masstransportmodstand; iii) Tilpasning af elektrodens mikrostruktur ved hjælp af ikke-opløsningsinduceret faseseparation. Integration af mikrostrømningsfelt i elektrodens arkitektur for forbedret masstransport ydeevne.

For det første blev den 3D elektrode morfologi af de tre kommercielt tilgængelige carbonfiber-elektroder karakteriseret gennem røntgenberegnet tomografi ved 0-50% kompressionsforhold. Elektrokemisk ydeevne blev evalueret i samme kompressionsområde i et lab-skala full-cell vanadium redox flow-batteri. Det blev fundet, at kluden havde en bimodal porestørrelsesfordeling. Imidlertid blev dens distinkte mikrostruktur og de tilknyttede fordelagtige masstransportegenskaber begrænset ved anvendt høj kompression (f.eks. >30% kompressionsforhold). Den optimale afvejning mellem trykfald og elektrokemisk ydeevne forekom ved kompressionsforholdene 30%, 20% og 20% for filt, papir og klud, hhv.

For det andet blev carbonklud-elektroden kombineret med et sublag af carbonpapirelektrode for at samle en dobbeltlagselektrodekonfiguration. Kvantitativ analyse af bidrag fra hver type polarisering blev undersøgt under både V^{2+}/V^{3+} og VO^{2+}/VO_2^+ redox par i en-container symmetriske celler med flow-gennem strømningsfelter. Resultaterne viste, at den foreslåede strategi var effektiv til at opnå nedsat samlet kinetisk og masstransportmodstand. Ved en strømtæthed på 100 mA/cm^2 blev der opnået en nedgang på ~35% og ~17% af den samlede overpotentiale sammenlignet med enkeltlags carbonklud og papir, hhv.

Endelig blev ikke-opløsningsinduceret faseseparation anvendt til at fremstille skræddersyede ikke-fibrose porøse elektroder. Inspireret af strømningsfeltdesigns i redox flow-batterier for lavt trykfald og ensartet elektrolytdistribution blev en strategi til prægning af mikromønstrede strømningsfelter direkte i elektrodens arkitektur under faseskifteprocessen foreslået. To mikromønstrede designs (dvs. rille- og søjlemønstre) blev valgt til undersøgelse, og de elektrokemiske målinger blev udført under Fe^{2+}/Fe^{3+} redox par i en symmetrisk celle. Det blev fundet, at søjlemønstrede elektroder med kombinationen af interdigiterede strømningsfelter viste den bedste ydeevne. Ved en elektrolythastighed på 10 cm/s er de samlede modstande for kinetik og masstransport mindre end 0,1 $\Omega \cdot cm^2$ i symmetriske jerncelletest, hvilket blev reduceret med ~60% sammenlignet med det aktiverede carbonpapirelektrode.

List of Publications

[1] Baichen Liu, Søren Bredmose Simonsen, and Johan Hjelm. Morphological properties and electrochemical performance for carbon-fiber electrodes under varying compression ratios in redox flow batteries.
To be submitted

[2] Baichen Liu, Salvatore De Angelis, Vedrana Andersen Dahl, Søren Bredmose Simonsen, and Johan Hjelm. Electrochemical performance of dual-layer carbon electrodes in aqueous redox flow batteries.
To be submitted

[3] Baichen Liu, Vanesa Muñoz, Simona Buzzi, Rémy Richard Jacquemond, Johan Hjelm, and Antoni Forner-Cuenca. Integrating micro-flow fields into electrode architecture via non-solvent induced phase separation for high performance redox flow batteries.
To be submitted

Contribution to papers

Paper I	Participated in the formulation of the conceptual framework. Participated in the planning of the experiments. Performed experiments on X-ray computed tomography, electrochemical impedance spectroscopy and flow battery tests for three types of electrodes under 0-50% compression ratios. Main responsible for the manuscript writing.
Paper II	Participated in the planning of the electrochemical experiments in two symmetric cells. Performed data collection, analysis, and interpretation of the results. Assisted in the fiber orientation analysis, flow distribution simulations, and membrane characterization. Main responsible for the manuscript writing.
Paper II	Involved in the development of micro-flow field concepts in the NIPS electrodes. Participated in the execution of the electrochemical measurements, including iron symmetric and vanadium tests. Assisted in the COMSOL simulations and analysis of the results. Main responsible for the manuscript writing.

Contents

Acronyms

AC	Alternating current
ASR	Area specific resistance
BET	Brunauer-Emmett-Teller
CC	Carbon cloth
CE	Coulombic efficiency
CF	Carbon felt
CNLS	Complex nonlinear least squares
CP	Carbon paper
CPE	Constant phase element
CR	Compression ratio
CT	Computed tomography
DC	Direct current
DL	Dual layer
ECSA	Electrochemical specific surface area
EDLC	Electrochemical double layer capacitance
EE	Energy efficiency
EIS	Electrochemical impedance spectroscopy
EU	Electrolyte utilization ratio
FTFF	Flow-through flow field
GF	Graphite felt
IDFF	Interdigitated flow field
LBM	Lattice Boltzmann Method
MEA	Membrane electrode assembly
MIP	Mercury intrusion porosimetry
NIPS	Non-solvent induced phase separation
OCV	Open circuit voltage
RFB	Redox flow battery
SE	System efficiency
SEM	Scanning electron spectroscopy

SFF	Serpentine flow field
SoC	State-of-charge
VE	Voltage efficiency
VRFB	Vanadium redox flow battery

Nomenclature

$\boldsymbol{a}$	Boundary thickness
$\boldsymbol{A}$	Area
$\boldsymbol{A_c}$	Cross-section area
$\boldsymbol{A_t}$	Internal surface area
$\boldsymbol{c}$	Concentration
CE	Coulombic efficiency
CR	Compression ratio
$\boldsymbol{C_{\mathrm{O}}}$	Concentration of oxidized active species
$\boldsymbol{C_{\mathrm{R}}}$	Concentration of reduced active species
$\boldsymbol{C_{\mathrm{S}}}$	Specific capacitance
$\boldsymbol{D_{\mathrm{O}}}$	Diffusion coefficient of oxidized active species
$\boldsymbol{D_{\mathrm{R}}}$	Diffusion coefficient of reduced active species
$\boldsymbol{d_f}$	Fiber diameter
$\boldsymbol{E}$	Potential
$\boldsymbol{E_0}$	Peak amplitudes of potential
ECSA	Electrochemical active surface area
EDLC	Electrochemical double layer capacitance
$\boldsymbol{f}$	Frequency
$\boldsymbol{f_{\mathrm{g}}}$	Geometric scaling factor
$\boldsymbol{F}$	Faradaic constant
$\boldsymbol{i}$	Current density
$\boldsymbol{i_0}$	Exchange current density
$\boldsymbol{j}$	Imaginary unit
$\boldsymbol{I}$	Current
$\boldsymbol{I_0}$	Peak amplitudes of current
$\boldsymbol{k_0}$	Permeability
$\boldsymbol{k_{\mathrm{m}}}$	Mass transfer coefficient
$\boldsymbol{K_c}$	Kozeny-Carman constant

L_0	Original electrode thickness before compression
L_c	Electrode thickness after compression
m	Weight
n	Electron transfer number
N_M	Macmullin number
P	Pressure
P_{pump}	Pumping power
Q	Volumetric flow rate
Q_{charge}	Charge capacity
$Q_{discharge}$	Discharge capacity
Q_0	Admittance of the constant phase element
R	Gas constant
R_{CT}	Charge transfer resistance
R_{MT}	Mass transport resistance
R_{Ω}	Area-specific ohmic resistance
R_{dis}	Distributed resistance
T	Temperature
v_e	Electrolyte velocity
V	Volume
VE	Voltage efficiency
W	Warburg diffusion element
Z_{Im}	Imaginary part of the impedance
Z_{Re}	Real part of the impedance

Greek symbol

α	Exponent of the constant phase element
α_V	Volumetric specific surface area
β	Non-linear Forchheimer coefficient
ε	Porosity
η	Efficiency
η_{con}	Concentration overpotential
κ	Permeability

κ_{eff}	Effective ionic conductivity of porous electrodes
κ_s	Electrolyte conductivity
μ	Dynamic viscosity
ρ	Density
ρ_e	Specific electronic resistivity
ρ_i	Specific ionic resistivity
τ	Tortuosity
φ	Shifted phase
ω	Radial frequency

Chapter 1

Introduction

1.1 Energy Storage System

The increasing global population and rapid technology evolution have been accelerating energy consumption demand. Yet, the traditional energy sources, primarily fossil fuels (i.e., coal, oil, nature gas, etc.), hinder the pathway to a sustainable, socio-economic, and carbon-neutral world. On the one hand, the exploitation of non-renewable fossil energies has a ripple effect on the environment and society, which causes pollution to the air, freshwater, soil, and oceans. On the other hand, the consumption of the fossil fuels has led to a significant increase in carbon dioxide emissions, exaggerating the greenhouse effect. The excessive greenhouse gas emissions have led to issues including the rise of global average temperatures and widespread melting of glaciers, which pose substantial challenges to social development. This underlines the importance of tapping into renewable energy resources [1].

Global renewable capacity is expected to increase by almost 2,400 GW from 2022 to 2027 according to the International Energy Agency's 2021 Energy Report (IEA) [6]. Solar and wind power are the most widely used renewable energy sources, which are expected to account for almost 90% of all new renewable energy installations in 2027 [6]. However, the growth of renewable clean energy sources encounters a fundamental challenge: the energy derived from solar, hydro, and wind generation is intermittent and fluctuates. Integrating these sources directly into the power grid without proper management can destabilize the energy network, leading to potential risks, including power outages [7]. Addressing this pivotal issue and facilitating the widespread adoption of renewable clean energy rely on the development of large-scale energy storage systems [8].

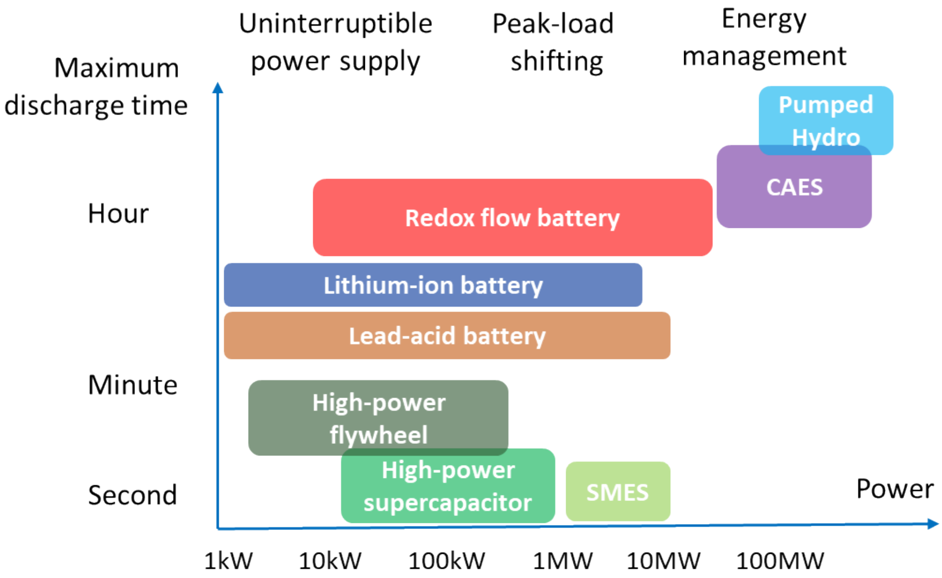

Figure 1.1 Maximum discharge time and power ratings for different energy storage technologies. CAES and SMES represents compressed-air energy storage and superconducting magnetic energy storage, respectively. Redrawn from Ref. [9] with permission. Copyright 2010, Electric Power Research Institute, Inc.

Energy storage technology refers to the process of converting intermittent renewable energies into forms that can be easily stored. These stored energies can be released as per actual requirements, ensuring a temporal and spatial separation between energy production and consumption [8]. Energy storage facilities have been extensively used in applications such as peak shaving and power following [10]. It has become an indispensable component of the renewable energy grid integration . Currently, common energy storage techniques include mechanical storage methods such as pumped hydropower, compressed air, and flywheel, and electrochemical methods such as sodium-sulfur batteries, lithium-ion batteries, lead-acid batteries, and redox flow batteries. Although competitive in terms of high energy storage capacity and longevity, mechanical storage methods usually demand specific locations and infrastructure requirements, which are geographically constrained in particular scenarios [11]. Compared to physical storage methods, electrochemical energy storage offers advantages in terms of cost and flexibility. Among them, lead-acid batteries are well-established, but they have a relatively low energy density and a limited cycle life, coupled with environmental concerns [12]. Lithium-ion batteries have been widely adopted as primary power source for portable devices. They provide a higher energy density but face safety and cost issues when considering large-scale energy storage [13]. Redox flow batteries stand out for their reliability, eco-friendliness, and deep discharge capabilities, which is considered to be one of the most promising and competitive electrochemical energy storage technologies [14].

Table 1.1 Comparison among different energy storage technologies [15]

Energy storage type	Capital cost ($/kW·h)	Efficiency	Lifespan (years)	Energy density (W·h/L)	Power output (MW)
Mechanical storage					
Pumped Hydro	5-100	70-87%	40-100	0.5-1.5	100-5,000
Compressed air	2-50	40-80%	20-100	3-6	1-400
Flywheels	1,000-5,000	80-99%	15-20	20-80	0.002-20
Supercapacitors	300-2,000	>97%	>20	>100,000	0.001-10
Electrochemical storage					
Lithium-ion batteries	600-2,500	85-90%	5-20	200-600	0.1-50
Lead acid batteries	200-400	70-92%	5-10	50-80	0.001-50
Vanadium RFB	150-1,000	65-85%	10-20	15-33	0.005-1.5
Zn-based RFB	150-1,000	75-80%	5-20	30-60	0.025-1

* The values provided in the table are approximate and can vary significantly based on the specific technology, design, manufacturer, and other factors.

1.2 Redox flow batteries

Redox flow battery (RFB) was initially introduced by L.H. Thaller in 1974 [16]. As depicted in Fig. 1.2, RFB system is primarily composed of battery stack, circulation pumps, and storage tanks. Unlike typical solid-state batteries, the positive and negative electrolytes in flow batteries are stored in external tanks outside the battery stack. The electrolytes are circulated into the reactor (using two pumps), where reversible redox reactions occur on the electrode surface. The energy capacity of a redox flow battery is determined by the volume of the electrolyte stored in the tanks and the concentration of its soluble active species. And the power output is determined by the size of the reactor and the number of cells connected in series within the battery stack. Consequently, the energy and power of redox flow batteries can be independently adjusted and scaled according to the demand. Such a design achieves decoupling of energy capacity and power output, which is the main advantage of the RFBs as large-scale energy storage systems. More importantly, unlike traditional batteries (e.g., lithium-ion batteries) where the electrodes undergo chemical and morphological changes during electrochemical reactions, the electrodes in RFBs only serve as a site for the active species reactions without participating in chemical reactions. This implies that RFBs can theoretically operate with deep charge-discharge cycles without risks of combustion, explosion, or significant performance degradation.

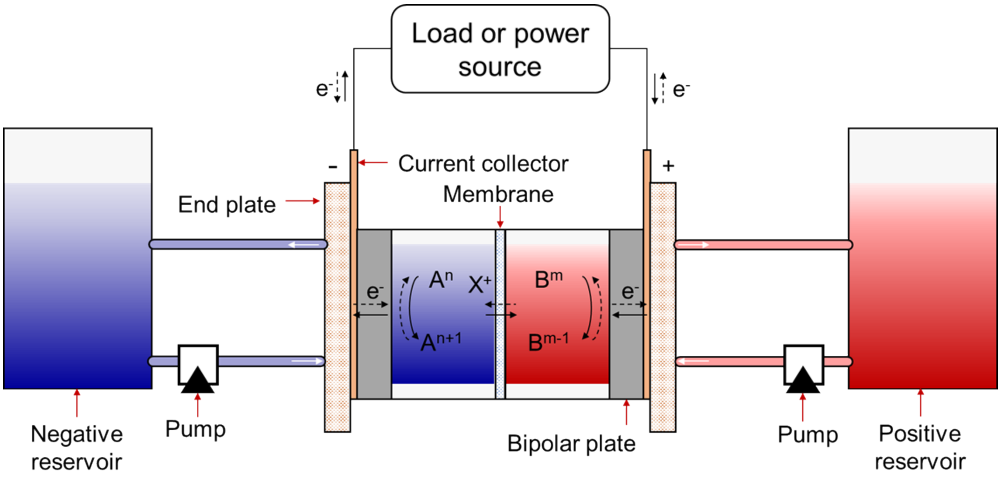

Figure 1.2 Schematic drawing of a redox flow battery system. A and B are active species dissolved in electrolytes. X is the ion species which cross the membrane to maintain charge balance. Solid arrows represent discharging process while dashed arrows represent charging process.

In recent years, a large number of RFBs with new electrolytes, such as semi-solid lithium ion electrolytes [17], alkaline anthraquinone electrolytes [18], and polymer electrolytes [19], have been developed and investigated. Here, we divide RFBs into aqueous RFBs and non-aqueous RFBs according to whether the solvent used is water or another organic solvent.

1.2.1 Non-aqueous Redox Flow Batteries

RFBs usually display lower energy density than encapsulated batteries using solid active materials, which is largely due to their relatively low cell voltage and limited solubility of the active materials. The limited voltage window of aqueous electrolytes (e.g., up to 1.5 V) has become a significant bottleneck for the advancement of RFBs [20]. In non-aqueous RFBs, organic solvents are adopted and higher potential window can be achieved (e.g., up to 4 V). Such a high voltage window of non-aqueous RFB has led to increased attention [21]. Non-aqueous RFBs include metal-based [22] and metal-free systems [23]. The metal-free systems offer higher solubility and electrochemical performance. Research in non-aqueous RFBs is relatively nascent but has accelerated in recent years. For example, Li et al. [24] proposed an all-organic non-aqueous RFB using acetonitrile as the electrolyte solvent and 2,2,6,6-tetramethylpiperidine-N-oxyl (TEMPO) and N-methylphthalimide (NMP) as the active redox couples in positive and negative sides, respectively. This type of RFB achieved high coulombic efficiency of >90% and high voltage window of 1.6 V.

Although higher voltage can be achieved, factors like reactivity, solubility, and stability of the active species also play a vital role on the performance of non-aqueous RFBs. At present, several other organic active species, such as thiophene derivatives [25] and dinaphtho-fused benzene derivatives [26], have been investigated. In addition, the choice of solvent is also crucial. Non-aqueous RFBs mainly use solvents like acetonitrile, carbonates, and ethers, which have disadvantages of lower ionic conductivity and limited solubility for less polar organic active species. Hence, it still necessitates the search for better alternatives. Overall, despite there is a growing interest in non-aqueous RFBs, they still face many challenges such as safety, cost, and performance.

1.2.2 Aqueous Redox Flow Batteries

Safety concerns are significant issues with organic-based batteries. In 2014, M.J. Aziz's group from Harvard University first introduced the concept of an aqueous organic RFB [27]. This battery uses an aqueous electrolyte containing water-soluble organic redox molecules (i.e., anthraquinone-based RFBs). The aqueous organic flow battery not only retains the advantages of high-performance organic redox couples, but also address the safety issues brought about by flammable non-aqueous solvent. Followed by this, several water-soluble organic redox couples have developed, including those based on pyridine [28], methylene blue [29], TEMPO [30], ferrocene [31], and quinones [32]. Although aqueous organic flow batteries still face challenges such as limited types of active materials, low solubility, and low operational current density, it is still considered as one of the most promising candidates for next-generation RFB systems.

In addition to the organic-based redox couples, aqueous RFBs include metal-based systems. These systems are the most commercially among the various RFBs in recent years. Although they are characterized by low energy density due to the limitation of voltage window, their long-term stability and cost-effectiveness make them attractive in applications. The first RFB concept proposed by National Aeronautics and Space Administration (NASA) [33], known as the iron-based Fe/Cr RFB, utilized ferric chloride (Fe^{2+}/Fe^{3+}, $E^0 = 0.77$ V vs. SHE) and chromic chloride (Cr^{3+}/Cr^{2+}, $E^0 = -0.41$ V vs. SHE) dissolved in hydrochloric acid solution as its positive and negative electrolytes, respectively. Due to the contamination caused by trans-membrane crossover of the active species, the advancement of commercialization was significantly hindered. To address these issues, the all-iron RFB was developed [34] using Fe^{2+}/Fe^{3+} and Fe/Fe^{2+} as positive and negative redox couples, respectively. Given the theoretical voltage of 1.21 V for the all-iron RFB and the high solubility of iron salts, the expected energy density of this RFB can reach up to 76 W·h/L. However, there is an inherent conflict in the pH range of the electrolyte that limits the enhancement of battery performance. Specifically, the equilibrium potential of Fe/Fe^{2+} is lower than the hydrogen evolution potential. This inevitably leads to hydrogen evolution as a side reaction, which becomes more prominent as the electrolyte pH decreases. However, the iron salts tend to hydrolyze when the electrolyte pH is raised (e.g., pH > 2). This creates a challenge in optimizing the all-iron RFB's development [35]. Despite these challenges, the low cost and abundant nature of iron drive explorations to optimize the battery performance of all-iron RFB, with ongoing efforts to address and overcome these issues.

Zn-based RFBs are another type of aqueous RFB that are attracting attention [36]. During the battery charging process, the anode side undergoes a Zn^{2+} deposition reaction, which means that the zinc-based RFBs are typical types of deposition-type RFBs. Due to the low deposition potential of Zn, these batteries possess a high theoretical voltage (e.g., Zn/Br_2,

E^0 = 1.83 V vs. SHE). This characteristic helps in increasing the energy density of the battery and reducing its cost. Although Zn-based RFBs have achieved performance optimization and preliminary commercialization progress, inherent drawbacks of deposition-type batteries remain unresolved. During deposition, Zn tends to form dendrites, which leads to capacity degradation. Dendrites that pierce the membrane can cause battery short circuits. The dendrite issue becomes more prominent when adopting higher current density [37].

The all vanadium redox flow battery (VRFB), regarded as the most successful commercial RFBs to date, uses VO_2^+/VO^{2+} and V^{2+}/V^{3+} as the positive and negative electrolyte redox couples, respectively. VRFB was first patented in 1986 by Skyllas-Kazacos et al. [38]. Known for their long operational lifespan and high safety, it has received a lot of attention and development over the past 30 years. Even though there are opportunities for further enhancement in cost-efficiency and performance, it is still widely recognized as one of the most promising RFB solutions [39].

1.2.3 Vanadium Redox Flow Batteries

Vanadium is a trace element widely distributed on Earth with an abundance of approximately 0.02%, with approximately 98% of it derived from vanadium titanium magnetite. Vanadium exists in various oxidation states, that is, +5, +4, +3, and +2. Hence, the VRFB utilizes VO_2^+/VO^{2+} and V^{2+}/V^{3+} as the active species for the positive and negative electrodes, respectively. The use of the vanadium active species on both sides effectively minimizes the performance degradation caused by crossover of active species. During the charge and discharge process, the oxidation and reduction reactions in positive and negative side are as follows:

$$\text{Cathode: } VO^{2+} + H_2O \xrightarrow{\text{charge}} VO_2^{+} + 2H^{+} + e^{-} \quad (1.1)$$

$$\text{Anode: } V^{3+} + e^{-} \xrightarrow{\text{charge}} V^{2+} \quad (1.2)$$

$$\text{Overall reaction: } VO^{2+} + V^{3+} + H_2O \xrightarrow{\text{charge}} VO_2^{+} + V^{2+} + 2H^{+} \quad (1.3)$$

Figure 1.3 Picture of a 15 kW/120 kW·h VRFB system installed as part of the distributed energy systems experimental facility at Risø campus, Technical University of Denmark [40]. The battery stack was refurbished in 2020 and the new stack is 50 kW/120 kW·h.

The advantages of the VRFB system include high energy capacity, long lifespan, independent adjustability of capacity and power, fast response time, low self-discharge rate, and high safety [41]. While VRFBs possess distinct advantages and demonstrate significant potential for large-scale energy storage applications, they still face challenges related to economic costs and electrochemical performance that need further improvement to meet current energy storage market demands [42].

Firstly, the primary barrier to wider adoption of VRFBs in the energy storage market is their high capital costs [43]. the U.S. Department of Energy has established that the investment needed for large-scale storage devices should be less than \$100 per kW·h per application [44]. A cost analysis of VRFB system indicates that the capital cost for a VRFB system with a capacity of 1 MW/4 MW·h exceeds \$450 per kW·h [45]. The reason for such a significant investment is that grid-scale VRFB systems require substantial amounts of raw materials. The manufacturing costs of the components used in VRFBs, along with the extraction costs of the vanadium electrolyte, are highly susceptible to fluctuations due to economic policies and market trends. Numerous studies have been conducted to reduce the operational costs of VRFBs [46]. One cost-effective approach is to significantly enhance the performance of VRFBs, including improvements in power density, electrolyte utilization, and long-term cycling stability, thereby reducing the overall capital costs [43].

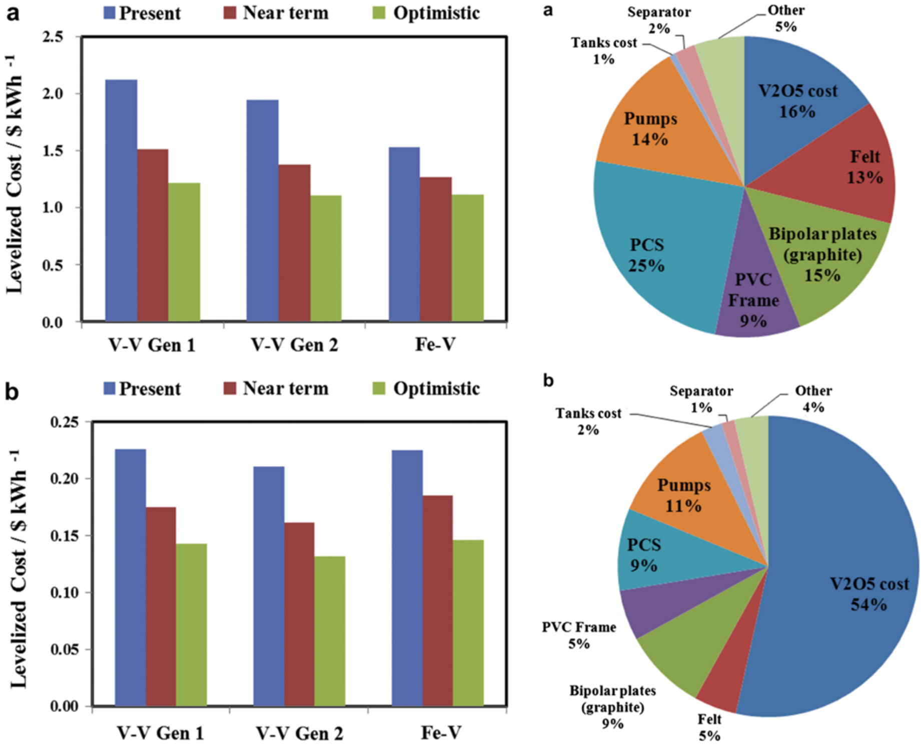

Figure 1.4 System cost analysis of (a) 1 MW/0.25 MW·h and (a) 1 MW/4 MW·h RFB systems. Adapted from Ref. [45] with permission. Copyright 2012, Elsevier B.V.

Secondly, the current state-of-the-art VRFBs demonstrate a medium-level performance in terms of power output per unit area within the energy storage technologies. The systems are below expectations to achieve the anticipated power output targets, leading to an enforced increase in the battery system's size to ensure the desired power output that matches the specifications. Enhancing the power density leads to a reduction in the physical dimensions and component requirements of the battery system, thereby decreasing capital costs for VRFBs. According to the electrochemical reaction mechanisms, boosting the power density entails minimizing activation polarization losses, ohmic losses, and concentration polarization losses. Activation polarization losses are determined by the active specific surface area of the electrodes and the reactive area they provide. The number of functional groups on the electrode surface and the internal pore microstructure play a significant role here. Ohmic losses are determined by the area specific resistance (ASR) of the separator (i.e., membrane), ionic conductivity of the electrolytes, and the electron transport pathway (i.e., tortuosity) within the electrode. Concentration polarization losses are determined by mass transport process of the active species from the bulk to the surface within porous electrodes. Developing a high power density VRFB system with minimized electrochemical losses poses significant challenges. It involves complex issues which require knowledge from material science, engineering, fluid dynamics, and electrochemical technologies. One of the essential points is to simultaneously consider both mass transport behavior and reactivity of active species [51]. Given the potential trade-offs between these two factors, it is crucial to strike a balance between them to achieve a substantial improvement in power density.

Additionally, the electrolyte utilization ratio is another important factor that directly impacts the effective use of active materials during charge and discharge cycles [52]. Enhancing the electrolyte utilization ratio can potentially reduce the amount of active material needed in the electrolyte, leading to a consequent decrease in electrolyte costs. Electrochemical polarization losses significantly hamper the electrolyte utilization ratio in VRFBs, especially under high current density conditions. Efforts need to be made to minimize the overpotential during both charge and discharge processes, particularly concentration polarization losses to extend the duration at the end of charge and discharge processes.

Moreover, the current VRFB systems encounter challenges related to their cycle stability [53]. When considering the needs for long-term operation, the emphasis on their cycle stability becomes paramount, seven surpassing the importance of power density. The capacity degradation during operations directly affects the RFB’s stability, which lead to elevated system maintenance costs and the battery failure. In VRFBs, the capacity degradation is mainly as a result of the transmembrane migration process of active vanadium ions of different valence states and water. Although this issue is not fatal due to the same vanadium species adopted in both sides, it become more evident and detrimental over prolonged durations. This process may introduce a self-discharge process and an imbalance of the state-of-charge (SoC) between the positive and negative electrodes, resulting in battery capacity losses. One simple solution is to mix and redistribute the electrolytes (i.e., electrolyte regeneration [54]) between the two sides. This can effectively recover the battery capacity. Besides, another factor that affects battery stability is from the loss of active reactive sites on the electrode surface. Catalyst-modified electrodes tend to lose particles over time due to their prolonged exposure to the continuous flowing electrolytes [55]. This leads to increased overpotentials during charge and discharge cycles and diminished battery capacity. Addressing the performance degradation is challenging without replacement of the battery components which may lead to significant maintenance costs and operational disruptions. To enhance the long-term cycling stability of VRFBs, efforts should be made to improve the structural stability of the porous electrodes.

Addressing these challenges mentioned above necessitates a comprehensive investigation into improving the performance of the key battery components of VRFBs. The critical battery components of VRFBs mainly include electrolytes, ion-exchange membrane, and porous electrodes.

1.3 Battery Components

As described above, a VRFB module primarily comprises a power unit made up of cell stacks, an energy storage unit made up of electrolyte tanks, a transport unit including piping, valves, and pumps, and a control unit made of battery management systems. For large-scale energy storage, a certain number of cell stacks are integrated into a single module through series and parallel connections. The cell stack is the core of RFB system, as shown in Fig. 1.5. Within each individual cell, an ion-exchange membrane serves as a separator between the positive and negative electrolytes. Symmetrically placed on either side of this membrane are the electrodes, gaskets, flow plates, current collectors, insulating layers, and end plates. The performance related components, which include the electrolytes, membrane, and electrodes, are directly related to the output performance of the VRFBs. These components are not only the critical components of the VRFB system but also the central focus of the related research and development.

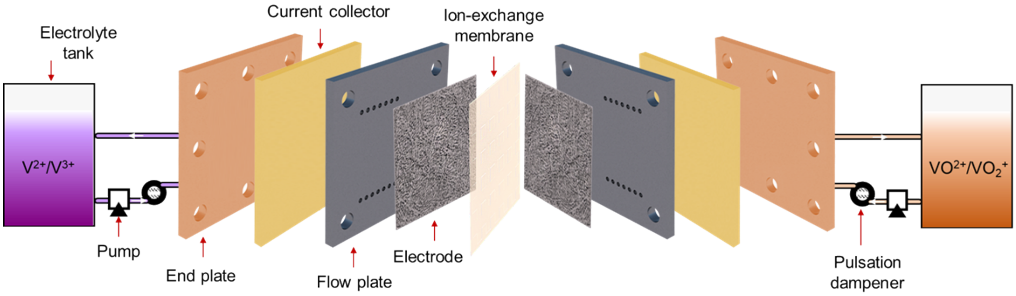

Figure 1.5 Schematic drawing of a single-cell VRFB system. The key battery components are presented in exploded-view. Some small components (such as gaskets, O-rings, bolts, insulation layer, etc.) are neglected.

1.3.1 Electrolytes

In VRFB systems, the electrolytes are composed of various valence states of vanadium ions and an aqueous solutions of acids (e.g., hydrochloric acid, sulfuric acid, etc.). Typically, V_2O_5 or $VOSO_4$ is used as the primary raw material to prepare the electrolytes through either chemical or electrochemical methods. Considering aspects of solubility and conductivity, sulfuric acid is the most widely used supporting electrolytes in VRFBs. Hence, the initial electrolyte usually consists of an aqueous sulfuric acid solution containing V^{3+}/VO^{2+}. Currently, the energy density of the VRFB is only approximately 20-40 W·h/L, primarily due to the inferior solubility and thermal stability of the active species in the electrolytes. Studies have shown that the VO_2^+ tends to precipitate and change to V_2O_5 when the electrolyte temperature is above 50 °C at high concentrations (e.g., >1.5 mol/L [56]). Also V^{3+} tends to precipitate when the temperature is below 10 °C [57]. To further enhance the solubility and stability of the electrolytes, various optimization strategies have been proved effectively. For example, using mixed acids as supporting electrolytes shows obvious benefits [58]. The mixture of hydrochloride acid and sulfuric acid can significantly improve the solubility of active species. The addition of phosphoric acid into the electrolytes has been proved to stabilize the electrolyte system at low temperatures [59]. Overall, the quality of the electrolytes is intrinsically linked to the performance of the VRFBs, with the electrolyte conductivity affecting the power density, the solubility affecting the energy capacity, and the stability affecting battery lifespan.

1.3.2 Membrane

The membrane is another key component within the battery stack. It separates the active species of the positive and negative sides, prevents crossover contamination, and conducts protons. An ideal membrane adopted in VRFB system needs to possess multiple characteristics, including high crossover resistance to vanadium species to reduce capacity fade, high ionic conductivity to reduce the internal resistances of the battery, and superior durability to ensure a long battery cycle lifespan. The most used membrane type is the ion-exchange membrane. It is made of polymer chains and ionic functional groups. The most representative type is the Nafion membrane (i.e., sulfonated tetrafluoroethylene-based fluoropolymer-copolymer membrane) from DuPont Company. Popular types of the Nafion membrane include Nafion 117, Nafion 211, FS-950, etc. [60]. They are all Nafion-based and differ in the thickness, equivalent weight, and other specific properties. The Nafion membranes can meet the above-mentioned basic requirements, but its high cost and relatively low ion selectivity limit its broader applications. Multiple modification strategies based on Nafion membrane have been explored, including modification with inorganic particles [61], doping with nanoparticles [62], and multi-resin composites [63]. Alternatively, many studies have been working on the development of cheaper ion-exchange membranes to replace Nafion membranes. They include adoptions of polyvinylidene fluoride (PVDF) [64], polyetheretherketone (PEEK) [65], polysulfone (PSF) [66], polybenzimidazole (PBI) [67], etc. However, a significant challenge is to strike a balance between enhancing ionic conductivity and maintaining resistance to vanadium. Besides, propensity of ion-exchange groups to promote membrane degradation, which is another challenge to maintain long-term cycle stability of the ion-exchange membranes.

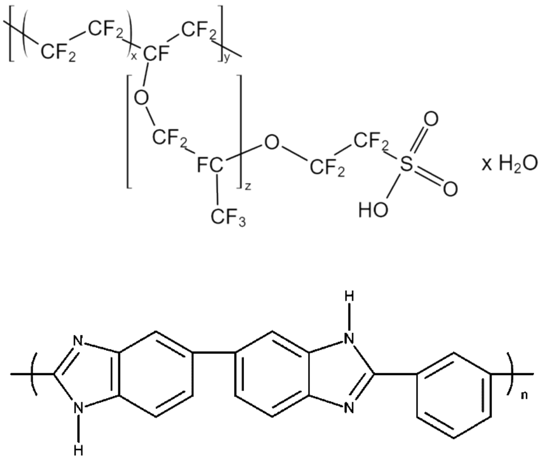

Figure 1.6 General structure of Nafion (above) and PBI (below) polymers. These two types of membranes were used in the present work.

1.3.3 Electrode

Electrodes play a crucial role in RFB systems. The primary functions of the electrodes include providing space for redox reactions of active species, facilitating electron transfer, and distributing the electrolytes within battery stack [68]. The performance of the electrode directly is linked to various polarization losses inside the flow battery, thereby influencing the battery's output and costs.

Specifically, the active specific surface area of the electrode determines the activation polarization. The electrode conductivity affects ohmic losses, and the mass transfer properties is closely related to concentration polarization. Currently, various carbon-fiber based materials, including carbon felt (CF) [69], graphite felt (GF) [70], carbon paper (CP) [71], and carbon cloth (CC) [72], have been widely studied due to their low cost, large specific surface area, high conductivity, and excellent chemical stability. CFs and GFs are derived from PAN (polyacrylonitrile) and Rayon (a semi-synthetic cellulose derived polymer) via extrusion and pyrolysis [73]. They possess advantages of high porous structure and are widely used in the commercial VRFB systems. Typically, to provide sufficient reactive active sites, the thickness of the CFs or GFs is usually not less than 3 mm. As a result, the area specific resistance (ASR) of the electrode remains in the high range of 3-5 Ω·cm². In order to minimize the internal resistance of the battery, Aaron et al. [74] designed and manufactured a VRFB with a zero-gap serpentine flow field structure. They chose stacked multi-layer of CPs as the electrodes, replacing the traditional CFs. Due to the improvement of battery structure and electrodes, the battery exhibited reduced polarization losses and a higher peak energy density of 557 mW/cm². In conventional flow-through flow field (FTFF), the electrolyte is forced to pass through the porous electrode due to the pressure drop between the inlet and outlet of the electrode, so the convection plays a dominant role in the transport of active species. In the VRFB with a serpentine flow field (SFF), the electrolyte distribution within the porous electrodes is jointly controlled by diffusion and under-rib convection. The driving force for the under-rib convection comes from the pressure difference between adjacent channels [75]. As a result, the electrode internal microstructure and its mass transfer properties play a critical role in the electrochemical performance and pressure drop under different flow field configurations. Balancing the interactions between the flow fields and porous electrodes is important to optimize the transport behavior and related losses [76].

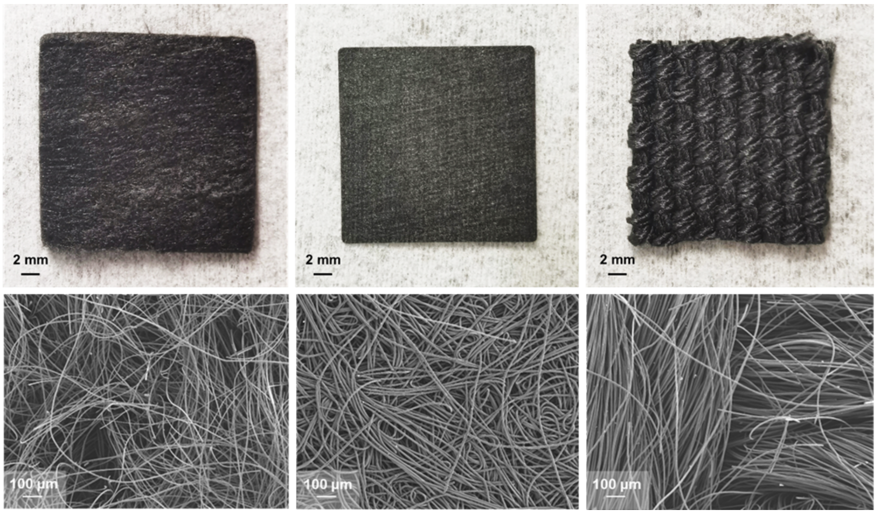

Figure 1.7 Picture of the carbon felt (left), carbon paper (middle), and carbon cloth (right) electrodes. SEM images are shown below.

The mass transfer process has been recognized as an important performance-limiting factor [77]. Enhancing the applied flow rate of the electrolyte is a way to reduce the diffusion distance [78]. Although valid, it comes at the expense of high pressure drop and pump consumptions, which may result in decreased system efficiency at high flow rates. From the electrode microstructure point of view, diffusion of active species within porous media is correlated with the porosity of the porous electrodes, and convection is determined by the permeability of electrodes. Specifically, the permeability is related to the fiber diameter, tortuosity of the electrolyte pathways, and electrode porosity. Hence, it is important for porous electrodes to keep the high porosity characteristics to enhance the mass transfer performance of the electrodes. Accordingly, Mayrhuber et al. [79] used CO_2 laser to create larger pores on carbon paper electrodes, aiming to improve the electrolyte penetration within the electrodes along through-plane direction. Compared to the original carbon paper, the modified carbon paper showed a 30% increase in the peak power density although it has a 15% reduction in the total active specific surface area. Xu et al. [80] used electrospinning technology to prepare a carbon fiber net with a very high porosity as an independent electrode for VRFBs. The design aims to minimize the concentration polarization and enhance the transport of active species inside the porous carbon fiber network. At a current density of 60 mA/cm^2, the energy efficiency reached 77.9%, which is higher than with the original carbon fiber networks. In addition, some strategies such as multi-layer carbon papers with different porosity, multi-segmented carbon felts, carbon felts with manually carved macro-channels were developed to enhance the mass transport performance. They were proved to be beneficial to the battery performance.

Recently, CC electrodes attracted a lot of attention [81]. Unlike randomly distributed fibers with low-hierarchical fiber orientations from CFs and CPs, CC is a woven structure and consists of periodically repeating bundles of carbon fibers from longitudinal (warp) and transverse (weft) directions without binders. It offers flexibility of woven pattern designs and bimodal pore size distributions, which is a promising candidate to enhance mass transfer properties and facilitate electrolyte penetration at low pressure drop sacrifice. Specifically, the fiber bundle arrangements of CCs create hierarchical pore size distributions including the intersection void between fiber bundles (e.g., ~10-100 μm), fiber-to-fiber distance (e.g., ~1-10 μm), and meso-pores on individual fiber surfaces (e.g., 2-50 nm). Due to the presence of the large void and well-defined microstructure, CC has been shown to be a high performance electrode with reduced mass transfer resistance and pressure drop in aqueous [82] and non-aqueous [83] RFB systems.

In addition to the mass transfer properties, the hydrophobicity and low electrochemical active surface area of pristine carbon-fiber electrodes (i.e., CF, GF, CC, etc.) seriously build up the overall resistances. The electrodes used in RFBs need to possess a high electrochemical active surface area, which can facilitate the acceleration of the reaction and minimize the activation polarization. For conventional carbon-fiber electrodes, to ensure a high permeability, the diameter of carbon fibers is maintained approximately 10 μm. The overlapping of fibers creates pores with diameters of several micrometers, facilitating the pathways for electrolyte transport within the electrodes. However, although the electrode achieves high porosity and larger pore sizes, the number of carbon fibers per unit area decreases. This results in a lower specific surface area, which in turn limits the further enhancement of electrochemical performance. To address this issue, numerous modification methods have been proposed including thermal [84] or acid [85] pre-treatment, surface modification [86], pore-etching on fibers [87], etc. These methods have been proved to effectively improve the battery performance. At a current density of 100 mA/cm^2, the VRFBs achieved the desired energy efficiency target of >80% [87].

Overall, the ongoing refinements have led to significant improvements in electrode surface area, hydrophilicity, and electrochemical activity. However, it still remains a challenge to understand the interactions between the reaction and micro-scale mass transfer process, which is essential for achievement of optimized trade-off between these two processes. Electrodes with hierarchical, multi-scale pore microstructures have been verified to be an effective way to balance kinetics and mass transfer. The electrodes with optimized kinetic and mass transfer performance can meet the requirements and commercial needs of RFBs for high efficiency and low cost, which are regarded as a future direction for next-generation RFB systems.

1.3.4 Cell Hardware

In addition to the above mentioned components, there are some remaining performance-related and assembly-related battery components, including the flow plates, gaskets, current collector, and end plates, etc. These components are briefly described in the following.

Flow Plates: Flow plates are responsible for distributing the electrolytes evenly throughout the cell and can also serve to remove heat from the cell. Currently there are several types of flow fields engraved on the flow plates, including serpentine [88], interdigitated [89], and flow-through [90] flow fields. The schemes of these flow filed are shown in Fig. 1.8. The design of the flow plates can significantly influence the battery's performance by ensuring uniform flow distribution and minimizing pressure drop.

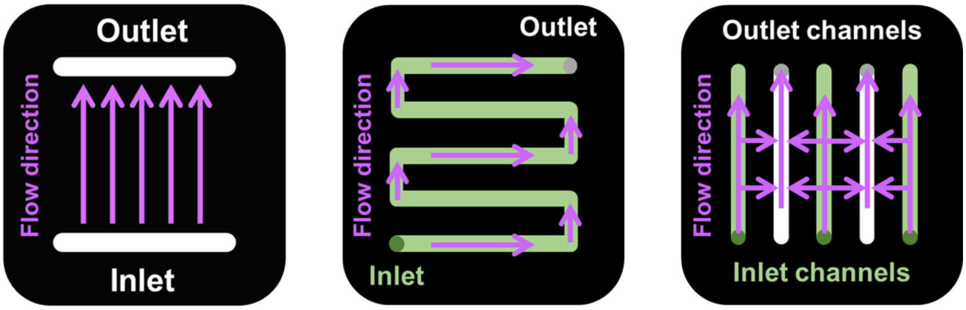

Figure 1.8 Schemes of representative flow plates with flow-through flow field (FTFF, left), serpentine flow field (SFF, middle), and interdigitated flow field (IDFF, right).

Gaskets: Gaskets ensure the sealing between different battery components, preventing any leakage of the electrolytes. They play a crucial role in maintaining the battery's integrity and ensuring long operational life. The selection of the thickness of the gaskets determines the electrode compression [91], which is an important operational parameter in RFB with impacts on electrode microstructure and the contact areas to the flow plates.

Current collector: Current collector serves as the intermediary between the electrode and the external circuit. It is usually covered by insulating layers on the one side. It ensures the efficient transfer of electrons during the battery operation, thus aiding in the overall energy conversion process.

End plates: End plates provide mechanical support to the entire battery assembly. They are typically made of robust materials that can withstand the stresses of the battery operation, ensuring the structural integrity of the battery pack.

1.4 Assessment Methods of Redox Flow Batteries

Performance assessment methods are crucial for flow battery research [92]. Charge-discharge cycling tests are the standard methods for evaluating the performance of RFBs. Several important performance metrics can be obtained through the cycling tests, including the coulombic efficiency (CE), Voltage efficiency (VE), energy efficiency (EE), system efficiency (SE), and electrolyte utilization ratio (EU), etc. Each of them is introduced in the following. In addition, the different cell cycling configurations and some other important electrochemical characterization methods, including polarization measurements and electrochemical impedance spectroscopy (EIS), are briefly introduced here.

1.4.1 Performance Evaluation

Charge and discharge capacities (Q_{charge} and $Q_{\mathrm{discharge}}$): These metrics represent the amount of charge the battery can store (i.e., charge capacity) or deliver (i.e., discharge capacity). They are usually expressed in A·h.

Coulombic Efficiency (CE): CE represents the ratio of the total charge extracted during discharge process to the charge put in during charge process. It gives an idea of how much energy is retained in the battery after charging. A CE of 100% means that the battery releases the same amount of charge as it received.

$$CE = \frac{Q_{\mathrm{discharge}}}{Q_{\mathrm{charge}}} \tag{1.4}$$

Voltage Efficiency (VE): VE is the ratio of the average voltage during discharge process to the average voltage during charge process. It indicates how effectively the battery can convert chemical energy into electrical energy.

$$VE = \frac{\overline{E}_{\text{cell,discharge}}}{\overline{E}_{\text{cell,charge}}} \tag{1.5}$$

Energy Efficiency (EE): EE is a combination of CE and VE. EE provides a comprehensive view of the battery's operational efficiency.

$$EE = CE \times VE \tag{1.6}$$

System Efficiency (SE): on the base of EE, SE considers all the energy losses in the entire operation battery system, including pumps consumptions and other auxiliary equipment.

Electrolyte Utilization Ratio (EU): This metric indicates the fraction of active species in the electrolytes that gets utilized during a charge or discharge cycle. UE is the ratio of the achievable capacity during charge or discharge process to the theoretical capacity determined by electrolyte specifications. A high utilization ratio means a greater fraction of the available active species is effectively used.

$$EU = \frac{Q_{\text{charge}} / Q_{\text{discharge}}}{nFcV_{\text{electrolyte}}} \tag{1.7}$$

where n denotes the electron transfer number;

F denotes Faraday constant;

c denotes the concentration of electrolytes;

and $V_{\text{electrolyte}}$ denotes the electrolyte volume.

Energy Density: It represents the amount of energy that the battery can store per unit volume or mass. It is usually expressed in W·h/L or W·h/kg. This metric provides insights into how long the battery can deliver power.

Power Density: It represents the maximum power output per unit volume or area of the battery. It is usually expressed in W/L or W/cm^2. It gives insights into how quickly the battery can deliver or accept power.

These metrics collectively provide a comprehensive understanding of the performance evaluation of a RFB system, which helps to assess and compare various RFB designs and systems.

1.4.2 Cell Testing Configurations

In RFBs, there are different cell configurations used for testing and evaluation of materials and battery performance. Performance metrics obtained from different test configuration provide insights from individual material properties to the comprehensive performance of a full-cell system. Here, we introduce two prominent cell configurations: full cell and symmetric cell.

Full Cell Testing: In a full-cell configuration, both the positive and negative electrolytes are different, replicating the actual conditions of an operational RFB. This setup uses the redox couples for both the anode and the cathode in the practical application. Full-cell testing provides a more realistic and comprehensive view of the battery performance since it mimics the actual operational conditions. During the charge-discharge cycling tests of a full-cell configuration, it can provide understanding of the CE, VE, SE, and other key performance indicators under practical scenarios. It is often employed for final-stage testing or when evaluating the complete performance of new materials or designs in RFBs.

Symmetric Cell Testing: In symmetric cell testing, the same electrolyte is used on both anode and cathode sides. This setup is primarily used to isolate and study specific processes or materials. One of the advantages of the symmetric cell testing is that the transmembrane process of the active species is mitigated. Any changes observed can be attributed to the material or process being studied, since the same electrolytes used on both sides. It is noted that the electrolyte volume adopted on both sides in a symmetric cell with two-tank configuration can be different. Using excess electrolyte volume on one side can minimize the negative impacts on capacity fade due to the crossover of active species [92].

Symmetric cell testing can be conducted using a single-tank configuration, where the electrolyte circulates from one container through both sides of the cell. This method ensures a consistent state of charge (SoC) at the inlets of the reactor on both sides since the balance of the electrolytes between the anode and cathode is maintained as the two electrolytes mix together. This configuration is particularly beneficial when conducting the polarization measurement and electrochemical impedance spectroscopy of a symmetric cell, which requires maximum system stability.

Overall, both configurations offer unique insights, with full-cell testing being more representative of practical applications, while symmetric cell testing provides a controlled environment for focused investigations.

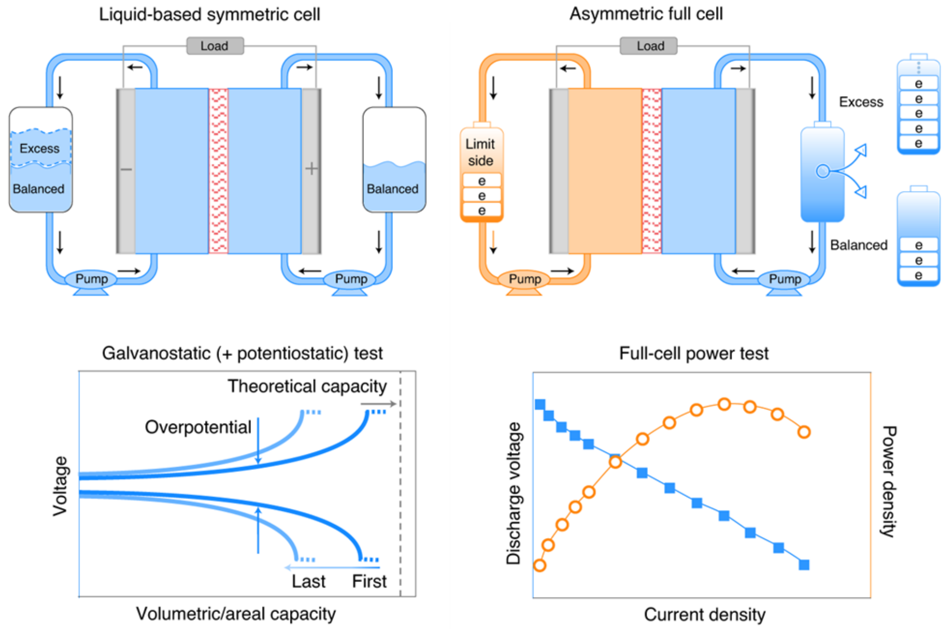

Figure 1.9 Schemes of symmetric cell (left) and full cell (right) configurations using either excessive or balanced electrolyte on the two sides . Recommended battery characterization protocols and reporting performance metrics for each of the cell configuration are shown below. Adapted from Ref. [92] with permission. Copyright 2021, Springer Nature Limited.

1.4.3 Battery Characterizations

To understand and evaluate the battery performance of RFBs under various operating conditions, several characterization techniques have been developed and utilized. Here, we briefly introduce cycling tests, polarization measurement, and electrochemical impedance spectroscopy that used in the present work.

Charge-discharge Cycling Tests: As mentioned above, charge-discharge cycling tests provide a direct evaluation of the practical performance of RFBs, revealing the effective capacity and efficiency over multiple cycles. It can be carried out in a few different ways, including constant current (CC), constant voltage (CV), and a combination of both (CC-CV). For the CC mode, the battery is charged or discharged at a constant current until a specific voltage or capacity is reached. And in the CV mode, the battery reaches a pre-set voltage and is maintained constant until the pre-defined current limit reaches. The CC-CV mode combines the two modes. Initially, the battery is charged using a constant current. Once a target voltage is reached, the method switches to CV mode. It ensures a fast and safe charge process with a quick charge initially and access more available electrolyte capacity in the end stage using CV. Overall, cycling tests primarily offer an overall evaluation of battery performance. It is challenging to get insights into the direct impacts of the change from a single battery material or operational condition. In order to quantitatively understand the battery performance, it needs additional diagnostic methods such as polarization measurement and EIS, which provide a targeted assessment of the electrochemical performance.

Polarization Measurement:

Polarization curve measures the voltage response of the battery against a range of current densities, which can be used to provide a qualitative assessment of overpotentials in the battery system, including ohmic loss, activation overpotential, and concentration overpotential. A typical polarization curve is shown in Fig. 1.10. Typically, at low current densities, the predominant losses of a VRFB are primarily due to the high kinetic overpotential, which indicates sluggish electrochemical reactions. It can be found from the initial sharp voltage decline at the low currents. At moderate current densities, a linear correlation between voltage and current is evident in the polarization curve. This is the ohmic-dominant region and it indicates the overall internal resistance within the battery. The primary contributor to the overall ohmic resistances tends to be the ionic resistance of the membrane especially for the applications using thick membrane to reduce crossover effects of active species, and also the contact resistances from the electrode and flow plates. At the highest currents, concentration polarization becomes the limiting factor. When the current is sufficiently high, the diffusion rate of the active species from the bulk to the electrode surface restrict further current increase even if the overpotential rises.

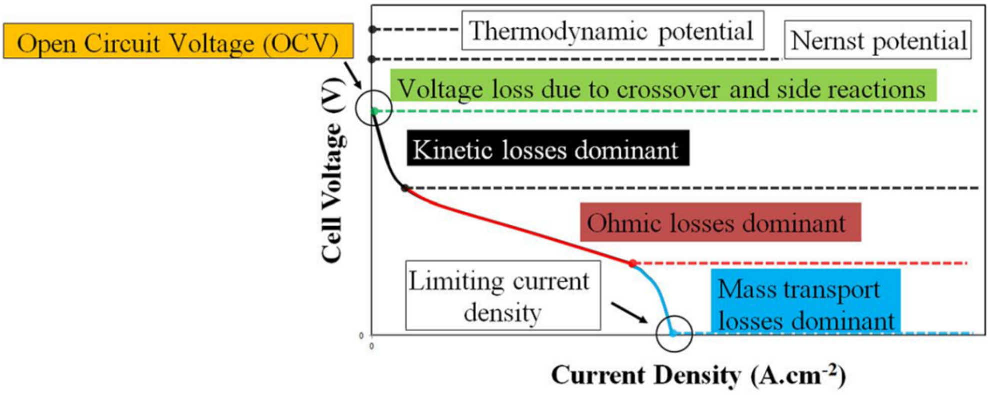

Figure 1.10 Typical polarization curve with multiple sources of overpotential. Adapted from Ref. [93].

Electrochemical Impedance Spectroscopy (EIS):

Electrochemical impedance spectroscopy (EIS) works with a small alternating currents (AC) and voltages over a range of frequencies to determine the battery's impedance spectrum. The magnitude and phase shift of the observed signal are captured over a spectrum of frequencies. When a sinusoidal potential signal is applied to a system (e.g., a RFB system), the response to this potential will be a current response with a shifted phase. Hence, according to Ohm’s Law, the impedance (*Z*) can be defined as the following equation:

$$Z = \frac{E(t)}{I(t)} = \frac{E_0 \sin(\omega\, t)}{I_0 \sin(\omega\, t + \varphi)} \tag{1.8}$$

where E_0 denotes the peak amplitudes of potential;

I_0 denotes the peak amplitudes of current;

ω denotes the radial frequency (i.e., $\omega = 2\pi f$, f denotes frequency);

and φ denotes the shifted phase.

Based on Euler's relationship:

$$\exp(j\varphi) = \cos\varphi + j\sin\varphi \tag{1.9}$$

where j denotes the imaginary unit.

Hence, the impedance can be expressed as follows:

$$Z = Z_0 \exp(j\varphi) = Z_0(\cos\varphi + j\sin\varphi) = Z_{\mathrm{Re}} + jZ_{\mathrm{Im}} \tag{1.10}$$

where Z_{Re} denotes the real part of the impedance;

Z_{Im} denotes the imaginary part of the impedance.

Impedance spectra can be viewed in a Nyquist plot, which is a plot of the imaginary component of impedance (i.e., $-Z_{\mathrm{Im}}$) as a function of the real part of impedance (i.e., Z_{Re}) at each frequency. The real and imaginary axes in Nyquist plot should always be plotted with equal scaling as the interpretation of the information is based on the shape of the plot. A representative Nyquist plot is shown in Fig. 1.11 in a VRFB system. Information about the process occurring in the system can be interpreted through by using an equivalent circuit model and fit this to the data using complex nonlinear least squares (CNLS) regression. The circuit elements used in equivalent circuit models include elements such as inductors, resistors, capacitors, constant phase elements, Warburg elements, etc. The equivalent circuit model is established based on a number of circuit elements in series and/or in parallel. A typical example of an equivalent circuit model is the Randles circuit, which is used to describe the impedance of a heterogeneous charge transfer process under semi-infinite linear diffusion conditions. A schematic of a Randles circuit is shown in Fig. 1.12. It consists of a series resistor (R_{ohmic}, usually including membrane resistance, contact resistances, ionic resistances from electrolytes, and electronic resistance from electrodes in an RFB cell) , a constant phase element (CPE), a charge transfer resistor (R_{ct}), and a Warburg diffusion element (W). For an electrochemical system that can be described by a Randles circuit, detailed information about ohmic, charge transfer, and finite diffusion resistances can be extracted from the parameters associated with the circuit elements.

In a RFB system, porous electrodes are commonly adopted to ensure high surface area. This increases the complexity of the EIS fitting. Due to the complexity of porous electrode microstructure, a semi-infinite model, developed by Levie [94] and adapted to flow battery conditions by Pezeshki et al. [95], was used to describe an electrode with cylindrical pores with uniform diameter filled with electrolyte. Assuming that the pores were cylindrical with a single pore size, this model could be resolved as a transmission-line model [96]. The concept of the transmission-line model is presented in Fig. 1. 13.

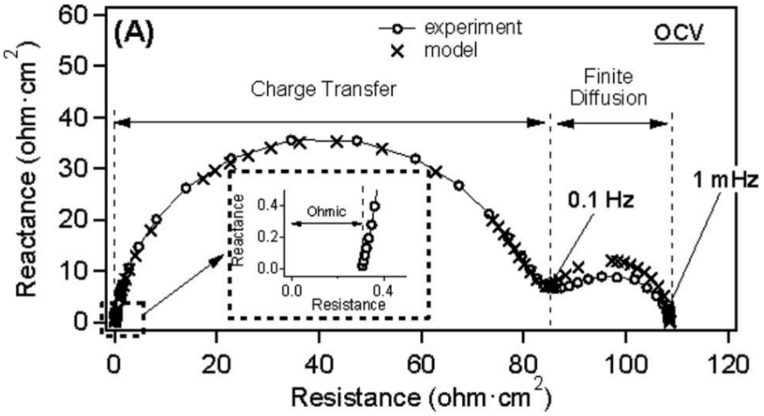

Figure 1.11 An example of EIS spectrum of a VRFB using single-layer carbon paper electrode in 0.8 mol/L V^{2+}/V^{3+}. Adapted from Ref. [97] with permission. Copyright 2014, The Electrochemical Society.

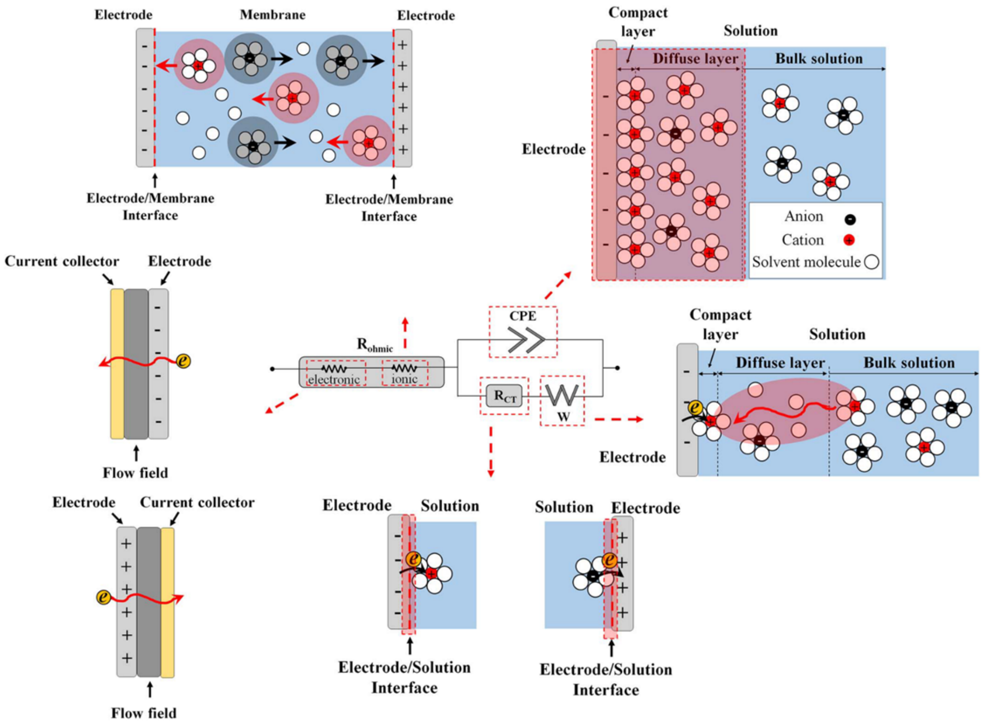

Figure 1.12 Schematic of the Randles circuit model and interpretation of the circuit elements. Adapted from Ref. [93].

Under blocking conditions, i.e., in the absence of faradaic reactions, the surface impedance of the interface between pores and electrolytes can be modelled with a CPE element. By fitting of a transmission-line model to the EIS data, the electrochemical double layer capacitance (EDLC) can be estimated using the following equation [98]:

$$EDLC = Q_0^{\frac{1}{\alpha}} \left(\frac{1}{R_s}\right)^{1-\frac{1}{\alpha}} \qquad (1.11)$$

where Q_0 denotes admittance of the constant phase element;

R_s denotes series resistances;

and α denotes exponent of the constant phase element.

Then, the electrochemical specific surface area (ECSA) of the porous electrode can be estimated using the following equation:

$$ECSA = \frac{EDLC}{C_s m_e} \tag{1.12}$$

where C_s denotes specific capacitance;

and m_e denotes weight of the measured electrode.

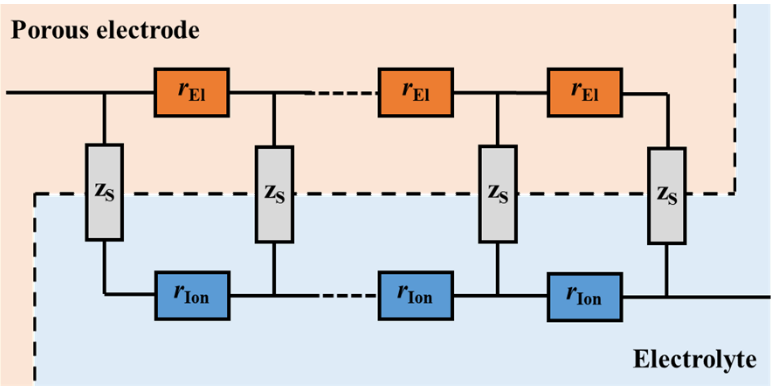

Figure 1.13 Schematic of the transmission-line model for a porous electrode. r_{El} and r_{Ion} denote the ohmic resistors representing electronic resistance and ionic resistance, respectively. z_S denote surface impedance of the interface between the electrolyte and the solid electrode. Redrawn from Ref. [96].

In the presence of faradaic reactions, i.e., under non-blocking conditions, the surface impedance is modeled using a Randles circuit with a finite length Warburg diffusion element, and this way kinetic and mass transport processes are considered in the transmission-line model. The impedance can then be resolved into distributed ohmic (R_{ohm}, electrode electronic and electrolyte ionic resistances in parallel), kinetic (R_{CT}), and mass transport resistance (R_{MT}), as follows:

$$R_{\text{ohm}} = L_c \frac{\rho_i + \rho_e}{3} + L_c \frac{\rho_i \rho_e}{3(\rho_i + \rho_e)} \tag{1.13}$$

where L_c denotes electrode thickness after compression;

ρ_i denotes specific ionic resistivity;

and ρ_e denotes specific electronic resistivity.

$$R_{\text{CT}} = \frac{ART}{A_t n F i_0} \tag{1.14}$$

where A denotes geometric area of the electrode;

A_t denotes internal surface area;

R denotes gas constant;

T denotes temperature;

n denotes electron transfer number;

F denotes Faradaic constant;

and i_0 denotes exchange current density.

$$R_{\text{MT}} = \frac{AaRT}{A_t f_g n^2 F^2} \left(\frac{1}{C_{\text{R}} D_{\text{R}}} + \frac{1}{C_{\text{O}} D_{\text{O}}}\right) \tag{1.15}$$

where a denotes boundary thickness;

f_g denotes geometric scaling factor;

C_R, C_O denote concentration of reduced and oxidized active species, respectively;

and D_R, D_O denote diffusion coefficient of reduced and oxidized active species, respectively.

1.5 Outline of the Thesis

As outlined in this chapter, although the RFB has shown potential in stationary grid-scale energy storage technology, further cost reduction of the RFB system is needed to achieve wider commercialization. It is critical to improve reactor performance to bring down the high capital cost, and one way to do this is to develop advanced porous electrodes with lower kinetic and mass transfer impedance. The objective of this thesis is to provides insights into the electrode microstructure with a better trade-off between active surface area and facile electrolyte transport pathways. This study is based on the use and optimization of three types of commercially available carbon-fiber and binder-free carbon electrodes. Tailored electrodes with integration of micro-flow fields into the electrode architecture is also considered to enhance mass transfer performance for high performance RFBs. Throughout the thesis, electrochemical impedance spectroscopy, polarization measurements, and charge-discharge battery cycling tests are employed. The analysis of the EIS data is performed through fitting of transmission line based equivalent circuit models to the obtained EIS data. Other characterization techniques include X-ray computed tomography, scanning electron microscopy (SEM), Brunauer-Emmett-Teller (BET), pressure drop measurements, etc. Simulations (e.g., Lattice Boltzmann Method) was also used to provide a qualitive analysis of the local flow distributions within the porous electrodes. Specifically, this thesis focuses on three distinct aspects of electrode and reactor engineering, and the results are divided into the following three chapters.

In **Chapter 2**, the morphological properties and electrochemical performance of three types of carbon-fiber electrodes (i.e., carbon felt, carbon paper, and carbon cloth) with distinct microstructures under 0-50% compression ratios in vanadium redox flow batteries were investigated. The 3D electrode morphology was characterized through X-ray computed tomography and the extracted key microstructural parameters were compared with corresponding electrochemically determined parameters. The optimal trade-off between fluid dynamics and electrochemical performance was investigated for three types of carbon-fiber porous electrodes.

Chapter 3 is mainly focused on the carbon cloth electrode and explored the potential of using it as a simplified flow field within an dual layer electrode assembly to enhance mass transport performance. A carbon cloth was placed close to the flow plate to serve as electrolyte distributor in a lateral flow through configuration, while a carbon paper sub-layer was placed near the membrane to provide a high density of reaction sites. Quantitative analysis of contributions from each type of polarization was investigated under both V^{2+}/V^{3+} and VO^{2+}/VO_2^+ redox couples in symmetric cells. The Lattice Boltzmann Method was adopted based on the 3-D reconstructed electrode structure to provide insight into the electrolyte distribution.

In **Chapter 4**, after investigation and optimization of commercial carbon-fiber electrodes, a novel approach relying on non-solvent induced phase separation (NIPS) was used to design non-fibrous carbon electrodes. This study involved integration of micro-flow fields directly into the electrode architecture during NIPS processing. The design of the electrode microstructures was tailored to simultaneously meet the requirements of high surface area, low mass transfer resistance, and low pressure drop.

References

[1] J. Twidell. Principles of renewable energy. *Renewable energy resources*, 1−31 (2021).

[2] O. Ellabban, H. Abu-Rub, F. Blaabjerg. Current status, future prospects and their enabling technology. *Renewable and sustainable energy reviews*, 39, 748−764 (2014).

[3] A. Hepbasli. A key review on exergetic analysis and assessment of renewable energy resources for a sustainable future. *Renewable and sustainable energy reviews*, 12, 593−661 (2008).

[4] P. Pinson, L. Mitridati, C. Ordoudis, J. Østergaard. Towards fully renewable energy systems: Experience and trends in Denmark. *CSEE journal of power and energy systems*, 3, 26−35 (2017).

[5] H. Lund, B. Mathiesen. Energy system analysis of 100% renewable energy systems—The case of Denmark in years 2030 and 2050. *Energy*, 34, 524−531 (2009).

[6] International Energy Agency (IEA). Renewable electricity. *Renewables 2022* (2022). URL: https://www.iea.org/reports/renewables-2022.

[7] I. Perez-Arriaga, C. Batlle. Impacts of intermittent renewables on electricity generation system operation. *Economics of Energy & Environmental Policy*, 1, 3−18 (2012).

[8] H. Ibrahim, A. Ilinca, J. Perron. Energy storage systems—Characteristics and comparisons. *Renewable and sustainable energy reviews*, 12, 1221−1250 (2008).

[9] W. Wang, Q. Luo, B. Li, X. Wei, L. Li, Z. Yang. Recent progress in redox flow battery research and development. *Advanced Functional Materials*, 23, 970−986 (2013).

[10] A. Pimm, T. Cockerill, P. Taylor. The potential for peak shaving on low voltage distribution networks using electricity storage. *Journal of Energy Storage*, 16, 231−242 (2018).

[11] T. Mahlia, T. Saktisahdan, A. Jannifar, M. Hasan, H. Matseelar. A review of available methods and development on energy storage; technology update. *Renewable and sustainable energy reviews*, 33, 532−545 (2014).

[12] C. Parker. Lead–acid battery energy-storage systems for electricity supply networks. *Journal of Power Sources*, 100, 18−28 (2001).

[13] M. Thackeray, C. Wolverton, E. Isaacs. Electrical energy storage for transportation—approaching the limits of, and going beyond, lithium-ion batteries. *Energy & Environmental Science*, 5, 7854−7863 (2012).

[14] C. Ding, H. Zhang, X. Li, T. Liu, F. Xing. Vanadium flow battery for energy storage: prospects and challenges. *The journal of physical chemistry letters*, 4, 1281−1294 (2013).

[15] H. Ferreira, R. Garde, G. Fulli, W. Kling, J. Lopes. Characterisation of electrical energy storage technologies. *Energy*, 53, 288−298 (2013).

[16] C. Roth, J. Noack, M. Skyllas-Kazacos. *History of Flow Batteries. Flow Batteries: From Fundamentals to Applications*, 29−52 (2023).

[17] M. Duduta, B. Ho, V. Wood, P. Limthongkul, V. Brunini, W. Carter, Y. Chiang. Semi-solid lithium rechargeable flow battery. *Advanced Energy Materials*, 1, 511−516 (2011).

[18] K. Lin, Q. Chen, M. Gerhardt, L. Tong, S. Kim, L. Eisenach, A. Valle, D. Hardee, R. Gordon, M. Aziz, M. Marshak. Alkaline quinone flow battery. *Science*, 349, 1529−1532 (2015).

[19] T. Janoschka, N. Martin, U. Martin, C. Friebe, S. Morgenstern, H. Hiller, M. Hager, U. Schubert. An aqueous, polymer-based redox-flow battery using non-corrosive, safe, and low-cost materials. *Nature*, 527, 78−81 (2015).

[20] D. Kwabi, Y. Ji, M. Aziz. Electrolyte lifetime in aqueous organic redox flow batteries: a critical review. *Chemical Reviews*, 120, 6467−6489 (2020).

[21] M. Li, Z. Rhodes, J. Cabrera-Pardo, S. Minteer. Recent advancements in rational design of non-aqueous organic redox flow batteries. *Sustainable Energy & Fuels*, 4, 4370−4389 (2020).

[22] J. Kim, K. Kim, M. Park, N. Lee, U. Hwang, H. Kim, Y. Kim. Development of metal-based electrodes for non-aqueous redox flow batteries. *Electrochemistry Communications*, 13, 997−1000 (2011).

[23] J. Chai, A. Lashgari, X. Wang, C. Williams, All-PEGylated redox-active metal-free organic molecules in non-aqueous redox flow battery. *Journal of Materials Chemistry A*, 8, 15715−15724 (2020).

[24] Z. Li, S. Li, S. Liu, K. Huang, D. Fang, F. Wang, S. Peng. Electrochemical properties of an all-organic redox flow battery using 2, 2, 6, 6-tetramethyl-1-piperidinyloxy and N-methylphthalimide. *Electrochemical and Solid-State Letters*, 14, A171 (2011).

[25] X. Liu, X. Zhang, G. Li, S. Zhang, B. Zhang, W. Ma, Z. Wang, Y. Zhang, G. He. Thienoviologen anolytes for aqueous organic redox flow batteries with simultaneously enhanced capacity utilization and capacity retention. *Journal of Materials Chemistry A*, 10, 9830−9836 (2022).

[26] V. Sentyurin, O. Levitskiy, T. Magdesieva. Molecular design of ambipolar redox-active molecules II: closed-shell systems. *Current Opinion in Electrochemistry*, 24, 6−14 (2020).

[27] B. Huskinson, M. Marshak, C. Suh, S. Er, M. Gerhardt, C. Galvin, X. Chen, A. Aspuru-Guzik, R. Gordon, M. Aziz. A metal-free organic–inorganic aqueous flow battery. *Nature*, 505, 195−198 (2014).

[28] A. Hollas, X. Wei, V. Murugesan, Z. Nie, B. Li, D. Reed, J. Liu, V. Sprenkle, W. Wang. A biomimetic high-capacity phenazine-based anolyte for aqueous organic redox flow batteries. *Nature Energy*, 3, 508−514 (2018).

[29] E. Beh, D. Porcellinis, R. Gracia, K. Xia, R. Gordon, R, M. Aziz. A neutral pH aqueous organic–organometallic redox flow battery with extremely high capacity retention. *ACS Energy Letters*, 2, 639−644 (2017).

[30] T. Liu, X. Wei, Z. Nie, V. Sprenkle, W. Wang. A total organic aqueous redox flow battery employing a low cost and sustainable methyl viologen anolyte and 4-HO-TEMPO catholyte. *Advanced Energy Materials*, 6, 1501449 (2016).

[31] Y. Ding, G. Yu. The promise of environmentally benign redox flow batteries by molecular engineering. *Angewandte Chemie International Edition*, 56, 8614−8616 (2017).

[32] D. Kwabi, K. Lin, Y. Ji, E. Kerr, M. Goulet, D. Porcellinis, D. Tabor, D. Pollack, A. Aspuru-Guzik, R. Gordon, M. Aziz. Alkaline quinone flow battery with long lifetime at pH 12. *Joule*, 2, 1894−1906 (2018).

[33] N. Hagedom. DOE/NASA/12726-24. NASA TM-836 (1984).

[34] K. Gong, F. Xu, J. Grunewald, X. Ma, Y. Zhao, S. Gu, Y. Yan. All-soluble all-iron aqueous redox-flow battery. *ACS Energy Letters*, 1, 89−93 (2016).

[35] H. Zhang, C. Sun. Cost-effective iron-based aqueous redox flow batteries for large-scale energy storage application: A review. *Journal of Power Sources*, 493, 229445 (2021).

[36] Q. Lai, H. Zhang, H., X. Li, L. Zhang, Y. Cheng. A novel single flow zinc–bromine battery with improved energy density. *Journal of Power Sources*, 235, 1−4 (2013).

[37] L. Guo, H. Guo, H. Huang, S. Tao, Y. Cheng. Inhibition of zinc dendrites in zinc-based flow batteries. *Frontiers in chemistry*, 8, 557 (2020).

[38] M. Skyllas-Kazacos, M. Rychcik, R. Robins, A. Fane, M. Green. New all-vanadium redox flow cell. *Journal of the electrochemical society*, 133, 1057 (1986).

[39] K. Lourenssen, J. Williams, F. Ahmadpour, R. Clemmer, S. Tasnim. Vanadium redox flow batteries: A comprehensive review. *Journal of Energy Storage*, 25, 100844 (2019).

[40] H. Bindner, C. Ekman, O. Gehrke, F. Isleifsson. Characterization of Vanadium Flow Battery. *Risø-R-Report* (2010). URL: http://orbit.dtu.dk/files/5889861/ris-r-1753.pdf.

[41] Á. Cunha, J. Martins, N. Rodrigues, F. Brito. Vanadium redox flow batteries: a technology review. *International Journal of Energy Research*, 39, 889−918 (2015).

[42] M. Guarnieri, P. Mattavelli, G. Petrone, G. Spagnuolo. Vanadium redox flow batteries: Potentials and challenges of an emerging storage technology. *IEEE Industrial Electronics Magazine*, 10, 20−31 (2016).

[43] J. Noack, L. Wietschel, N. Roznyatovskaya, K. Pinkwart, J. Tübke. Techno-Economic Modeling and Analysis of Redox Flow Battery Systems. *Energies*, 9, 627 (2016).

[44] R. Dmello, J. Milshtein, F. Brushett, K. Smith. Cost-driven materials selection criteria for redox flow battery electrolytes. *Journal of Power Sources*, 330, 261−272 (2016).

[45] V. Viswanathan, A. Crawford, D. Stephenson, S. Kim, W. Wang, B. Li, G. Coffey, E. Thomsen, G. Graff, P. Balducci, M. Kintner-Meyer, V. Sprenkle. Cost and performance model for redox flow batteries. *Journal of Power Sources*, 247, 1040−1051 (2014).

[46] A. Parasuraman, T. Lim, C. Menictas, M. Skyllas-Kazacos. Review of material research and development for vanadium redox flow battery applications. *Electrochimica Acta*, 101, 27−40 (2013).

[47] G. Kear, A. Shah, F. Walsh. Development of the all-vanadium redox flow battery for energy storage: a review of technological, financial and policy aspects. *International journal of energy research*, 36, 1105−1120 (2012).

[48] M. Skyllas-Kazacos, G. Kazacos, G. Poon, H. Verseema. Recent advances with UNSW vanadium-based redox flow batteries. *International Journal of Energy Research*, 34, 182−189 (2010).

[49] L. Su, A. Badel, C. Cao, J. Hinricher, F. Brushett. Toward an inexpensive aqueous polysulfide–polyiodide redox flow battery. *Industrial & Engineering Chemistry Research*, 56, 9783−9792 (2017).

[50] T. Li, F. Xing, T. Liu, J. Sun, D. Shi, H. Zhang, X. Li. Cost, performance prediction and optimization of a vanadium flow battery by machine-learning. *Energy & Environmental Science*, 13, 4353−4361 (2020).

[51] A. Forner-Cuenca, F. Brushett. Engineering porous electrodes for next-generation redox flow batteries: recent progress and opportunities. *Current Opinion in Electrochemistry*, 18, 113−122 (2019).

[52] H. Jiang, J. Sun, L. Wei, M. Wu, W. Shyy, T. Zhao. A high power density and long cycle life vanadium redox flow battery. *Energy Storage Materials*, 24, 529−540 (2020).

[53] J. Luo, A. Sam, B. Hu, C. DeBruler, X. Wei, W. Wang, T. Liu. Unraveling pH dependent cycling stability of ferricyanide/ferrocyanide in redox flow batteries. *Nano Energy*, 42, 215−221 (2017).

[54] N. Roznyatovskaya, T. Herr, M. Küttinger, M. Fühl, J. Noack, K. Pinkwart, J. Tübke. Detection of capacity imbalance in vanadium electrolyte and its electrochemical regeneration for all-vanadium redox-flow batteries. *Journal of Power Sources*, 302, 79−83 (2016).

[55] Z. He, Y. Lv, T. Zhang, Y. Zhu, L. Dai, S. Yao, W. Zhu, L. Wang. Electrode materials for vanadium redox flow batteries: Intrinsic treatment and introducing catalyst. *Chemical Engineering Journal*, 427, 131680 (2022).

[56] W. Carvalho Jr, L. Cassayre, D. Quaranta, F. Chauvet, R. El-Hage, T. Tzedakis, B. Biscans. Stability of highly supersaturated vanadium electrolyte solution and characterization of precipitated phases for vanadium redox flow battery. *Journal of Energy Chemistry*, 61, 436−445 (2021).

[57] K. Rho, S. Yoon, J. Ryu, S. Cho, M. Kim, D. Kim. Study on thermal behavior of vanadium redox flow battery at low temperature to prevent precipitation. *Journal of Energy Storage*, 49, 104110 (2022).

[58] S. Roe, C. Menictas, M. Skyllas-Kazacos. A high energy density vanadium redox flow battery with 3 M vanadium electrolyte. *Journal of The Electrochemical Society*, 163, A5023 (2015).

[59] A. Mousa, M. Skyllas-Kazacos. Effect of additives on the low-temperature stability of vanadium redox flow battery negative half-cell electrolyte. *ChemElectroChem*, 2, 1742−1751 (2015).

[60] B. Jiang, L. Wu, L. Yu, X. Qiu, J. Xi. A comparative study of Nafion series membranes for vanadium redox flow batteries. *Journal of Membrane Science*, 510, 18−26 (2016).

[61] J. Xi, Z. Wu, X. Qiu, L. Chen. Nafion/SiO_2 hybrid membrane for vanadium redox flow battery. *Journal of Power Sources*, 166, 531−536 (2007).

[62] C. Lin, M. Yang, H. Wei. Amino-silica modified Nafion membrane for vanadium redox flow battery. *Journal of Power Sources*, 282, 562−571 (2015).

[63] X. Teng, J. Dai, J. Su, Y. Zhu, H. Liu, Z. Song. A high performance polytetrafluoroethene/Nafion composite membrane for vanadium redox flow battery application. *Journal of Power Sources*, 240, 131−139 (2013).

[64] X. Li, H. Zhang, Z. Mai, H. Zhang, I. Vankelecom. Ion exchange membranes for vanadium redox flow battery (VRB) applications. *Energy & Environmental Science*, 4, 1147−1160 (2011).

[65] S. Yan, X. Chu, B. Xue, T. Lv, B. Lin, Z. Zhang. Polyether Ether Ketone-Based Anion Exchange Membranes with Bis-imidazolium Cations for All-Vanadium Redox Flow Batteries. *ACS Applied Energy Materials*, 4, 6787−6796 (2021).

[66] Z. Yuan, X. Li, Y. Zhao, H. Zhang. Mechanism of polysulfone-based anion exchange membranes degradation in vanadium flow battery. *ACS applied materials & interfaces*, 7, 19446−19454 (2015).

[67] D. Chen, H. Qi, T. Sun, C. Yan, Y. He, C. Kang, Z. Yuan, X. Li. Polybenzimidazole membrane with dual proton transport channels for vanadium flow battery applications. *Journal of Membrane Science*, 586, 202−210 (2019).

[68] R. Wang, Y. Li. Carbon electrodes improving electrochemical activity and enhancing mass and charge transports in aqueous flow battery: Status and perspective. *Energy Storage Materials*, 31, 230−251 (2020).

[69] R. Banerjee, N. Bevilacqua, A. Mohseninia, B. Wiedemann, F. Wilhelm, J. Scholta, R. Zeis. Carbon felt electrodes for redox flow battery: Impact of compression on transport properties. *Journal of Energy Storage*, 26, 100997 (2019).

[70] Z. Zhang, J. Xi, H. Zhou, X. Qiu. KOH etched graphite felt with improved wettability and activity for vanadium flow batteries. *Electrochimica Acta*, 218, 15−23 (2016).

[71] A. Pezeshki, J. Clement, G. Veith, T. Zawodzinski, M. Mench. High performance electrodes in vanadium redox flow batteries through oxygen-enriched thermal activation. *Journal of Power Sources*, 294, 333−338 (2015).

[72] X. Zhou, T. Zhao, Y. Zeng, L. An, L. Wei. A highly permeable and enhanced surface area carbon-cloth electrode for vanadium redox flow batteries. *Journal of Power Sources*, 329, 247−254 (2016).

[73] C. Minke, U. Kunz, T. Turek. Carbon felt and carbon fiber-A techno-economic assessment of felt electrodes for redox flow battery applications. *Journal of Power Sources*, 342, 116−124 (2017).

[74] D. Aaron, Q. Liu, Z. Tang, G. Grim, A. Papandrew, A. Turhan, T. Zawodzinski, M. Mench. Dramatic performance gains in vanadium redox flow batteries through modified cell architecture. *Journal of Power sources*, 206, 450−453 (2012).

[75] X. Ke, J. Prahl, J. Alexander, J. Wainright, T. Zawodzinski, R. Savinell. Rechargeable redox flow batteries: flow fields, stacks and design considerations. *Chemical Society Reviews*, 47, 8721−8743 (2018).

[76] V. Muñoz-Perales, P. García-Salaberri, A. Mularczyk, S. Ibáñez, M. Vera, A. Forner-Cuenca, *ChemRxiv* (2023), https://doi.org/10.26434/chemrxiv-2023-2zthc.

[77] J. Milshtein, K. Tenny, J. Barton, J. Drake, R. Darling, F. Brushett. Quantifying Mass Transfer Rates in Redox Flow Batteries. *Journal of The Electrochemical Society*, 164, E3265–E3275 (2017).

[78] T. Wang, J. Fu, M. Zheng, Z. Yu. Dynamic control strategy for the electrolyte flow rate of vanadium redox flow batteries. *Applied Energy*, 227, 613–623 (2018).

[79] I. Mayrhuber, C. Dennison, V. Kalra, E. Kumbur. Laser-perforated carbon paper electrodes for improved mass transport in high power density vanadium redox flow batteries. *Journal of Power Sources*, 260, 251–258 (2014).

[80] C. Xu, X. Li, T. Liu, H. Zhang. Design and synthesis of a free-standing carbon nano-fibrous web electrode with ultra large pores for high-performance vanadium flow batteries. *RSC advances*, 7, 45932–45937 (2017).

[81] M. León, L. Castañeda, A. Márquez, F. Walsh, J. Nava. Review—Carbon Cloth as a Versatile Electrode: Manufacture, Properties, Reaction Environment, and Applications. *Journal of The Electrochemical Society*, 169, 053503 (2022).

[82] A. Forner-Cuenca, E. Penn, A. Oliveira, F. Brushett. Exploring the Role of Electrode Microstructure on the Performance of Non-Aqueous Redox Flow Batteries. *Journal of The Electrochemical Society*, 166, A2230–A2241 (2019).

[83] A. Wong, M. Aziz. Method for Comparing Porous Carbon Electrode Performance in Redox Flow Batteries. *Journal of The Electrochemical Society*, 167, 110542 (2020).

[84] K. Greco, A. Forner-Cuenca, A. Mularczyk, J. Eller, F. Brushett. Elucidating the Nuanced Effects of Thermal Pretreatment on Carbon Paper Electrodes for Vanadium Redox Flow Batteries. *ACS Applied Materials & Interface*, 10, 44430−44442 (2018).

[85] L. Yue, W. Li, F. Sun, L. Zhao, L. Xing. Highly hydroxylated carbon fibers as electrode materials of all-vanadium redox flow battery. *Carbon*, 48, 3079−3090 (2010).

[86] Y. Zhao, L. Yu, X. Qiu, J. Xi. Carbon layer-confined sphere/fiber hierarchical electrodes for efficient and durable vanadium flow batteries. *Journal of Power Sources*, 402, 453–459 (2018).

[87] Z. Zhang, J. Xi, H. Zhou, X. Qiu. KOH etched graphite felt with improved wettability and activity for vanadium flow batteries. *Electrochimica Acta*, 218, 15−23 (2016).

[88] J. Sun, M. Zheng, Y. Luo, Z. Yu. Three-dimensional detached serpentine flow field design for redox flow batteries. *Journal of Power Sources*, 428, 136–145 (2019).

[89] S. Tsushima, T. Suzuki. Modeling and simulation of vanadium redox flow battery with interdigitated flow field for optimizing electrode architecture. *Journal of The Electrochemical Society*, 167, 020553 (2020).

[90] S. Kumar, S. Jayanti. Effect of flow field on the performance of an all-vanadium redox flow battery. *Journal of Power Sources*, 307, 782–787 (2016).

[91] P. Ghimirea, A. Bhattarai, R. Schweiss, G. Scherer, N. Wai, Q. Yan. A comprehensive study of electrode compression effects in all vanadium redox flow batteries including locally resolved measurements. *Applied Energy*, 230, 974–982 (2018).

[92] Y. Yao, J. Lei, Y. Shi, F. Ai, Y. Lu. Assessment methods and performance metrics for redox flow batteries. Nature Energy, 6, 582−588 (2021).

[93] Y. Gandomi, D. Aaron, J. Houser, M. Daugherty, J. Clement, A. Pezeshki, T. Ertugrul, D. Moseley, M. Mench. Critical review—experimental diagnostics and material characterization techniques used on redox flow batteries. *Journal of The Electrochemical Society*, 165, A970 (2018).

[94] R. Levie. On porous electrodes in electrolyte solutions: I. Capacitance effects. *Electrochimica Acta*, 8, 751–780 (1963).

[95] A. Pezeshki, R. Sacci, F. Delnick, D. Aaron, M. Mench. Elucidating effects of cell architecture, electrode material, and solution composition on overpotentials in redox flow batteries. *Electrochimica Acta*, 229, 261–270 (2017).

[96] J. Landesfeind, J. Hattendorff, A. Ehrl, W. Wall, H. Gasteiger. Tortuosity Determination of Battery Electrodes and Separators by Impedance Spectroscopy. *Journal of The Electrochemical Society*, 163, A1373–A1387 (2016).

[97] C. Sun, F. Delnick, D. Aaron, A. Papandrew, M. Mench, T. Zawodzinski. Resolving losses at the negative electrode in all-vanadium redox flow batteries using

electrochemical impedance spectroscopy. *Journal of The Electrochemical Society*, 161, A981 (2014).

[98] J. Brug, A. van der Eeden, M. Sluyters-Rehbach, J. Sluyters. The analysis of electrode impedances complicated by the presence of a constant phase element. *Journal of Electroanalytical Chemistry and Interfacial Electrochemistry*, 176 (1984) 275–295.

Chapter 2

Morphological Properties and Electrochemical Performance for Compressed Carbon-fiber Electrodes in Redox Flow Batteries

Baichen Liu[a], Søren Bredmose Simonsen[a], Johan Hjelm[a*]

[a] Department of Energy Conversion and Storage, Technical University of Denmark
Building 310, DK-2800 Kgs. Lyngby, Denmark

[*] Corresponding author: johh@dtu.dk

Abstract

Recognizing the urgent need for further cost reduction to drive deep penetration of redox flow batteries as grid-scale stationary energy storage systems in the global energy mix, it is critical to improve reactor performance to bring down the high capital cost. As one of the main contributors to the overall internal resistance, porous electrodes with properly designed microstructure and optimized physiochemical properties are preferable for boosting electrochemical and fluid dynamic performance. The present study aims to unveil the relationship between electrode morphology and electrochemical performance under varying electrode compression. Three representative, commercially available, carbon-fiber electrodes (i.e., paper, felt, and cloth) with distinct microstructures were selected here, and a comprehensive study was conducted to compare morphology, hydraulic permeability, mechanical behavior, electrochemical properties including decoupled kinetic and mass transport resistances, and overall battery performance in a lab-scale vanadium redox flow battery at 0-50% compression ratios. The 3D electrode morphology was characterized through X-ray computed tomography and the extracted key microstructure parameters (e.g., surface area and tortuosity) were compared with corresponding electrochemically

determined parameters. It was found that the cloth possessed a bimodal pore size distribution due to its distinct woven microstructure and that it was sensitive to the applied compression. The large pores formed at the intersections between fiber bundles collapsed under excessive compression, which greatly reduced the advantageous high permeability and low mass transport resistances characteristic of the uncompressed cloth. The paper electrodes exhibited a strongly growing compression force accompanied by increased in-plane tortuosity and mass transport resistance even at low compression (<20%). During battery operation, the cloth maintains a good balance between performance and pressure drop at moderate compression. The optimal trade-off between fluid dynamics and electrochemical performance occurred at the compression ratios of 30%, 20%, and 20% for the felt, paper, and cloth, respectively.

2.1 Introduction

Energy storage systems are of great importance for overcoming the instability associated with the incorporation of large amounts of intermittent renewables in the power mix [1]. Scalable, low-cost, and high-performance energy storage systems will accelerate the global transition to a society powered by sustainable renewable energy sources [2]. Redox flow batteries (RFB) have attracted great attention for stationary grid-scale energy storage in recent years due to their unique architecture with decoupled energy and power ratings [3]. Unlike most batteries, the energy of RFB is stored using active materials dissolved in liquid or semi-solid [4] electrolytes and stored in external tanks, while the power output is determined by the size of the battery stack. Such modular flexibilities make RFB more suitable to scale-up (e.g., ranging from kW/kW·h to MW/MW·h [5]) with long lifespans (e.g., >10,000 cycles, ~10-20 years [6]) compared to other batteries with fixed energy to power ratio. In recent years, great efforts have been placed in the improvement of critical components in RFB systems, including the development of organic redox couples with low degradation [7], highly selective novel membranes [8], eco-friendly catalysts [9], etc. However, high system costs are still among the main barriers to wider market adoption, and further cost reduction is needed to meet the capital expense target of \$100-150/(kW·h) set by the U.S. Department of Energy [10].

According to a cost analysis of a 10 kW/120 kW·h vanadium redox flow battery (VRFB) system, the stack cost accounts for the highest proportion, and it is directly influenced by internal resistances and system efficiency [11]. Porous electrodes are critical components within modern electrochemical flow reactors and flow battery stacks. They provide space for electrochemical reactions and pathways for charge and mass transport [12]. Electrodes with high active specific surface area and facile electrolyte transport pathways will largely bring down kinetic overpotentials, concentration overpotentials, and pressure drops during battery operation. Commercial porous electrodes used in RFBs include carbon paper [13], carbon felt [14], and carbon cloth [15]. Despite the advantages of a highly porous internal structure and good chemical stability, the inertness and hydrophobicity of pristine carbon electrodes significantly influence the overall cell resistance. Pre-treatment (e.g., thermal treatment [16][17], acid treatment [18], etc.) and surface modification [19] approaches are commonly adopted to enhance the active surface area and hydrophilicity of such electrodes. However, these methods have only a minor impact on improving the mass transfer properties due to the original characteristics of low-hierarchical fiber orientations for these electrodes. The mass transfer process has been recognized as an important performance-limiting factor, especially for applications using fast-kinetic redox couples [20]. Enhancing the applied flow rate is a way to reduce the diffusion distance [21] through a decreased effective depletion layer thickness. Although valid, it comes at the expense of pumping energy expenditure, which may result in decreased system efficiency at high flow rates. Apart from this, some efforts have been focused on electrode physical structure modifications to mitigate the transport issues. Carbon paper with laser-perforated macro-pores (i.e., ~200-500 μm [22]) was developed and combined with different flow fields [23] to increase the penetration of electrolytes. Multi-layer carbon paper assemblies with different porosity from the flow field side to the membrane side [24][25] and multi-segmented carbon felts with different properties from the inlet to the outlet side [26][27][28] were investigated for more even through-plane and in-plane electrolyte flow distributions, respectively. In addition, some manually carved open [29][30] and cross-poked [31] macro-channels (e.g., 2 mm of the channel width [31]) on carbon felt proved to be beneficial to battery performance. These methods created macro-passageways on the electrodes by sacrificing some substance, which can help to reduce the pressure drop. Yet, it remains a challenge to understand the balance between the electrochemical reaction kinetics and micro-scale mass transfer processes, which is essential for an optimized trade-off.

Electrode microstructure plays a key role in electrochemical performance. Ideally, high-performance electrodes need to incorporate both nano-scale pores (e.g., ~20 nm) for providing a large number of reaction sites, and interconnected micro-scale pores (e.g., ~20 μm) with low tortuosity for low pressure drop and uniform flow distribution of the electrolytes [32]. Electrodes with hierarchical, multi-scale pore microstructures [33] have been verified to balance kinetics and mass transfer effectively. Unveiling the relationship between electrode microstructure and electrochemical performance can provide guidelines for bottom-up designs for next-generation advanced electrodes with unique structures using novel manufacturing processes, such as 3D printing [34], electrospinning [35], and phase separation [36]. Currently, the most straightforward technique for microstructural characterization is scanning electron microscopy (SEM). It can be used to qualitatively visualize electrode surface morphology (such as fiber diameter, pore structure, etc.). Several groups compared electrode morphology and battery performance using off-the-shelf carbon-fiber electrodes. For instance, Forner-Cuenca et al. [37] compared three different types of electrodes (i.e., carbon paper, carbon felt, and carbon cloth) in a non-aqueous RFB. Tenny et al. [38] and Wong et al. [39] compared the physical and electrochemical properties of carbon cloth electrodes with different interwoven patterns to identify the relationship among structure, hydraulic permeability, and electrochemical resistive losses. Recently, Wong et al. [40] proposed an in-situ, direct visualization method by fluorescence microscopy to capture real-time mass transport processes and heterogeneous behavior in carbon papers. To better understand the structure-function relations, simulations were introduced to gain insight into independent electrode parameters on cell performance. They included the adoption of battery-scale 2D and 3D finite element methods [41], pore network models [42][43], and a Lattice-Boltzmann model (LBM) [44]. For instance, Cheng et al. [41] reported that the volumetric area of an electrode has the largest positive correlation with current density output compared to electrode thickness and porosity. Although resolved information was provided, the results were difficult to validate considering the simplification and the difference between the artificial model and realistic microstructures.

X-ray computed tomography is a strong, non-destructive method to capture 3D realistic microstructure under sub-micron resolution (e.g., ~1 μm [45]). It has been widely used across science and engineering fields [46], and also in engineered porous materials [47] to inspect the structural quality. It provides more comprehensive morphological properties (such as porosity, volumetric specific surface area, tortuosity, etc.) of porous materials compared to SEM. Also, the reconstructed images can be further used as concrete objectives in LBM studies [48][49]. Kok et al. [50] investigated the dimensional heterogeneity of electrospun carbon fibrous mat using X-ray tomography combined with LBM to evaluate permeability results. Jervis et al. [51] used an in-situ compression rig in X-ray tomography to determine the non-linear physical characteristics of carbon felt from 0-90% compression ratios. Some studies correlated these features with electrochemical performance in operational flow batteries. For example, Simon et al. [52] combined image analysis with experimental hydraulic permeability on carbon paper and carbon cloth electrodes at ~20% compression ratios in a non-aqueous RFB. They reported that the carbon cloth showed the highest performance on account of its periodic woven alignment and unique bimodal pore distributions.

As an important operational variable in RFB, applying certain compression to the electrode can effectively increase the contact areas to the bipolar plates [53]. Excessive compression destroys the pore structures and leads to a deterioration of mass transfer properties [54]. Numerous studies, mostly focused on carbon felt [55][56][57], have been conducted on varying compression ratios on electrode mechanical properties [58], permeability [59][60], battery performance with [61] or without flow fields [62], and structure optimizations [27][63][64]. Tenny et al. [65] recently reported compressive effects on carbon paper and carbon cloth electrodes. Under ideally uniform compression, the pore size within a porous electrode shrinks without major impacts on individual fibers. This is a way to investigate the impact of porosity changes in a single type of microstructure on the electrochemical mass transport properties, and on the overall battery performance. Hence, the present study selected three binder-free commercial electrodes (SGL GFD 2.5 EA, Freudenberg H23, and AvCarb 1186 HCB) as representatives for the distinctive microstructure of carbon felt, carbon paper, and carbon cloth. We comprehensively compared morphological properties, mechanical behavior, fluid dynamics, electrochemical, and overall battery performance for the three electrodes at a broad range of compression ratios from 0-50% used in practical

RFB applications. Specifically, porosity, pore size and pore size distribution, surface area, and tortuosity were captured through image analysis before and after compression. We achieved the same compression conditions in an operational VRFB cell and investigated the effects of the compression-induced microstructural changes on electrochemical performance. Electrochemical impedance spectroscopy (EIS) was employed in this work and interpreted using an equivalent circuit model consisting of a transmission-line to model the porous electrodes in the absence and presence of faradaic reactions, i.e. under blocking and non-blocking conditions. Kinetic and mass transport resistances were decoupled and extracted using complex non-linear least squares fitting. Moreover, we evaluated electrochemical active surface area (ECSA) and through-plane tortuosity via EIS under blocking conditions and compared the results with microstructural parameters obtained from image analysis of X-ray CT data obtained at different compression ratios. Finally, cycling tests were conducted at the best-performing compression ratio for each electrode under varying current densities to examine battery performance. To summarize, the objective of the present study is to elucidate the relationship of compression-induced electrode microstructure changes and its influence on electrochemical kinetics and mass transport.

2.2 Experimental

2.2.1 Electrode material

Three commercially available carbon-fiber electrodes were selected as typical representatives of different types of electrodes: SGL GFD 2.5 EA carbon felt, Freudenberg H23 carbon paper, and AvCarb 1186 HCB carbon cloth. The electrodes were cut to squares with areas of 5 cm^2 for battery assembly. Optical photographs of the prepared samples are shown in Fig. 2.1. All the carbon electrodes were hydrophobic as received. To make sure the electrodes were hydrophilic before use, each electrode was thermally treated at 400 °C for 24 hours in air atmosphere [17]. Multiple studies [16][17] have been carried out on the impact of activation temperature and duration time of thermal treatment on carbon electrodes. The fiber diameter and used pyrolysis temperature varies significantly for different commercial electrodes, which is why there is not a single optimal pretreatment procedure for all carbon electrodes. In the present study, we placed emphasis on the effect of compression on performance and pressure drop, and therefore chose a single electrode activation process for all the three electrodes to obtain satisfactory wettability. Microstructural data determined using SEM imaging as well as specific surface areas determined using gas adsorption of the three selected electrodes before and after thermal treatment can be found in *Supplementary Information* (Fig. S2.1 and Table S2.1).

2.2.2 Battery assembly under compression

A schematic diagram of the employed single-cell VRFB reactor is shown in Fig. 2.1(a). The battery reactor was constructed using hardware obtained from Fuel Cell Technologies, Inc (Albuquerque, NM). In the present study, the prepared electrode samples were placed in the cavity of the polytetrafluoroethylene (PTFE) gaskets on both positive and negative sides, which were separated by a perfluorinated cation exchange membrane (Fumasep FS-950, Fumatech BWT GmbH). The membrane was placed in the reactor without any pretreatment. The dry thickness of the membrane was 50 μm. Two flow plates (Resin B347B graphite) with flow-through flow-field (FT-FF) designs were placed on either side of the cell. Two gold-plated copper current collectors, with one side covered by an insulating layer, were placed in contact with the flow plates. All of the components were clamped and tightened together by two brass end plates with 8 bolts and nuts. A torque wrench was adopted to ensure that all bolts were tightened with a constant 8 N·m torque in each test.

To control the compression ratios for the different electrodes, PTFE gaskets with thicknesses of 25, 50, 100, 200, 500, and 1000 μm were cut to size. Different CR of the three types of electrodes could be achieved by using combinations of different thickness PTFE gaskets. In the present study, we selected a broad range of CR from 0% to 50%, and compare the morphological properties and electrochemical performance of the investigated electrodes under the same range of CR. The deviations of CR for the three electrodes are within ±1.5%. A schematic of the CR control method is shown in Fig. 2.1(b). It is noted that the thickness of uncompressed Freudenberg H23 paper is only 210 μm. To precisely control the CR, we used 3-layer paper electrodes in the battery assembly (3×210 μm), which is also the recommended number of layers for carbon paper [66] to ensure sufficient ECSA.

Due to that the PTFE gaskets were much harder to compress compared to porous carbon-fiber electrodes, the electrodes could be uniformly compressed to the thickness of the PTFE gaskets under FT-FF designs. The compression ratios (CRs) were calculated using the following expression:

$$CR = (1 - \frac{L_c}{L_0}) \times 100\% \tag{2.1}$$

where L_c denotes electrode thickness after compression;

and L_0 denotes original electrode thickness before compression.

During operation, the vanadium electrolytes (OXKEM, containing 1.61 mol/L vanadium active species, 4.05 mol/L sulphate, and 0.05 mol/L phosphoric acid) were stored in two sealed external glass bottles outside the flow cell. The vanadium species in the original electrolyte consisted of 50% V^{3+} and 50% VO^{2+}. The electrolytes were circulated between the bottles and cell using a peristaltic pump (Shenchen LabV1) fitted with a dual-channel four-roller pump head (Masterflex L/S Easy-Load II). Perfluoroalkoxy alkane (PFA) tubing (Swagelok, PFA-T2-030-100) and tube fittings (Swagelok, PFA-220-9) were used in the set-up, and the pump tubing consisted of a #16 rubber tube (Tygon, A-60-G). A flow pulsation dampener (KNF FPD 06) was placed between the battery inlet and peristaltic pump on each side of the cell. All of the experiments were conducted in a sealed cabinet with continuous flow of argon to prevent oxidation of V^{2+} [67] at room temperature. The oxygen partial pressure in the cabinet was below 0.1% during the tests. The electrolytes were purged with argon for at least 5 min to remove residual air before sealed in the bottles, and the cabinet was sealed and left for at least 30 min while flushing with argon before the measurements started. All of the cables were passed through the cabinet wall using sealed cable entry frames (KEL-ER 10/6) and were connected to a Bio-Logic SP-300 potentiostat.

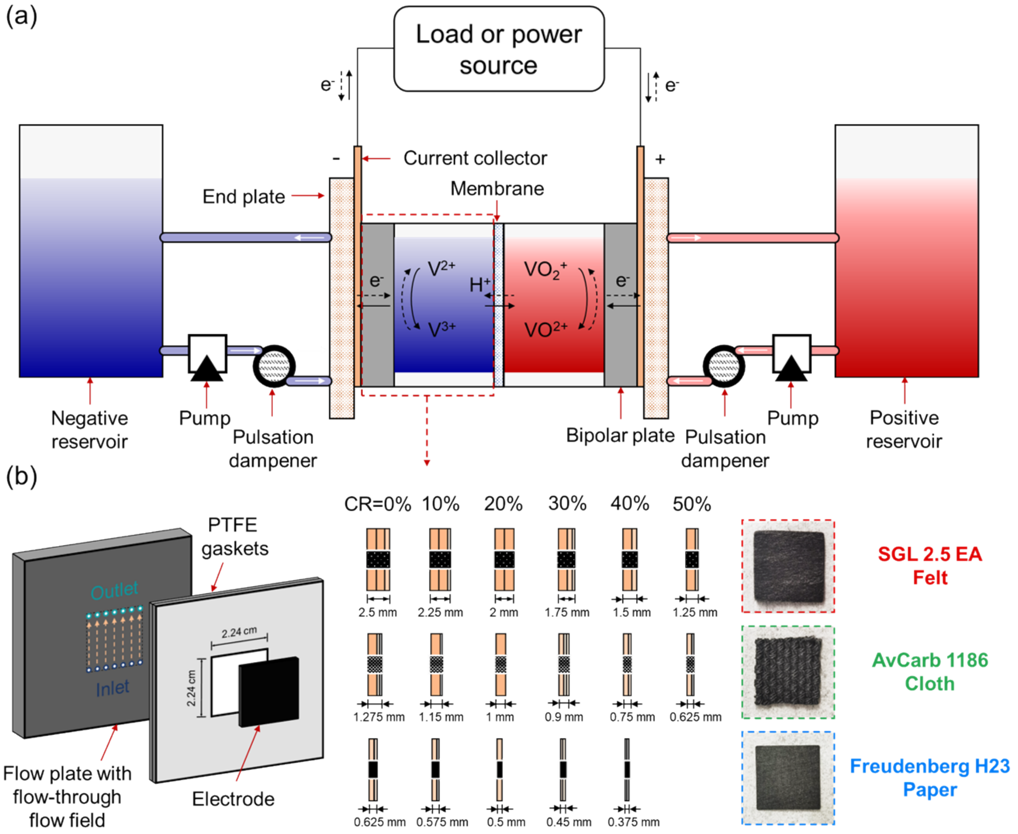

Figure 2.1 (a) Schematics of the VRFB single-cell setup; (b) schematic of the method to control the electrode compression ratio with FT-FF flow field pattern and optical photographs of the carbon-based electrode samples adopted in this study.

2.2.3 Electrode morphology characterization

X-ray micro-computed tomography (μ-CT) was adopted to acquire the 3D microstructure images for the three electrodes under varying CRs. A ZEISS XRadia 410 Versa with a tungsten target was used for the measurements in the present study. To mimic the compression status in a practical flow battery, electrode samples were approximately cut to a circular shape with 1 cm diameter, and then were placed in a custom-built compression tool which was made of a cylindrical transparent polycarbonate (PC) tube (1 mm of the wall thickness) assembled with a micrometer screw to apply the mechanical force. A photo of the compression tool in the X-ray μ-CT is displayed in Fig. S2.2. A glued plastic plug was placed at the end of the tube. On the top of the end plug, the samples were placed and sandwiched between two incompressible plastic plates (2 mm thickness). The relatively low attenuation from these plates ensured minimal shadowing from the plate to the sample in the cone beam geometry. The radiograms were shown in *Supplementary Information* (Fig. S2.3). An aluminum piston was used between the plastic plate and micrometer screw to adjust height and apply the compressive force. Knowing the original thickness of each electrode samples, the CR was controlled through the micrometer screw to manually adjust the distance to the required compressed thickness of each electrode. After assembling the compression tool with electrode samples, the apparatus was mounted vertically on a sample holder between the X-ray source and detector without any additional filter (air filter). The sample holder was rotated for 360 degrees during X-ray scanning, and electrode morphological information was captured. In the present study, a source voltage of 40 kV and a power of 10 W were adopted. For the detector, the 4X objective was used and the relative source-sample-detector distances were adjusted to give a pixel size of 4.12 μm. This was a compromise between obtaining sufficient spatial resolution and the largest possible field of view. The scanning was performed in a 2x2 binning mode for an exposure time of 3 seconds to acquire 2401 projections. The recorded data were reconstructed using a Feldkamp-Davis-Kress algorithm. The commercial software Avizo was used for processing the reconstructed data and quantification of the morphological properties (porosity, specific surface area, etc.). Symmetric nearest neighbor (SNN) filter with a neighborhood size of 3 pixels was introduced to remove noise. Example histograms before and after SNN filter was shown in Fig. S2.4. Segmentation was performed by using a global threshold where the threshold was half between the histogram peaks representing the two phases, fibers and air. Isolated islands <50 voxels were removed. To evaluate the quality of the segmentation, the raw constructed data was compared with the slice after segmentation in Fig. S2.5. After segmentation, quantitative analysis was performed in Avizo. Volume fractions were extracted directly by counting the voxels of each phase, while surface areas were extracted after generating a triangular mesh surface form the segmentation. To estimate measuring errors in the quantitative analysis, upper and lower limits were determined by manual adjustment of the global threshold until the segmentation became clearly unreasonable as evaluated from slice images.

The specific surface area for uncompressed electrodes acquired through X-ray μ-CT techniques were also compared to the results from other approaches, i.e., ECSA (determined in Section 2.2.6) measurements, Brunauer-Emmett-Teller (BET) measurements, and theoretical cylindrical filament model [38]. Among them, BET measurements were conducted using an Autosorb-1 equipment. Electrode samples were approximately cut to ~0.1 g and sent to measure the specific surface area. The cylindrical filament model was used for volumetric specific surface area (α_V) prediction assuming that all of the carbon fibers were smooth and cylindrical without any intersections, which could be expressed as follows [38]:

$$\alpha_V = \frac{4(1-\varepsilon)}{d_f} \qquad (2.2)$$

where ε denotes electrode porosity;
and d_f denotes fiber diameter.

In addition, the uncompressed electrode surface morphology was also captured through a Carl Zeiss Merlin field-emission SEM under the acceleration voltage of 5 kV. Images were captured on a secondary detector at multiple magnifications. The average fiber diameters of the three electrodes were measured at magnifications of 20,000 X in the through-plane perspective.

2.2.4 Mechanical strain-stress characterization

The mechanical strain-stress curves were measured using a material testing machine (Zwick/Roell Z030) under compression mode at room temperature. The electrode samples were cut to the same geometric sizes used in battery tests (5 cm^2) and placed on a stainless-steel plate. The moving-magnet motor was fixed at the position where the electrodes remained at the original thickness as 0% CR for zero-point correction, and started compression load until reaching the calculated distance for 60% CR. The load rate was set to 0.2 mm/s for each test, and the maximum compression loading force was 4 kN.

2.2.5 Pressure drop measurements

To evaluate the actual electrode pressure drop and permeability during battery operation, the single-cell flow battery setup was used in the pressure drop measurements. The two flow pulsation dampeners were removed to avoid any external influence on the observed pressure changes. Instead, four pressure sensors (from Grundfos Direct Sensors^{TM}, RPS 0-1) were placed at the inlet and outlet of the battery on both sides and connected with a USB multifunction DAQ device (LabJack U6) to collect the signal from each sensor. The pristine vanadium electrolyte (1.61 mol/L $V^{3.5+}$, 4.05 mol/L SO_4^{2-}, and 0.05 mol/L PO_4^{3-}) was selected as the working fluid for both positive and negative sides in all of the pressure drop tests. The pressure drop of the empty cell (flow cell without electrodes) were excluded in each test, to isolate the pressure drop generated by the electrodes. The pressure drop measurements for the three electrodes were collected in the volumetric flow rate range of 0-25 mL/min.

2.2.6 Electrochemical measurements

The electrochemical double layer capacitance (EDLC) of the three electrodes under varying CRs was captured through potentiostatic electrochemical impedance spectroscopy. The impedance of the flow cell in absence of faradaic reactions (i.e. under blocking conditions) was used to determine the EDLC [37]. Experiments were conducted in the single-cell setup described in the previous section with both positive and negative sides containing 2 mol/L H_2SO_4 solutions (diluted from 98% H_2SO_4, Sigma-Aldrich). Volumetric flow rates were maintained at 30 mL/min for all EDLC measurements. The measured data was recorded using an amplitude of 10 mV under the frequency range from 200 kHz to 1 Hz with 12 points per frequency decade.

In addition, full-cell EIS and polarization curves were obtained in the same single-cell setup while circulating the vanadium electrolytes described above. The electrolytes were first charged to 50% state-of-charge (SoC) for both measurements. During full-cell EIS measurements, we adopted the same settings described in EDLC measurements, but the lowest frequency limit was pre-set to 30 mHz to capture the complete mass transport impedance. The measurements were repeated 3 times to check the repeatability and confirm that the cell was at steady state during the measurements (e.g., the electrode pores were fully saturated with electrolytes and that no changes in the state of charge occurred). For the polarization curves, the data was collected every second through linear sweep voltammetry at the scan rate of 5 mV/s from the open circuit voltage (OCV) to a cell voltage of 0.45 V. All electrochemical measurements were carried out using Bio-Logic SP-300 potentiostat.

To compare the electrochemical performance of different electrodes at varying CRs, we selected the same cross-sectional electrolyte velocity (v_e) for all the three electrodes. This was accomplished by use of higher volumetric flow rate (Q) for thicker electrodes or low CRs. v_e was set to 2 cm/s for each test, e.g., a volumetric flow rate of 67.5, 34.4, and 16.9 mL/min was used for felt, cloth, and paper electrodes at 0% CR, respectively. The relationship between v_e and Q under all CRs was shown in Table S2.2. The electrolyte velocity was calculated as follows:

$$v_e = \frac{Q}{A_c} \tag{2.3}$$

where Q denotes electrolyte volumetric flow rate;

and A_c denotes cross-sectional area of the electrode.

2.2.7 Equivalent circuit models and EIS fittings

To describe the ongoing electrochemical process and extract individual contributions to the impedance (i.e., ohmic, kinetic, and mass transport impedance) in the flow cell, equivalent circuit models consisting of several basic circuit elements were employed. Due to the complexity of the porous electrode microstructure, a semi-infinite model, developed by Levie [68] and improved by Pezeshki et al. [68], was used to describe a continuous distributed pore network filled with electrolytes. Assuming that the pores were cylindrical with homogeneous pore distributions, this model could be resolved as a transmission-line model [70] and was used here under non-faradaic [70] and faradaic conditions [69][71].

Under blocking conditions, in the absence of faradaic reactions, the surface impedance of the interface between pores and electrolytes was modelled by a constant phase element

(CPE), to reflect double-layer charging. The transmission-line model was placed in series with an inductor (L_0), to model lead inductance, and a resistor (R_0), to model the membrane resistance, in the equivalent circuit. To better capture the contact resistance feature observed at low CRs in the high frequency region, we introduced an additional RQ element (a parallel connection of a resistor and a constant phase element) in series with the other elements of the circuit. The equivalent circuit model was established using the Python package impedance.py [72]. By fitting the experimental EIS data in high frequency region (i.e., $-\mathrm{Im}(Z) < 2\ \Omega\cdot\mathrm{cm}^2$ in the present study), we could calculate the equivalent EDLC from the best fit parameters from complex nonlinear least squares (CNLS) through the equation [73]:

$$EDLC = Q_0^{\frac{1}{\alpha}} \left(\frac{1}{R_s}\right)^{1-\frac{1}{\alpha}} \tag{2.4}$$

where Q_0 denotes admittance of the constant phase element;

R_s denotes series resistances;

and α denotes exponent of the constant phase element.

After obtaining the EDLC, the ECSA was calculated as follows:

$$ECSA = \frac{EDLC}{C_s m_e} \tag{2.5}$$

where C_s denotes specific capacitance;

and m_e denotes weight of the measured electrode.

In the present study, we adopted the specific capacitance of the glassy carbon electrode reported in Ref. [37], 18 μF/cm^2. We note that there could be a difference of the C_s between the glassy carbon and carbon-fiber electrodes. The obtained results were used to estimate the ECSA for comparison of different electrodes under varying CRs.

Under non-blocking conditions the surface impedance was modeled using a Randles circuit incorporating a finite-length Warburg element to capture the pore-scale diffusion. Details about the establishment of the model can be found in Ref. [69]. The non-blocking transmission-line model was in series with an inductor and a resistor in the equivalent circuit model used here. It should be noted that this model used for full-cell EIS fitting was simplified. The complete electrochemical process in the full-cell VRFB system incorporates two independent kinetic resistances from anode and cathode. In the present study, we assumed that the kinetic resistance from the anode (V^{2+}/V^{3+}) was the major contributor [57] and only considered a single charge transfer process for the cell. This simplified equivalent circuit model contained a single transmission line to model both electrodes but could still capture the electrochemical processes well, resulting in adequate quality CNLS fits to the experimental EIS data.

2.3 Results and discussions

In this section, the morphological and electrochemical results of the three different electrodes under compression are presented. Firstly, the microstructure images and physical properties captured through X-ray μ-CT and SEM techniques are shown in Section 2.3.1 and 3.2. The microstructure changes (e.g., fiber density, porosity, and tortuosity, etc.) under varying CRs (i.e., 10%-50%) are analyzed. Secondly, the mechanical strength and hydraulic properties are presented through strain-stress curves and pressure drop measurements, respectively, in Section 2.3.3 and 2.3.4. Then, the electrochemical properties are presented under both non-faradaic and faradaic processes in Section 2.3.5 and 2.3.6, respectively, to unveil the relationship between the electrode performance and microstructure properties under varying compressions. The trade-off between the electrochemical performance enhancement and pressure drop sacrifice under varying electrolyte velocities are evaluated in Section 2.3.7 and 2.3.8. Lastly, the long-term cycling tests and overall efficiencies under best-performed CR (i.e., CR with highest peak power density in polarization curves) for each type of electrode in a full-cell VRFB are compared in Section 2.3.9.

2.3.1 Uncompressed electrode morphology

Fig. 2.2 shows the through-plane (*z* direction, a1-a3) and cross-sectional in-plane (*x* and *y* direction, b1-b3) microstructure images of the uncompressed felt, cloth, and paper through SEM techniques. Other magnification images are shown in the *Supplementary Information* (Fig. S2.1). The felt electrode (SGL 2.5 EA) is formed by interconnected, relatively sparse carbon fibers, which are produced through carbonization and graphitization of rayon-based polymers. The average fiber diameter is ~6.4 µm (determined using SEM images). Freudenberg H23 paper electrode is a binder free electrode that consists of long carbon fibers, and it is produced through a hydroentangling process without binders. The average fiber diameter is relatively large, i.e., ~10.7 µm (measured from SEM images), compared to the felt electrode. Generally, one of the advantages of large fiber diameters is that it leads to formation of larger pores and in turn improved hydraulic performance. Longer and thicker fibers also help maintain mechanical integrity.

Different from the other two electrodes, the woven cloth electrode (AvCarb 1186, 2×2 basket weave) has periodically repeating features. It consists of multiple single-layer, carbon fiber bundles, and the weave periodicity is 4 cm^{-1}. In addition to the internal small pores (e.g., ~10 µm, measured from SEM images) between the individual fibers inside bundles, the intersections between bundles create relatively large pores (e.g., ~300 µm, measured from SEM images) from the through-plane perspective, which are not fully visible at the magnification used in Fig. 2.1. The complete woven pattern is illustrated in Fig. S2.1. There are also some gaps between warp and fill tows from a cross-sectional perspective. The large pores and gaps are expected to facilitate the electrolyte penetration and reduce the pressure drop but will inevitably be suppressed and deformed under compression. Compared to the paper and felt electrodes after thermal treatment, the fiber surface of the AvCarb 1186 cloth tends to be less smooth with deep grooves, notches, and microscopic pores on the surfaces (see Fig. S2.1). These surface defects could also be observed in the as-received cloth samples before thermal treatment.

From the volume renderings (c1-c3) and through-plane slices (d1-d3) of the X-ray µ-CT raw data in Fig. 2.2, we found that the fiber density is highly uniform for uncompressed felt and paper materials. The fiber density of the cloth electrode is significantly more non-uniform. The 3D data was segmented and processed using the software Avizo to obtain key microstructure properties, which are summarized in Table 2.1.

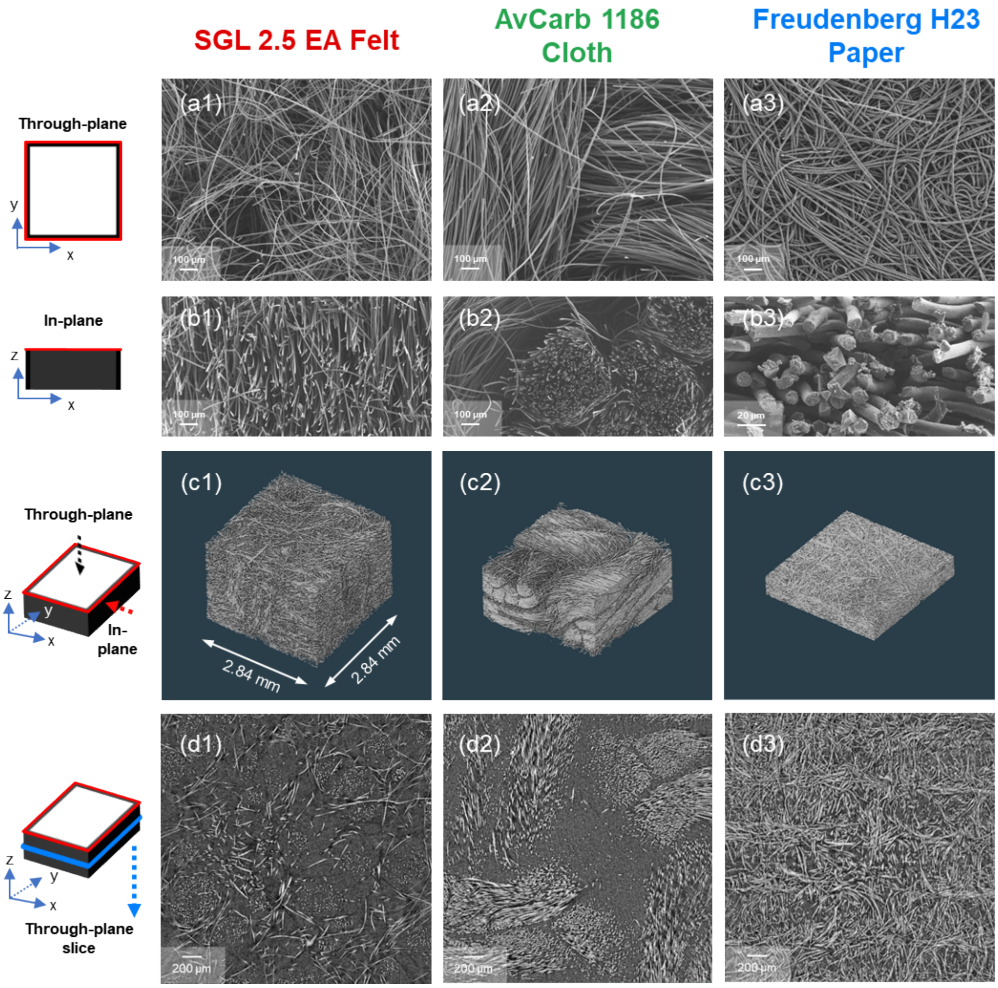

Figure 2.2 Through-plane SEM (a1-a3), in-plane SEM (b1-b3), volume renderings of the X-ray μ-CT data (c1-c3), and through-plane slices from X-ray μ-CT raw data (d1-d3) for the uncompressed felt, cloth, and paper electrodes selected in the present study. The SEM images were captured with the feature size of 100 μm (except for the in-plane image of the paper). Because the paper is much thinner than the other samples, three layers of papers were stacked for the X-ray μ-CT scan.

First, for the porosity results shown in Table 2.1, the felt displays the highest porosity (89.7%, measured form X-ray μ-CT), while the paper shows a relatively dense structure (72.4% porosity, measured form X-ray μ-CT), in agreement with the features shown in Fig. 2.2. The porosity obtained from the 3D reconstructions of the three uncompressed electrodes are all consistent with the data provided by the manufacturers. We note that the employed spatial resolution (pixel size=4.12 μm) leads to some exaggeration of the fiber-to-fiber contacts observed in the X-ray μ-CT 3D data, which reduces the apparent porosity. Analysis of an additional X-ray μ-CT data set recorded at higher spatial resolution (pixel size=1.68 μm) yielded fewer voxels with fiber-to-fiber contact for the uncompressed felt electrodes and the porosity determined from the X-ray μ-CT is 95 % (see Fig. S2.6 in *Supplementary Information*) in this case. This is because the higher resolution makes it possible to resolve small spaces between fibers which are not resolved at lower spatial resolution. In practice, this means that the accuracy of the measured porosity depends to some degree on the spatial resolution used to image the electrode. Similar results are also found in a related literature report [51]. However, higher spatial resolution requires longer scanning time, which would not be feasible to use for the full compression series. More importantly, the samples (especially for the cloth) are not homogeneous at the micrometer scale, we would get very different results depending on where we choose the scan region at such a high resolution. Hence, our choice of the resolution is a compromise between getting sufficient resolution to be able to resolve the individual fibers, and at the same time maximize the field of view to avoid too large influence from local non-uniformities. In the present study, we put the emphasis on the microstructure property changes under varying CRs (as shown in Section 2.3.2) for each selected electrode. The effects of the resolution selection on the measured results are beyond the scope of the present study.

Secondly, we measure the specific surface areas from X-ray μ-CT data, and compare with the BET measured, ECSA measured (see Section 2.3.5), and theoretically predicted results. Generally, the X-ray μ-CT specific surface area is of the same order of magnitude as the results predicted from the (smooth) cylindrical filament model, and both are smaller than measured BET and ECSA results. The X-ray μ-CT measured results at higher resolution (e.g., 0.51 m^2/g for uncompressed felt shown in Table S2.3) are slightly increased and closer to the model-predicted results (e.g., 0.77 m^2/g), but still different from the results measured through BET and ECSA. This discrepancy is mainly attributed to the rough surface characteristics (microscopic pores and grooves as shown in Fig. S2.1) of individual carbon fibers. The cylindrical filament model assumes non-overlapping fibers with absolute smooth fiber surface [37]. And the spatial resolution of the X-ray μ-CT is not sufficient for resolving these surface microstructures. Neglecting the surface roughness is inherent in X-ray μ-CT and in the smooth cylindrical filament model and will underestimate the specific surface areas from sub-micron and nano-scale pores. However, we expect that the compression effects do not have noticeable impacts on the surface microstructures of individual fiber. The trends in the surface area change measured through X-ray μ-CT under varying CR (in Section 2.3.2) are still effective to present the inter-fiber microstructures and states under compression, which is more critical to the scope of the present study. Moreover, it is noted that there is an especially large discrepancy between surface areas measured from X-ray μ-CT and BET for the Freudenberg H23 paper. The surface area of the paper before thermal treatment measured from BET (i.e., 0.37 m^2/g, as shown in Table S2.1) is two orders of magnitude smaller than the result after thermal treatment in Table 2.1 (i.e., 53.63 m^2/g), indicating that the selected temperature and duration have great impact on the surface microstructures of this paper. For the cloth and paper, we don't see such a great increase after thermal treatments for the BET surface areas, which may be due to the different carbonization or graphitization degrees during manufacturing process. Similar surface area increments of the Freudenberg H23 paper after thermal treatment are also found in other study [17][18], where they point out that the majority of the added surface area comes from the sub-nanometer (<1 nm) pore size range [17]. These pores cannot be identified through X-ray μ-CT and not even from our SEM images, which may need advanced nano-CT instrument for recognition.

Tortuosity is a crucial metric to describe effective transport pathways within the porous structure compared to ideal straight transport pathways [70]. In the present study, we used an open-source MATLAB application, TauFactor (version 1.4) [52], to calculate the tortuosity for the three electrodes from x, y, and z directions based on the segmented X-ray μ-CT 3D image data. Generally, we find that for the uncompressed electrodes, the felt shows the lowest and most isotropic tortuosity in all the three directions, likely due to its high porosity. The paper and cloth electrodes show more tortuous structures, and the through-plane (i.e., z direction) tortuosity results are higher in both cases than observed the in-plane (i.e., x and y directions) tortuosity. This is in agreement with literature [52].

Similarly, due to the selection of the pixel size in the present study and the fiber-to-fiber contact phenomenon, the tortuosity may be slightly overestimated. Selected tortuosity results obtained under higher resolution are listed in Table S2.3.

Table 2.1 Microstructure parameters for uncompressed carbon-based electrodes

Electrode commercial name		SIGRACELL felt GFD 2.5 EA	AvCarb carbon cloth 1186 HCB	Freudenberg H23
Original thickness* (mm)		2.5	1.27	0.21
Weave periodicity* (cm^{-1})		-	4	-
Average weight* (g/m^2)		250	525	95
Measured weight (g/m^2)		209±4	519±6	91±6
Uncompressed porosity (%)		94*	82 [38]	80*
Measured porosity# (%)		90 (+2/-4)	82 (+2/-3)	72 (+3/-5)
Average fiber diameter## (μm)		6.4±0.2	9.9±0.3	10.7±0.2
X-ray μ-CT surface area# (m^2/g)		0.13	0.08	0.10
Model-based surface area (m^2/g)		0.77	0.18	0.24
BET surface area (m^2/g)		7.52	0.61	53.63
ECSA (m^2/g)		1.42	0.32	21.19
Tortuosity#	x	1.27	1.49	1.52
	y	1.22	1.56	1.57
	z	1.26	1.98	2.14

* Provided by the manufacture datasheet.

\# Calculated through the 3D segmented data from X-ray μ-CT with pixel size of 4.12 μm.

\## Measured from multiple SEM images (N⩾6).

2.3.2 Microstructure properties under compression

The electrode microstructure will be inevitably suppressed and deformed under compression during practical battery operation, which has impacts on electrochemical process (contact resistance, mass transport process, etc.). To better understand the relationship between electrode morphology and electrochemical performance for each type of electrode, we select some critical microstructure parameters (i.e., porosity, volumetric specific surface area, and tortuosity) and measure them under 0-50% CRs in X-ray μ-CT using the custom-built compression tool. The maximum obtainable CR for Freudenberg H23 paper (3 layers) in our compression tool was 30%.

Fig. 2.3 shows orthoslices of pore size distribution images from the through-plane direction for each electrode at 0% and maximum compression (i.e., 50% CR for felt and cloth, and 30% CR for paper). The pore sizes were determined using a local thickness map method in Avizo from the segmented 3D data. The mean pore diameters presented in Fig. 2.3 are determined based on the complete 3D reconstructions. The detailed pore size distribution histograms before and after compression are shown in Fig. S2.7. From Fig. 2.3, we find that compression drastically reduces the pore size within the porous electrodes. For the felt, the mean pore diameter is reduced by 52.2% from 47.9 μm (uncompressed) to 22.9 μm (at 50% CR), but the overall reduction of the pores is relatively uniform under compression. As for the cloth, the pore compression mainly occurs at the intersections between fiber bundles, which are regarded as the electrolyte rapid penetration pathways for cloth electrodes. At extremely high CR of 50%, the large channels in the cloth are deformed and compressed significantly, indicating that the related mass transport advantages will be significantly reduced, which will result in highly elevated pressure drop, which is not desirable in practical application. The mean pore diameter of the cloth electrode decreases under compression to a larger extent than for the felt electrode, from 63.1 μm to 19.4 μm. In addition, we also observed that the fibers within the fiber-bundles in the cloth are already in close contact in the uncompressed cloth. The warp and fill tow bundles are significantly distorted at 50% CR, resulting in high tortuosity results as shown in Fig. 2.5. For the paper electrode there is no obvious mean pore diameter reduction due to its high compactness and uniform pore features. We still observe a decrease of the overall porosity after compression for this electrode.

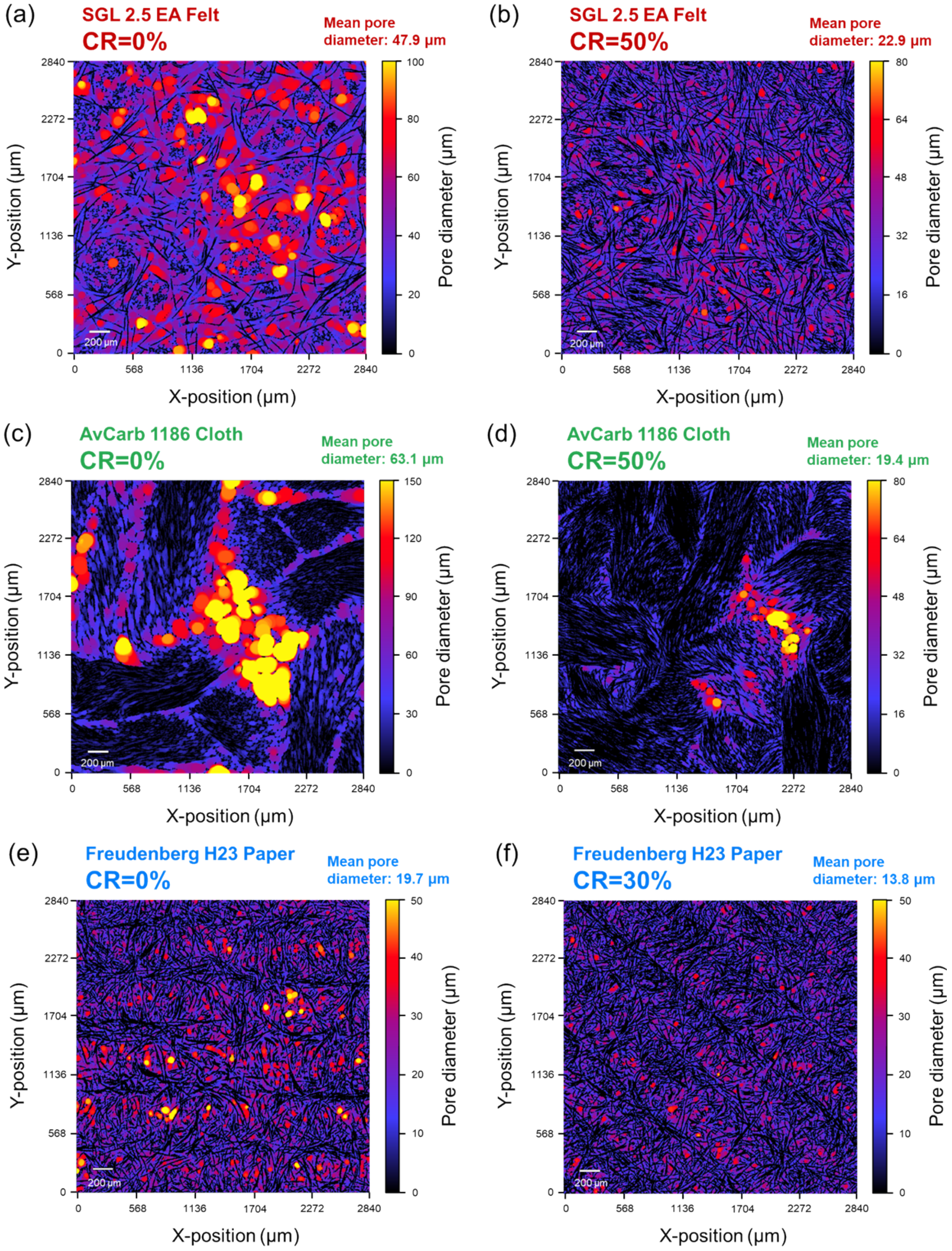

Figure 2.3 Example through-plane orthoslices of pore size distribution images for the felt at (a) 0% CR and (b) 50% CR, cloth at (c) 0% CR and (d) 50% CR, and paper at (e) 0% CR and (f) 30% CR.

The porosity (ε) and volumetric specific surface area (α_V) obtained from the segmented 3D data under the complete CR range are shown in Fig. 2.4. The light-colored regions represent the error bars (see Section 2.2.3). For the porosity analysis, Eq. (2.6) is commonly used in porous materials to estimate the porosity as a function of the compression assuming that there is a constant solid volume during uniform compression [53]. The predicted porosity changes under compression (dashed lines) based on the measured uncompressed porosity data in Fig. 2.4(a) were added to facilitate comparison with the observed X-ray μ-CT trends.

$$\varepsilon_c = 1 - \frac{L_0}{L_c}(1-\varepsilon) \tag{2.6}$$

where all the parameters are defined above.

In Fig. 2.4(a), we find that the porosity decreases with CR increments, and the X-ray μ-CT measured porosity shows good agreement with the predicted results for all three electrodes. The decreased porosity during compression may help to increase inter-fiber contacts within the electrodes and increase the effective electrical conductivity. To verify this, we show the volumetric specific surface area results (determined through the fiber surface area divided by the sample volume) under compression in Fig. 2.4(b). If there are no additional fiber contacts during compression, the fiber surface area should remain constant while the sample volume should decrease due to the compressed thickness, resulting in increased α_V with increasing compression. We observed this expected trend for the felt sample, which indicates that before 50% CR there is no significant influence of apparent fiber contacts and the electrode still remains highly porous. However, for the cloth at high CRs (i.e., 30-50%) and paper, α_V does not increase or even decreases with CR increments. This means that surface area is lost by formation of fiber-to-fiber contacts. It should be noted that although more fiber contacts under compression help to increase inter-fiber electrical conductivity, they do not contribute to the ohmic resistance reduction if there is an extremely high degree of tortuosity. In addition, both decreased porosity and increased tortuosity at high CRs will both lead to increased pressure drop (see Fig. 2.7), which is not favorable in battery operation.

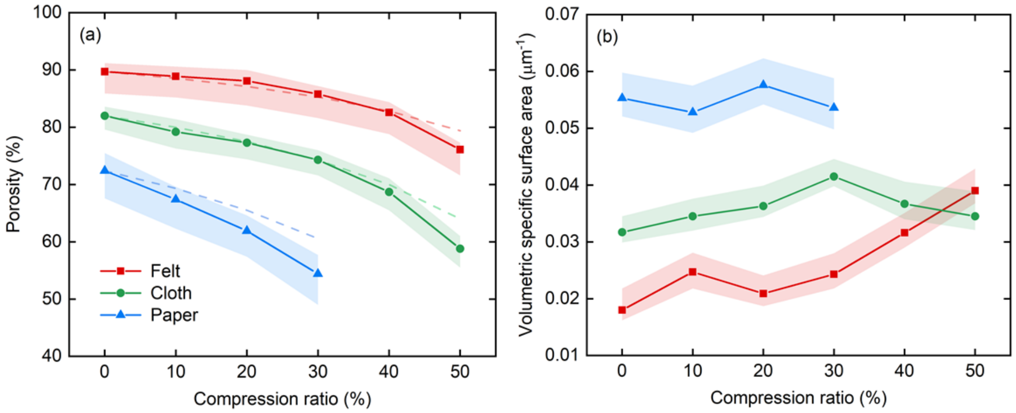

Figure 2.4 Variations of the (a) porosity and (b) volumetric specific surface area of the felt, cloth, and paper electrodes under varying CRs calculated from X-ray μ-CT segmented 3D data. Light colored areas represent error bars, where the upper and lower limits were determined by manual adjustment of the global threshold until the segmentation became clearly unreasonable as evaluated from slice images. The dashed lines in (a) represent the predicted porosity under compression.

To better understand the fiber features under compression, the tortuosity results under varying CRs calculated from segmented 3D data using TauFactor for the three electrodes are shown in Fig. 2.5. We select the average tortuosity from *x* and *y* direction to represent the in-plane tortuosity as shown in Fig. 2.5(a), and the *z* direction results as the through-plane tortuosity as shown in Fig. 2.5(b). Electrode tortuosity is highly correlated to the electrolyte flow pathways within the porous microstructure. High tortuosity may lead to stagnant flow regions and elevated concentration overpotentials in the flow battery. In the present study under FT-FF designs, the in-plane tortuosity is expected to have the largest impact on the flow resistance. But for the flow-by flow patterns (e.g., serpentine flow field), the through-plane tortuosity may also play a significant role as the electrolyte needs to penetrate from the flow fields to the regions near the membrane. From Fig. 2.5, we could find that the tortuosity increases with applied compression, and the through-plane tortuosity results for the three electrodes are generally higher than in-plane results. This is probably because the fibers in the *z*-direction tend to be bent and twisted under through-plane compression. Similar trends were also observed in other work [51]. For the cloth, we found that there are rapid through-plane tortuosity increases at high CRs. This probably comes from the excessive fiber contacts and kinks within the bundle regions, which can be found from Fig. 2.3(d). For the paper electrode, we found that the in-plane tortuosity grows markedly with CR increments while the rise of the through-plane tortuosity is not obvious. We speculate that there could be more fibers oriented along the in-plane direction than in the through-plane direction.

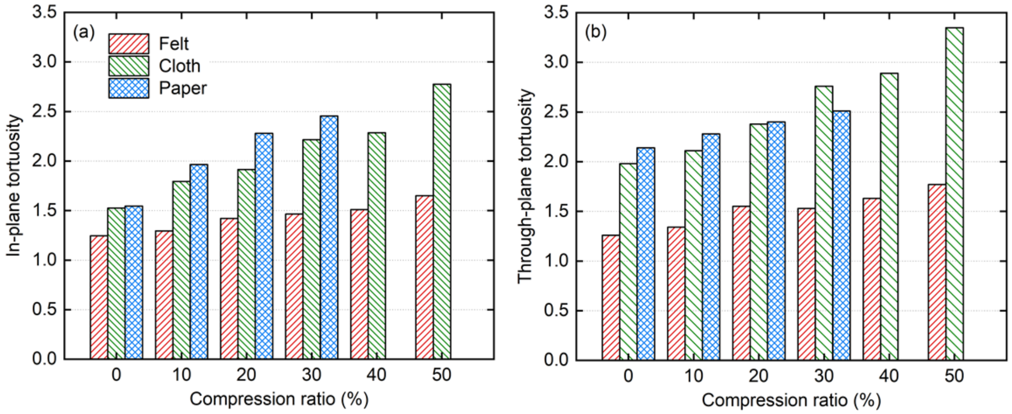

Figure 2.5 (a) In-plane and (b) through-plane tortuosity results of the felt, cloth, and paper electrodes under varying CRs calculated from X-ray μ-CT segmented 3D data. The in-plane tortuosity results are calculated through the average of the results from *x* and *y* directions.

2.3.3 Mechanical strain-stress curves

The strain-stress curves of the three electrodes are shown in Fig. 2.6, which can be regarded as a measure of the mechanical behavior of the electrodes. The observed response reflects the external force required in battery compression as a function of the compression. We found that there are two typical regions in the curves for all three electrodes. The compression stresses initially increase slowly in the first region, and then a rapid non-linear increase at high CR ranges. It is implied that under low CR ranges, the air is expelled from the internal electrode and the pores are compressed. When the large pores are mostly collapsed and fiber-to-fiber spacings are narrowed to the point where they are tightly connected, the strain-stress curves are likely to reflect the rigidity of the carbon fibers themselves. This is supported by the observed surface area variations under compression in Fig. 2.4(b).

In Fig. 2.6, the felt displays a relatively slow buildup of stress under compression among the three electrodes. The stress remains low (<0.06 MPa) when the CR is below ~40%, and only slightly increases at the CR range of ~40% to 60%, reaching 0.18 MPa at 60% CR. The high porosity of the felt electrode leaves ample space for the internal pores to be compressed. For the cloth, the stress responds quickly compared to the felt. The compression stress elastically increases at the beginning, and rises up fast when above ~30% CR. Under compression, the large pores at the intersections between fiber bundles are expected to be deformed first until these large pores have almost collapsed. At this point, the advantages of the large pores for electrolyte penetration are significantly reduced, leading to substantially increased pressure drops (see Fig. 2.7(b)). As for the paper, the elastic stress region is only at CR below ~8%. The compression stress grows rapidly with further compression and reaches 1 MPa already at 22% CR, which is good agreement with the data provided by manufacturer (1 MPa compression pressure at 19% CR). Hence, ~20% CR can be regarded as the maximum value for this paper in a flow cell as additional compression requires great load forces. However, up to 40% CR could be achieved in practical flow battery assembly under a torque of 8 N·m without electrolyte leakage. This could in part be due to the compression of other non-rigid components inside battery, such as membrane and even PTFE gaskets under such a high mechanical load. Under extremely high CR ranges (~40-50%), the electrode fibers may penetrate through and destroy the membrane, resulting in severe crossover of active species and short circuiting, which should be avoided.

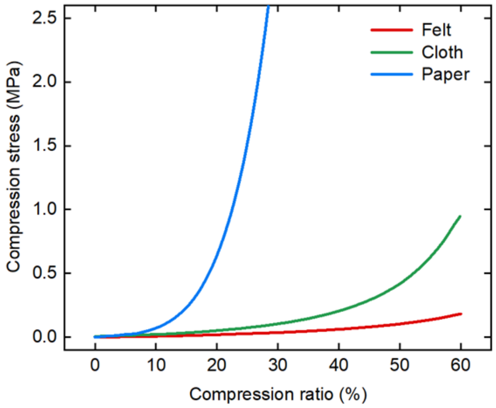

Figure 2.6 Strain-stress curves of the felt (red), cloth (green), and paper (blue) electrodes under the through-plane CRs of 0-60%.

2.3.4 Pressure drop and permeability

Electrode permeability (κ) is a crucial factor for fluid dynamic performance. High electrode permeability effectively reduces the pump energy consumption during battery operation and improves the system efficiency. In the present study, we employed the non-linear Darcy-Forchheimer equation [37] to capture the deviations from the linear Darcy equation at high electrolyte velocities due to unidirectional flow and internal microscopic effects. The equation is expressed as follows:

$$\Delta P = \frac{\mu Q w_e}{\kappa A_c} + \beta \rho (\frac{Q}{A_c})^2 w_e \tag{2.7}$$

where ΔP denotes measured pressure drop of the electrode;

μ denotes electrolyte viscosity (=4.928 mPa·s in the present study [74]);

w_e denotes width of the electrode through which the electrolyte passes;

β denotes non-linear Forchheimer coefficient;

ρ denotes electrolyte density (=1.354 g/cm^3 in the present study [74]).

and the other parameters are defined above.

Fig. 2.7 shows the measured pressure drop vs. volumetric flow rate under varying CRs for the three electrodes in a FT-FF single-cell setup. We found that CR has great impact on the electrode pressure drop. For all the three electrodes, the pressure drop is elevated at higher CRs as the compressed pores and the resulting increased tortuosity amplifies the flow resistance through the electrodes. In the volumetric flow rate range (0-25 mL/min) measured in the present study, the pressure drop curves show a nearly linear variation with increasing flow rates. The non-linear Forchheimer coefficient (β) becomes significant only at higher CRs, e.g., 9.0×10^{5} m^{-1} and 2.9×10^{6} m^{-1} for the cloth at 40% CR and paper at 30% CR, respectively. The details of the κ and β results under varying CRs could be found in Table S2.4.

The permeabilities obtained from the measured pressure drops are summarized in Fig. 2.7(d). Due to the highly porous character of the felt electrode, the permeability remains high even at higher CRs. Specifically, the measured permeability gradually decreases from 1.8×10^{-10} m^{2} at 0% CR to 6.8×10^{-11} m^{2} at 50% CR. In contrast, the cloth electrode demonstrates desirable high permeability at low CR (0-20%), but deteriorates rapidly from 20% to 40% CR. This implies that the electrolyte channels at the intersection of fiber bundles are excessively deformed, eliminating the hydraulic advantages of this woven structure. As for the paper electrodes, the measured permeability at 0-30% CR is consistently the lowest among the three electrodes. In the uncompressed condition, at 0% CR, the permeability of the paper electrode is 6.7×10^{-11} m^{2}, which is less than a third than that of the cloth. The measured permeability results are compared to the other studies at certain CR, and the results are in good agreement with previous studies in most cases. For instance, Forner-Cuenca et al. [37] reported a permeability of 2.0×10^{-11} m^{2} for untreated Freudenberg H23 paper at the CR of 23±9%, and Andrew et al. [39] reported ~5×10^{-11} m^{2} through-plane permeability for plasma-activated AvCarb 1186 cloth at 40% CR. The discrepancies may be due to the different electrode pretreatment approaches and different electrolyte solvents. It is noted that for the felt electrodes, we observed different permeability results with FT-FF designs from other literatures, e.g., 2.7×10^{-11} m^{2} at 12±6% CR [37], or 1×10^{-9} m^{2} at 28% CR [61]. This might be attributed to the different original thickness of the felt samples and different manufacturers, which may need further exploration.

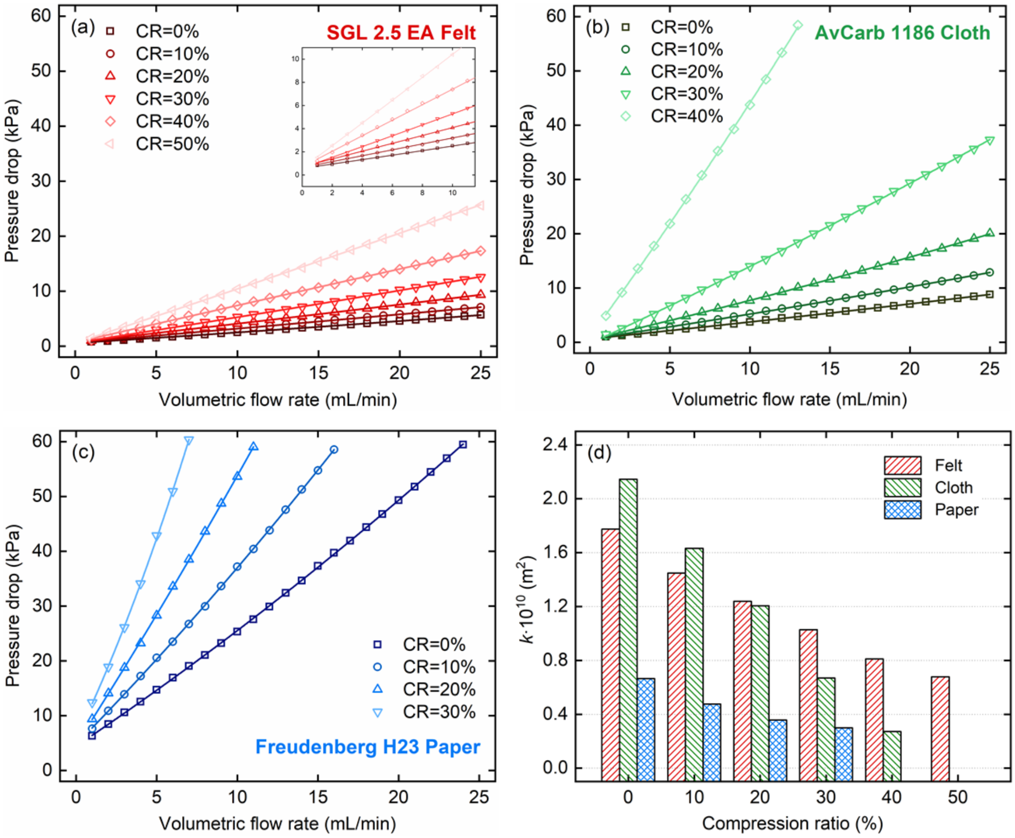

Figure 2.7 Pressure drops (dots) versus volumetric flow rates within the single-cell (FT-FF flow patterns) under varying CRs for the three electrodes: (a) felt, (b) cloth, and (c) paper. The volumetric flow rates are within the range of 0-25 mL/min. The solid lines show the results of non-linear least squares fits of the Darcy-Forchheimer equation to the experimental data. Due to the limitation of the pressure sensors, the measurements of the cloth under 50% CR and the paper under 40% and 50% CRs are not presented; (d) calculated permeability from the fittings under varying CRs for the three electrodes.

2.3.5 EIS under non-faradaic condition

In previous sections, we investigated the electrode surface areas through X-ray μ-CT under varying CRs, and also through BET, and cylindrical filament model (uncompressed conditions) for the three electrodes. However, ECSA results may be different to physical surface area measurements (BET, X-ray μ-CT) in the flooded electrode as there may be nano-scale porosity after the thermal treatment where the active species in electrolytes cannot get access to. This is also influenced by the electrode wettability, the hydrodynamic radius of the active species, and solvent properties. Other literature reported discrepancies between physical (e.g., from BET) and electrochemical surface area results [37]. To evaluate the ECSA of the three electrodes and the impact of electrode microstructure on battery performance under compression, the EIS measurements were conducted under non-faradaic (blocking) conditions in 2 mol/L H_2SO_4 aqueous electrolyte to estimate the double layer capacitance and ECSA. The EIS results and equivalent circuit model fits are shown in Fig. 2.8. We used the measured weight of the electrodes (as shown in Table 2.1) for normalization of the ECSA calculations, and the results are summarized in Table 2.2.

From Table 2.2, we can find that the paper electrodes hold the highest ECSA values. The large ECSA yields low kinetic losses for the paper electrode. The relatively low ECSA of the cloth electrode yields high kinetic losses (see Fig. 2.9). The cloth may require another temperature in the thermal activation process or use of other pre-treatment methods (such as KOH-etched [75], nanoparticle modified [76], etc.) to further improve the active surface area and/or provide a larger number of reaction sites. Under varying CRs, we find that for the felt and cloth, the ECSA does not noticeably change, except a small decrease at high CR, indicating a slight reduction of the number of accessible electrochemical active sites at high compression. Interestingly, we observe an increase of the ESCA for the paper especially at 30% and 40% CRs, but we do not see this increase in X-ray μ-CT results before 30% CR. The accessible fiber surface area should not increase under compression. We speculate that the observed increase in ECSA at high CR may be due to fiber breakage.

The collected non-faradaic EIS data is displayed in a series of Nyquist plots in Fig. 2.8. A semi-circle is present at high frequencies in the data collected at low CR (e.g., 0-10% CR for the felt and paper). This high-frequency feature gradually decreases with increasing CR until it completely disappears at ~30% CR for both felt and paper. We interpret this resistance as a contact resistance, likely derived from poor and/or low numbers of contacts between carbon fibers and flow plates when insufficient external compression force is applied. The contact resistance is most pronounced for the felt electrode, which is the electrode with the highest porosity and thus is expected to have the fewest contact points to the carbon composite flow plates at low compression. The presence of the contact resistance impacts the evaluation of ECSA due to the large overlap with the impedance of the porous electrodes. This problem leads to that the fitted R_{ion} is underestimated in the CNLS fits, and in turn leads to lower ECSA estimates at low CR (e.g., paper at 0% CR). The contact resistance effect is not obvious even under 0% CR for the cloth electrodes. Similar trends could also be observed in full-cell EIS results in Fig. 2.9.

Table 2.2 ECSA (m^2/g) of the felt, cloth, and paper under the range of 0-50% CRs

	SIGRACELL felt GFD 2.5 EA	AvCarb carbon cloth 1186 HCB	Freudenberg H23
CR=0%	1.42	0.32	21.19
CR=10%	1.36	0.31	24.17
CR=20%	1.37	0.30	23.95
CR=30%	1.27	0.33	26.14
CR=40%	1.29	0.32	27.27
CR=50%	0.91	0.29	-

In addition to the ECSA, we can also acquire basic information about through-plane (i.e., along with the electrochemical measurement direction) tortuosity from EIS measurements under non-faradaic conditions [70]. An empirical MacMullin number (N_M) is defined as follows to link the tortuosity and porosity:

$$N_M = \frac{\tau}{\varepsilon} \tag{2.8}$$

where all the parameters are defined above.

The N_M is also defined through conservation laws [70], which is expressed as follows:

$$N_M = \frac{\kappa_s}{\kappa_{eff}} \tag{2.9}$$

where κ_s denotes bulk electrolyte conductivity;
κ_{eff} denotes the effective ionic conductivity (of the flooded porous electrode).

Given that the electronic resistances in electrode solid phase are negligible compared to the ionic resistances, after quantification of the R_{ion} from EIS fittings under blocking conditions, the electrode tortuosity could be defined as follows [70]:

$$\tau = \frac{R_{ion} A \kappa_s \varepsilon}{2L_c} \tag{2.10}$$

where all the parameters are defined above.

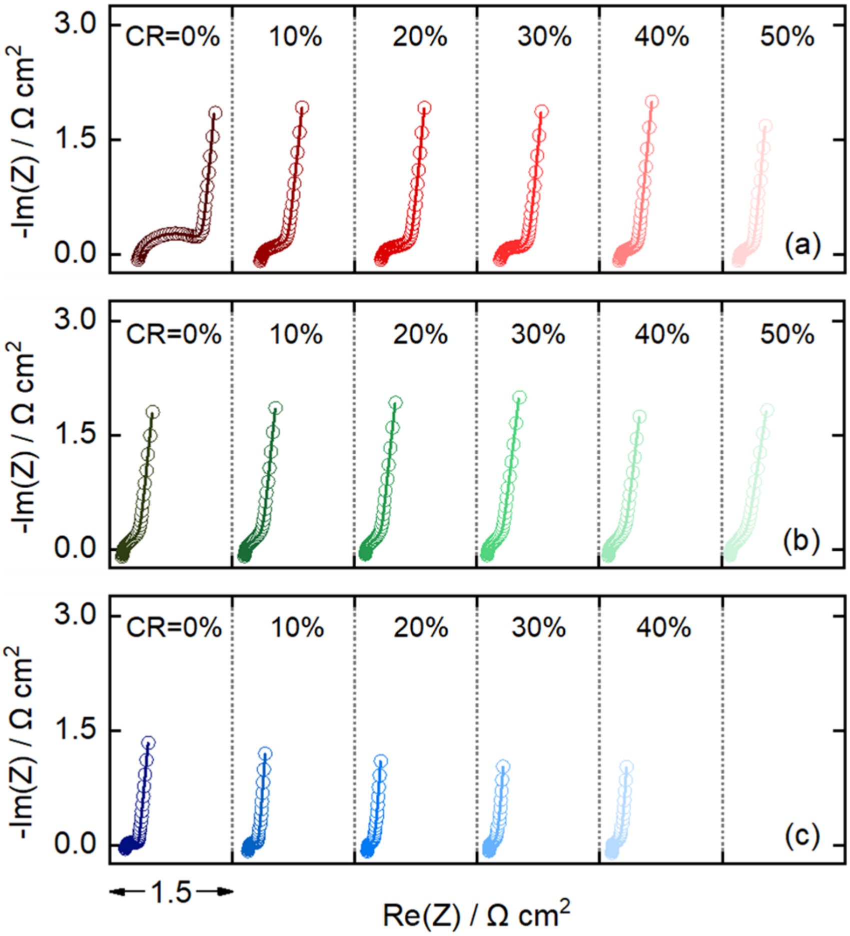

Figure 2.8 Nyquist plots of measured EIS data (open circles) and CNLS fits (lines) for the (a) felt, (b) cloth, and (c) paper electrodes under 0-50% CRs in 2 mol/L H_2SO_4 solutions. The volumetric flow rates are 30 mL/min for all measurements.

The electrochemical through-plane tortuosity provides insights into electrode microstructure features without additional equipment (such as X-ray μ-CT) and major modifications of the battery setup. In the present study, due to the impact from the contact resistance on the R_{ion} results, we only present the tortuosity results obtained at high CRs, where the contact resistances are minimized.

The calculated tortuosity results are shown in Table 2.3. We can find that at high CRs from 30% to 50%, the cloth shows the highest tortuosity, while the felt is the least tortuous. This is in overall agreement with the through-plane tortuosity results measured through X-ray μ-CT in Fig. 2.5(b). The results obtained here are generally lower than the X-ray μ-CT results. The reason could be an overestimation from X-ray μ-CT analysis due to the fiber-to-fiber contact phenomenon from the selected low resolution in the present study as discussed in Section 2.3.1.

Table 2.3 Through-plane tortuosity of the felt, cloth, and paper from EIS at high CRs

	SIGRACELL felt GFD 2.5 EA	AvCarb carbon cloth 1186 HCB	Freudenberg H23
CR=30%	-	1.69	1.48
CR=40%	1.23	2.04	-
CR=50%	1.36	2.10	-

2.3.6 Full-cell electrochemical performance

The full-cell EIS measurements were conducted at 50% SoC at a flow velocity of 2 cm/s for the three electrodes at 0-50% CRs to map out and resolve the electrochemical losses (including ohmic, kinetic, and mass transport resistances) in an VRFB. The EIS results and equivalent circuit fits are presented in Fig. 2.9. Electrolyte leakage occurred at 50% CR for the paper electrodes during battery assembly, so those results are omitted here.

The area-specific ohmic resistance (R_{Ω}) values obtained from CNLS fitting are shown in Fig. 2.10(a). The ohmic resistance of the cell is dominated by the membrane resistance but the electronic conductivity of the carbon electrodes may also contribute significantly. We found that in a series of cells with the same type of membrane but loaded with different types of electrodes, the cell with felt electrodes generally shows the highest ohmic resistances, since the electrode thickness is two and four times that of cloth and paper, respectively. In addition, all three electrodes display a decreasing ohmic resistance with increasing CR at moderate compression ratios (e.g., 0-40% CR for felt and cloth, and 0-30% for paper). The decreased R_{Ω} is attributed to an increasing number of contact points between the fibrous electrodes and the flow plates. There is no further decrease of R_{Ω} at high CRs. However, the R_{Ω} increases again at 40-50% CRs for felt and cloth, and at 30-40% CRs for paper as shown in Fig. 2.10(a). In this region, there are sufficient contacts between fibers and plates, and the compressed pores and greatly enhanced tortuosity become significant. This trend is in good agreement with findings in previous studies [53][65]. The R_{Ω} of the cloth changes significantly less with CR variations than it does for the felt and paper electrodes, suggesting that the number of effective contact points may not change much under varying CRs.

In addition to the R_{Ω}, we observe a contact resistance arc at low CRs (e.g., CR=0% for the felt, and 0-10% CRs for the paper) in the EIS data, which is similar to the EIS results under non-faradaic conditions in Fig. 2.8. When the contact resistances are insignificant, at high CR, the kinetic resistance barely changes with varying CR for all the electrodes, except for a slight increase at 50% CR for felt and cloth, which is consistent with the ECSA trend observed under non-faradaic conditions. The paper electrodes with the highest ECSA exhibit the lowest kinetic resistances under moderate compression. The volumetric specific surface area of the electrodes (as shown in Fig. 2.4) obtained from X-ray μCT data is larger for the cloth than the felt, but this technique is not able to capture roughness or porosity with dimensions smaller than the pixel/voxel size. Normalizing the ECSA to the electrode volume indicates that the felt has a greater surface area per volume. The observed trends in the kinetic resistance and in the volumetric specific surface area may reflect poor utilization of finer porosity in the thermally treated felt electrode.

The mass transport resistance (R_{MT}) is also expected to be greatly affected under compression. The R_{MT} results are extracted from Fig. 2.9 and summarized in Fig. 2.10(b). In general, the R_{MT} decreases first and then increases with CR increments for the three electrodes. It indicates that moderate pore compression can facilitate increased electrolyte flow velocity inside the pores, but excessive compression leads to increased resistance to electrolyte flow. Compression has strong impact on R_{MT} of the paper electrodes. As shown in Fig. 2.10(b), the R_{MT} of the paper electrodes first decreases from 0 to 10% CR, and then increases by ~two times from 10% to 40% CR. The R_{MT} results here are generally small, especially for the paper electrodes considering their dense microstructure and low permeability features. This is a result of the relatively high electrolyte flow velocity (2 cm/s) used here. The impact of electrolyte flow rate on mass transport is discussed in the following (as shown in Fig. 2.12).

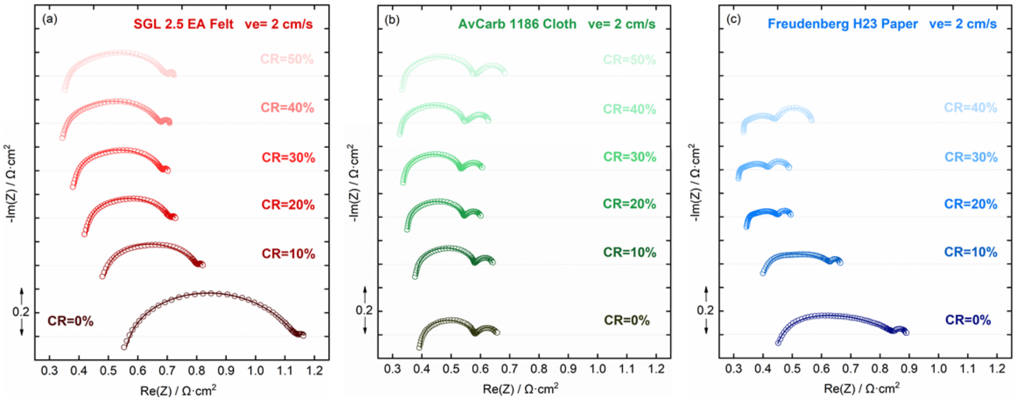

Figure 2.9 Nyquist plots of measured EIS data (open circles) and CNLS fits (lines) for the (a) felt, (b) cloth, and (c) paper electrodes under 0-50% CRs in a full-cell VRFB setup. The electrolytes for positive and negative sides are pre-charged and maintained at 50% SoC. The flow velocities are 2 cm/s for all measurements.

The polarization curves of the three electrodes under varying CRs are shown in Fig. 2.11, which display an overall agreement with the results obtained from EIS above. We found that with increasing applied compression, the overall electrochemical performance of the three electrodes improves at low CRs, then deteriorates rapidly at high CR ranges. Compared to the felt and paper, compression has less impact on the electrochemical performance of the cloth (except at CR=50%) and the polarization curves are quite similar from 0-40% CR. This may be attributed to the modest change in the R_{Ω} of the cells with cloth electrodes as shown in Fig. 2.10(a). Such robust features are favorable in industrial flow battery reactor designs [77]. In addition, as the applied compression increases, all three electrodes exhibit a mass transfer-limited current that decreases with increasing CR,. Such high current densities are usually not used in practical applications. At current densities below the limiting current, moderate compression is still an effective way to reduce the ohmic and mass transport.

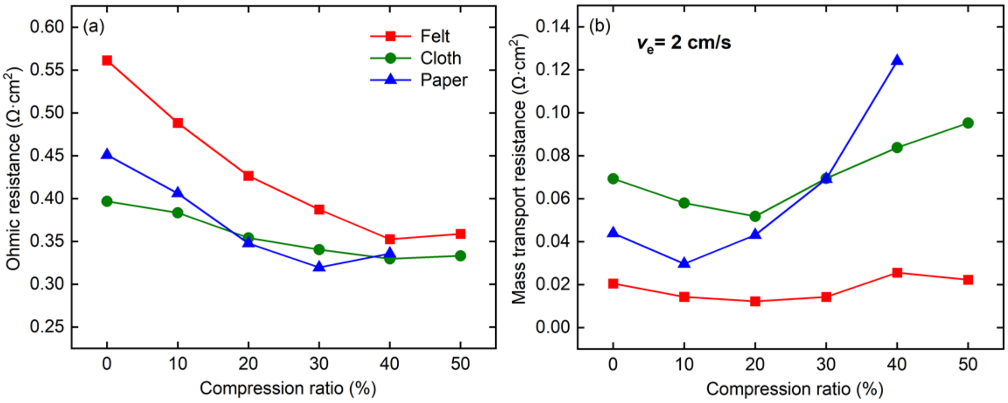

Figure 2.10 (a) Variations of ohmic resistances and (b) mass transport resistances with respect to CR for the three electrodes at 50% SoC under v_e=2 cm/s.

Discharge current-voltage and power-density curves for each CR for the different cells is shown in Fig. 2.11(a-c) , and a summary of the peak power density results is displayed in Fig. 2.11(d). At 0% CR, the cloth shows the highest peak power density among the three electrodes, and then surpassed by the paper electrodes at 10-30% CRs. Under extreme compression (i.e., at 50% CR), only the highly porous felt electrodes could retain performance (>600 mW/cm^2). We selected the CR at which each of the three electrodes reach their highest peak power densities, that is, 20% CR for paper and cloth electrodes, and 30% CR for felt electrode, as the optimum CRs and adopt these in the following analysis designed to investigate the mass transport properties (Section 2.3.7) and overall cycling performance (Section 2.3.9).

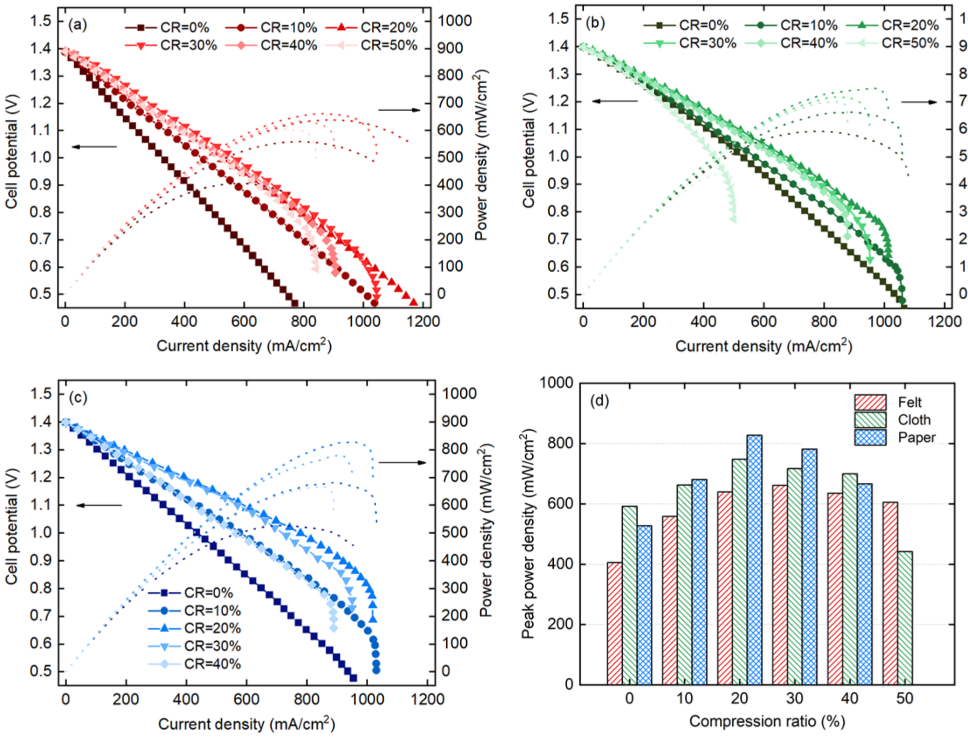

Figure 2.11 Polarization (dots) and power density (dashed lines) curves under varying CRs for the (a) felt, (b) cloth, and (c) paper electrodes; (d) extracted peak power density results under varying CRs for the three electrodes. The tests are measured under 50% SoC in a full-cell VRFB. The flow velocities are selected as 2 cm/s for all measurements.

2.3.7 Mass transport properties under varying electrolyte velocities

The electrochemical measurements above are carried out at a constant high electrolyte velocity, v_e=2 cm/s. To unveil the significance of the electrolyte velocity on the mass transport properties, we further measure the polarization curves at optimum compression for each electrode using electrolyte velocities of 0.5, 1, 2, and 5 cm/s. The resulting polarization curves are displayed in Fig. 2.12. The curves are iR-corrected to remove impacts from ohmic resistances. Emphasis is placed on the mass transport resistances given that the electrolyte velocity is not expected to have a significant effect on ohmic and kinetic resistances. Moreover, full-cell EIS measurements were also conducted to extract the R_{MT}

in each case as shown in Fig. 2.12(d). The complete set of EIS data is available in *Supplementary Information* (as shown in Fig. S2.8).

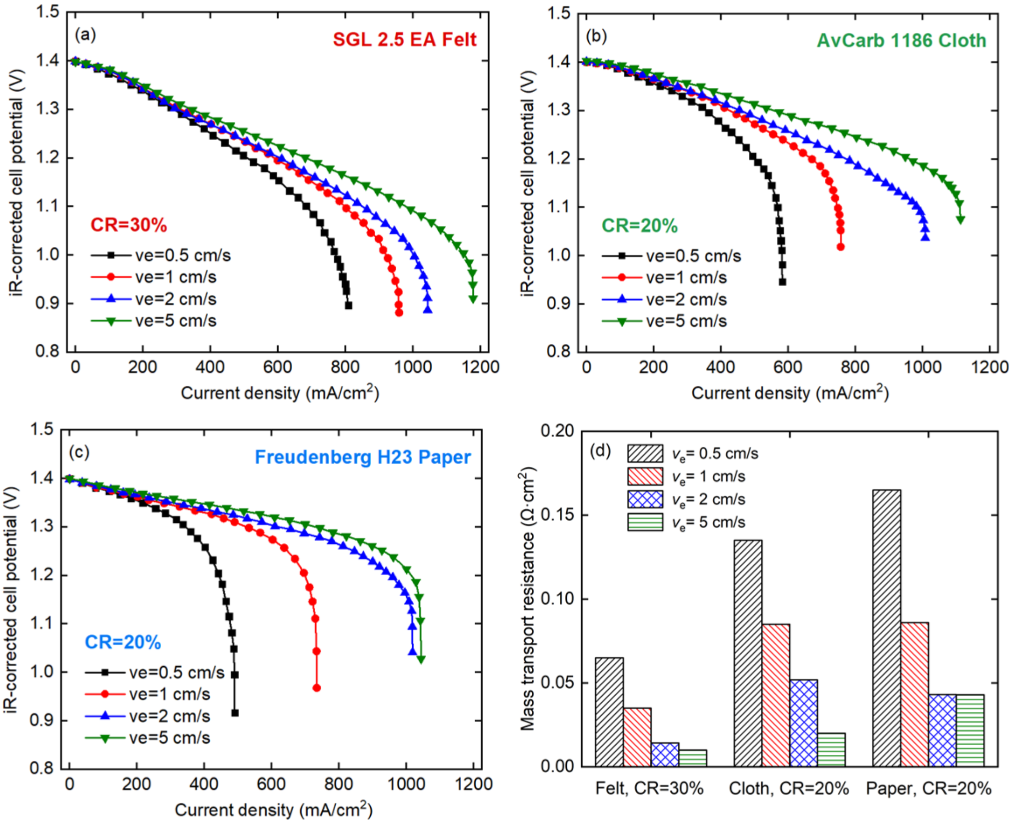

Figure 2.12 iR-corrected cell potential versus current densities at the electrolyte velocities of 0.5, 1, 2, and 5 cm/s for the (a) felt, (b) cloth, and (c) paper electrodes under the best-performing CRs (i.e., 30%, 20%, and 20%, respectively). The tests are measured under 50% SoC in a full-cell VRFB; (d) the mass transport resistances for the three electrodes under varying electrolyte velocities under the best-performed CRs.

The electrolyte velocity has a great impact on the battery performance. Low overpotentials are obtained at high v_e for all the three electrodes. The paper electrodes display the lowest overpotentials among the three electrodes in the low current density region, except for the v_e of 0.5 cm/s where R_{MT} is large. It is noted that at particularly high v_e (e.g., 5 cm/s), a reduced R_{MT} and an overall performance increase is still observed for felt and cloth.

However, there is no noticeable performance gain for the paper from 2 to 5 cm/s, as increasing v_e to > 2 cm/s does not yield a significant R_{MT} reduction for this electrode.

2.3.8 Performance and pressure drop trade-off

Elevated electrolyte velocities result in lower mass transport resistances, but also inevitably leads to an increase of the pressure drop. Low pumping losses are important for an overall high system efficiency. Herein, we attempt to connect the relationship between pressure drop and achievable current density as the metrics of hydraulic and electrochemical performance, respectively, for each type of the electrode. The achievable current density is extracted from iR-corrected polarization curves at the overpotential of 50 mV. Impacts of the electrolyte velocity and CR are illustrated in Fig. 2.13(a) and (b), respectively.

In Fig. 2.13(a), the four points on each curve represent the electrolyte velocity of 0.5, 1, 2, and 5 cm/s at the best-performed CRs for each electrode (i.e., 30%, 20%, and 20% for felt, cloth, and paper, respectively). We found that for the felt, a detrimental point has been reached at the electrolyte velocity of 5 cm/s where further increases of v_e brings little electrochemical performance gain but yields a large increase of the pumping losses. The cloth and paper electrodes both deliver excellent performance even at relatively low v_e. The paper electrodes yield a slightly better electrochemical performance (except for v_e=0.5 cm/s) compared to the cloth, but the pressure drop is ~3 times higher than that of the cloth under the same v_e. Cloth achieves a promising trade-off between performance and pressure drop. In Fig. 2.13(b), v_e is maintained at 2 cm/s to demonstrate the impact of CR. We found that the pressure drop increases with increasing CR, and becomes much amplified at high CRs especially for the paper and cloth. There is a turning point of the achievable current density with increasing CR for each of the three electrodes. After this, further increased CR results in both higher pressure drop and lower electrochemical performance. The turning points occur at 30%, 20%, and 20% CR for felt, cloth, and paper electrodes, respectively, which are identical to the best-performing CR with highest peak power density before iR-correction. Cloth maintains a good balance between the performance and pressure drop at moderate CRs.

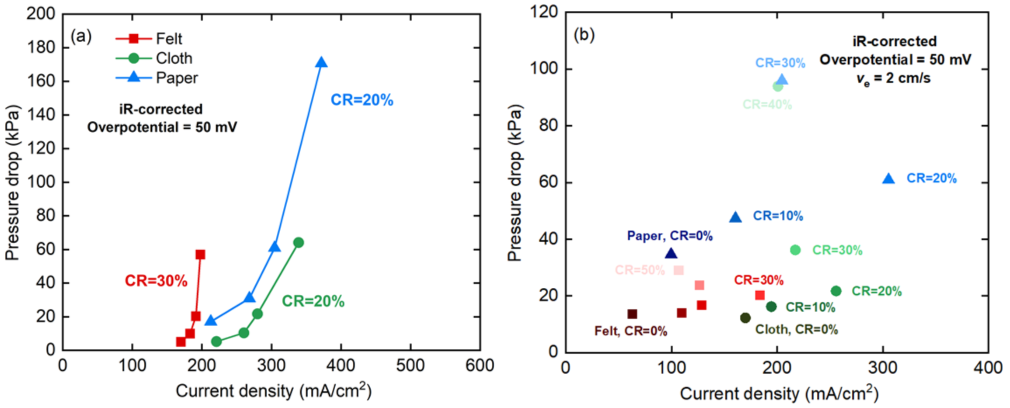

Figure 2.13 Pressure drop versus achievable current density under (a) different electrolyte velocities and (b) different CRs for the three electrodes. Best-performed CRs are selected as 30%, 20%, and 20% for the felt, cloth, and paper electrodes, respectively in (a), while electrolyte velocity is maintained as 2 cm/s in (b). The overpotential is selected as 50 mV after iR-correction.

2.3.9 Overall cell performance in cycling tests

To further confirm the performance of each electrode at its best-performing CR, we conduct a long-term charge-discharge cycling tests and summarize the coulombic efficiency (CE) and voltage efficiency (VE) as shown in Fig. 2.14(a). The cycling tests are conducted at current densities of 40-160 mA/cm^2 with 20 mL electrolyte on both the positive and the negative side. The current density rises by 20 mA/cm^2 every 6 cycles and returns back to 80 mA/cm^2 at the end. The whole cycling duration exceeds 150 h. The required pumping power of each electrode is presented in Fig. 2.14(b) based on the equation as follows:

$$P_{\text{pump}} = \frac{\Delta P \times Q}{\eta_{\text{pump}}} \tag{2.11}$$

where η_{pump} denotes pump efficiency (=0.7 in the present study [78]);
and the other parameters are defined above.

As anticipated, the paper electrodes maintain their high performance reflected in the high VE observed even at as high current density as 160 mA/cm^2, but the accompanying pumping power consumption is also very high. The test with a cell loaded with cloth electrodes consumes 50% of the pumping power of the cell with paper electrodes at the same electrolyte flow velocity (2 cm/s) and retains a VE above ~85% at current densities up to 120 mA/cm^2. We found the relatively inferior VE of the cloth at high current density regions compared to the paper electrodes. This is likely due to the low ESCA of the cloth used in this study, which needs to be further optimized.

In all the tests, the CE was above 91% during the entire cycling period. CE decreases with decreasing applied current density due to that the increasing (dis-)charge duration time allows more transmembrane crossover of active species [79]. Interestingly, we observed a lower CE for the tests with cloth electrodes compared to the other two electrodes. We found deep imprints of the woven pattern on the membrane after cycling for the cloth electrode (as shown in Fig. S2.9). This leads to stretching of the membrane and thus an increase of the effective surface area of it, along with an increased risk of membrane rupture. A larger membrane area with a thinned membrane is expected to lead to an increased crossover, consistent with the observed decrease of the CE.

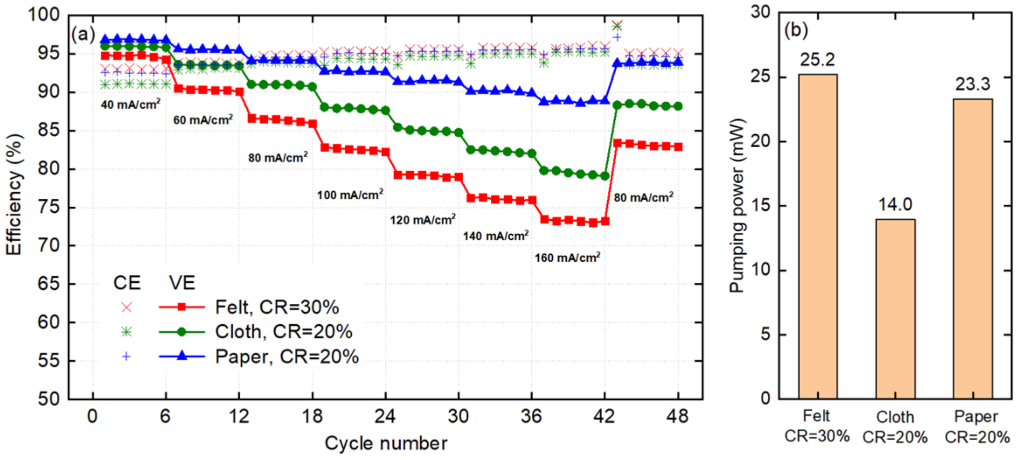

Figure 2.14 (a) Coulombic efficiency (dots) and voltage efficiency (dots and lines) versus charge-discharge cycle number under the 30%, 20%, and 20% CRs for the felt, cloth, and paper electrodes, respectively. The cycling tests were conducted at various current densities from 40 to 160 mA/cm^2, and the electrolyte velocity was set to 2 cm/s for all tests; (b) required pumping power for the three electrodes in the cycling tests.

2.4 Conclusions

In the present study we examined the electrochemical, microstructural, and pressure-drop characteristics of three types of binder-free, hydrophilic, carbon-fiber electrodes (i.e., felt, paper, and cloth) and investigated the relationship between electrode microstructure and operational vanadium flow battery performance using electrode compression of 0-50%. The electrode microstructure was charactered through X-ray μ-CT using a custom-made adjustable compression tool. Through image analysis, we found that the cloth, with its distinct periodically repeating woven structure, displays a bimodal pore size distribution, while the felt and paper electrodes possessed low-hierarchical fiber orientation with a more sparse or more dense inter-fiber connectivity, respectively. Under compression, the X-ray μ-CT measured porosity of the three electrodes decreased with CR increments, in good agreement with the predicted compressed porosity. For the cloth, pore compression mainly occurred of the large pores at the intersections between fiber bundles and was accompanied by significant deformation of the fiber bundles. The mean pore diameter of the cloth electrode decreased from 63.1 μm at CR=0% to 19.4 μm at CR=50%. Highly tortuous fibers within bundles were observed at excessive compressions. Such microstructure changes of the cloth had great impact on the fluid dynamic response. For the uncompressed cloth, the Darcy-Forchheimer permeability was 2.1×10^{-10} m^2, which was the most desirable among the three electrodes. But it deteriorated rapidly to 2.7×10^{-11} m^2 at 50% CR (i.e., reduced by one order of magnitude) as the result of the deformed and smaller pores, and tortuous electrolyte pathways, under applied compression. The paper electrodes are of low compressibility, due to their high fiber density and low porosity. The maximum CR before damage of the compression tool in X-ray μ-CT was 30%, and the low compressibility was validated through a mechanical strain-stress measurement as the compression stress rose rapidly to 1 MPa already at 22% CR. The in-plane tortuosity increased remarkably with CR increments compared to through-plane tortuosity for the paper electrode, which is likely due to that more fibers are oriented along the in-plane direction in this electrode.

We compared the X-ray μ-CT measured surface area and through-plane tortuosity through image analysis with the electrochemically obtained ECSA results. It was found that the ECSA of the three electrodes did not change much under varying CRs, except a slight decrease at extremely high CR of 50% for the felt and cloth. This fiber-to-fiber contact phenomenon is in accordance with what we observed in X-ray μ-CT. Interestingly, there was a slight increase of ECSA for the paper electrodes at a high CR of 40%. We speculate that this increase may be due to fiber breakage at such high compression.

We employed EIS to obtain decoupled ohmic, kinetic, and mass transport resistances in tests of full VRFB cells at 50% SoC under varying CRs. For the felt and paper, the ohmic resistance and contact resistance decreased with compression up to moderate compression ratios, while the cloth displayed smaller variation in ohmic resistance and no obvious contact resistance even 0% compression. This was reflected also in in the polarization curves of cells loaded with cloth electrodes, which showed relatively invariant performance under varying CRs (except at CR=50% where R_{MT} increased significantly). The R_{MT} of the felt and cloth was further reduced with increasing v_e from 2 to 5 cm/s, but with the paper electrodes R_{MT} was invariant at $v_e > 2$ cm/s. Overall, the optimal balance of highest achievable current density (extracted at the overpotential of 50 mV through iR-corrected polarizations) and satisfactory pressure drop for the felt, paper, and cloth came about at 30%, 20% and 20% CR, respectively. The cloth presented the best balance between the electrochemical performance and pressure drop. Owing to its distinct woven microstructure, it maintained >85% voltage efficiency before 120 mA/cm^2 at the best performing CR (i.e., 20%) and kept ~2 times lower pump consumption compared to the felt and paper electrodes at v_e=2 cm/s. The inferior performance of the cloth at higher current density was limited by ECSA, points to that further improvement could be sought for this electrode through a more aggressive pre-treatment protocol.

2.5 Supplementary Information

- **Microstructure and BET surface area before and after thermal treatment**

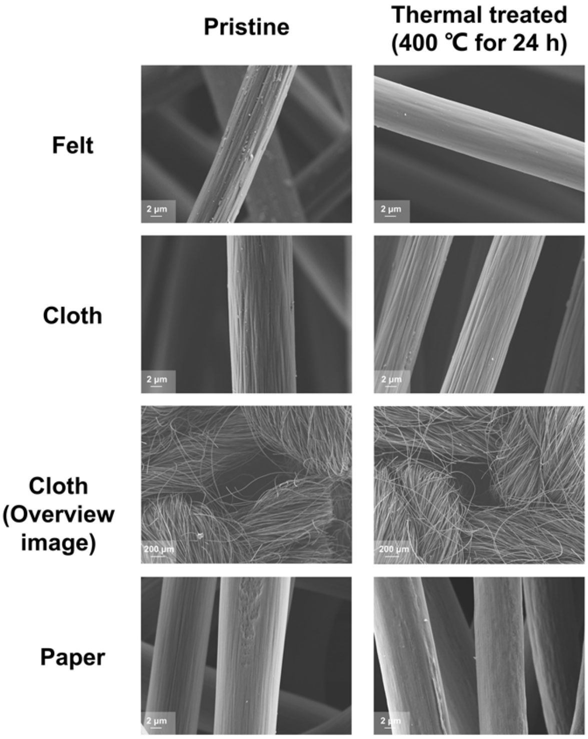

Figure S2.1 SEM microstructure images (captured in through-plane direction) of three uncompressed electrodes before and after thermal treatment.

Table S2.1 BET surface areas (m^2/g) of the three electrodes before and after thermal treatment at 0% CR

	SIGRACELL felt GFD 2.5 EA	AvCarb carbon cloth 1186 HCB	Freudenberg H23
Before treated	0.49	0.43	0.37
After treated	7.52	0.61	53.63

- **Relationship between Q and v_e**

Table S2.2 Relationship between volumetric flow rate and linear electrolyte velocity (v_e) through electrode cross-section area at different CRs

	CR	Volumetric flow rate (mL/min)			
	(%)	$v_e = 0.5$ cm/s	$v_e = 1$ cm/s	$v_e = 2$ cm/s	$v_e = 5$ cm/s
SGL 2.5 EA Felt	0	16.88	33.75	67.50	168.75
	10	15.19	30.38	60.75	151.89
	20	13.50	27.00	54.00	135.00
	30	11.81	23.63	47.25	118.13
	40	10.13	20.25	40.50	101.25
	50	8.44	16.88	33.75	84.38
AvCarb 1186 Cloth	0	8.61	17.21	34.43	86.06
	10	7.76	15.53	31.05	77.63
	20	6.75	13.50	27.00	67.50
	30	6.08	12.15	24.30	60.75
	40	5.06	10.13	20.25	50.63
	50	4.22	8.44	16.88	42.19
Freudenberg H23 Paper (3 layers)	0	4.22	8.61	16.88	42.19
	10	3.88	7.76	15.53	38.81
	20	3.38	6.75	13.50	33.75
	30	3.04	6.08	12.15	30.38
	40	2.53	5.06	10.13	25.31
	50	2.3	4.05	8.10	20.25

Compression tool using in X-ray μ-CT scan

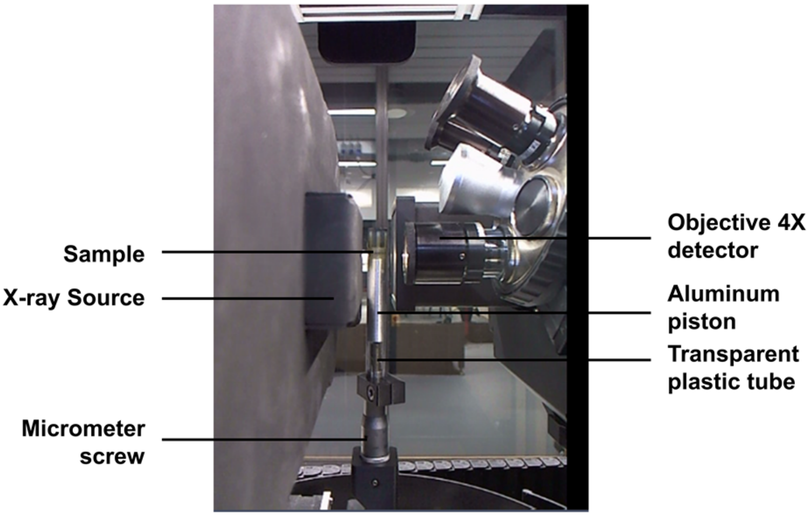

Figure S2.2 Picture of the custom-made compression tool stacked with electrode sample in VersaXRM-410 X-ray μ-CT.

Image process for X-ray μ-CT data

The original radiograms (from in-plane view) of the uncompressed samples in the compression tool are shown in Fig. S2.3. The samples are sandwiched between two incompressible plastic plates (2 mm thickness). From Fig. S2.3, we can find that there are clear boundaries between the sample region and the plastic plate regions, where we crop the image to only keep the sample region for volume renderings and microstructure property analysis.

To remove noises in the reconstructed data, we adopt the symmetric nearest neighbor (SNN) filter with a neighborhood size of 3 pixels. Fig. S2.4 shows example histograms of the uncompressed cloth before and after SNN filter. After SNN filter, there are obvious two peaks in the histogram representing two phases (i.e., fiber and air) in the image data. According to this, we can further conduct segmentation to separate the two phases, as shown in Fig. S2.5.

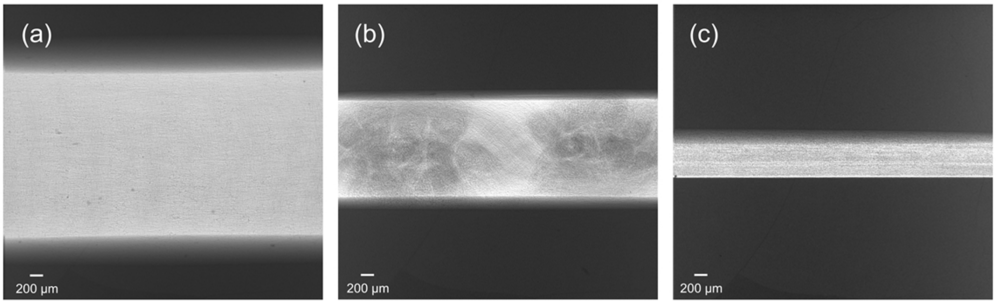

Figure S2.3 Radiograms of the uncompressed (a) felt, (b) cloth, and (c) paper (3 layers) sandwiched between two incompressible plastic plates in X-ray µ-CT scan.

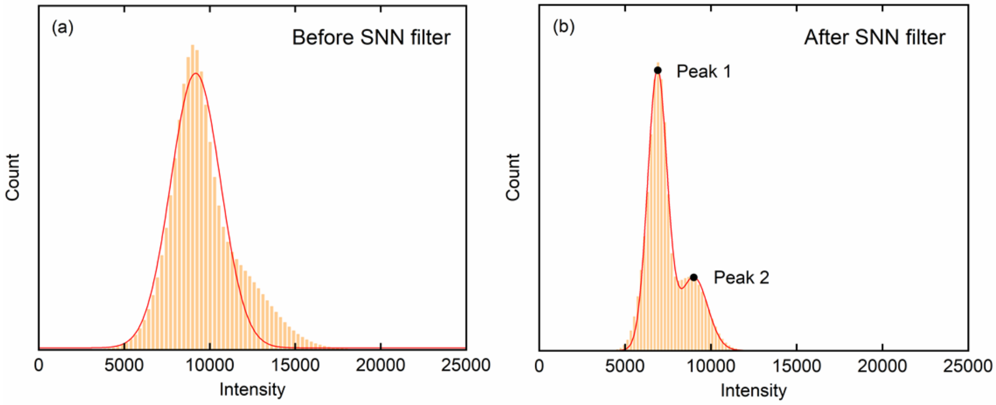

Figure S2.4 Histograms of the uncompressed cloth electrode (a) before and (b) after SNN filter with a neighborhood size of 3 pixels.

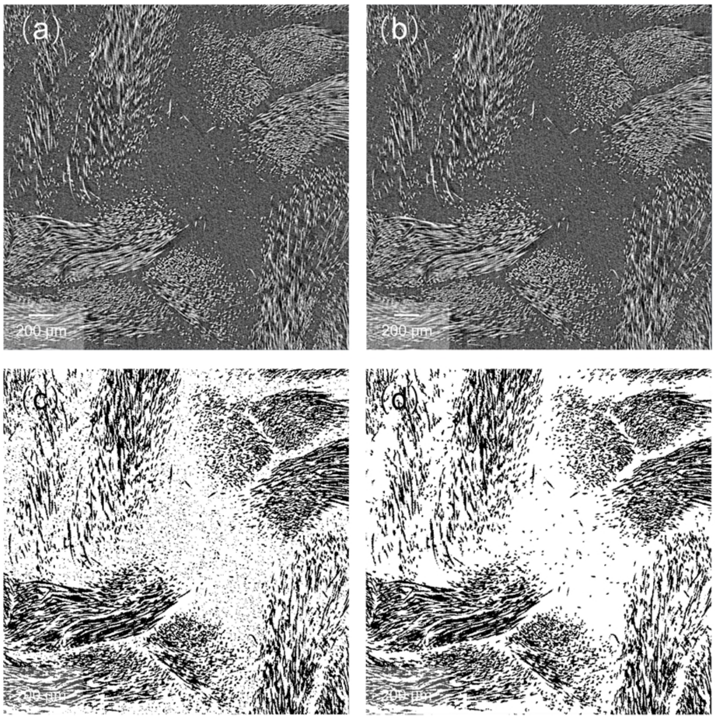

Figure S2.5 Example through-plane orthoslices for uncompressed AvCarb 1186 cloth (a) raw data, (b) after SNN filter with a neighborhood size of 3 pixels, (c) after segmentation, and (d) after removing isolated islands (< 50 voxels).

- **Impact of the pixel sizes on microstructure through image analysis**

In addition to the 4X objective detector, we also adopt the 20X objective detector for the uncompressed felt electrode to obtain high resolution X-ray μ-CT data with a pixel size of 1.68 μm. The scan is performed in a 4x4 binning mode with an exposure time of 16 seconds to acquire 3201 projections. The other parameter settings and image processing steps are the same as that under the 4X objective. The volume renderings of X-ray μ-CT data under 4X and 20X objective detectors are shown in Fig. S2.6. The morphological properties analyzed through Avizo are shown in Table S2.3.

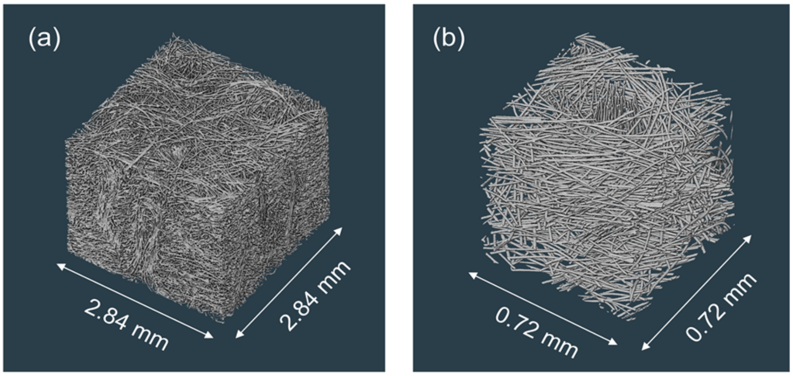

Figure S2.6 3D volume renderings of X-ray μ-CT data for the uncompressed carbon felt electrode under (a) 4X and (b) 20X objective detectors with the pixel sizes of 4.12 and 1.68 μm, respectively.

Table S2.3 Morphological properties for the uncompressed carbon felt electrode under 4X and 20X objective detectors

		4X objective	20X objective
Porosity (%)		89.7	94.9
Specific surface area (m^2/g)		0.13	0.51
Volumetric specific surface area (μm^{-1})		0.018	0.049
Tortuosity	x	1.27	1.05
	y	1.22	1.04
	z	1.26	1.07

In addition, the histograms of the pore diameter distribution before and after compression for three electrodes are shown in Fig. S2.7. The X-ray μ-CT data provides a rough pore distribution feature, more accurate distributions still need to be verified through mercury intrusion porosimeter (MIP).

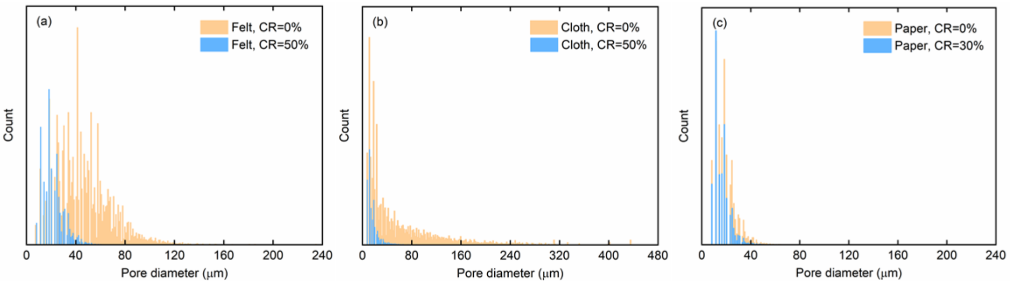

Figure S2.7 Histograms of the pore size distribution before and after compression for the (a) felt, (b) cloth, and (c) paper electrodes.

Pressure drop measurements

Table S2.4 Electrode permeability (κ) and non-linear Forchheimer coefficient (β) of the three electrodes obtained from pressure drop measurements

		SIGRACELL felt GFD 2.5 EA	AvCarb carbon cloth 1186 HCB	Freudenberg H23
κ (m^2)	CR=0%	1.77×10^{-10}	2.14×10^{-10}	6.65×10^{-11}
	CR=10%	1.45×10^{-10}	1.63×10^{-10}	4.77×10^{-11}
	CR=20%	1.24×10^{-10}	1.21×10^{-10}	3.60×10^{-11}
	CR=30%	1.03×10^{-10}	6.69×10^{-11}	3.00×10^{-11}
	CR=40%	8.11×10^{-11}	2.72×10^{-11}	-
	CR=50%	6.79×10^{-11}	-	-
β (m^{-1})	CR=0%	2.70×10^{5}	1.02×10^{5}	3.05×10^{5}
	CR=10%	7.17×10^{4}	1.62×10^{5}	4.40×10^{5}
	CR=20%	1.27×10^{5}	2.26×10^{5}	4.54×10^{5}
	CR=30%	1.78×10^{5}	2.64×10^{5}	2.87×10^{6}
	CR=40%	5.28×10^{4}	9.02×10^{5}	-
	CR=50%	1.35×10^{5}	-	-

- **EIS measurements under varying electrolyte velocities**

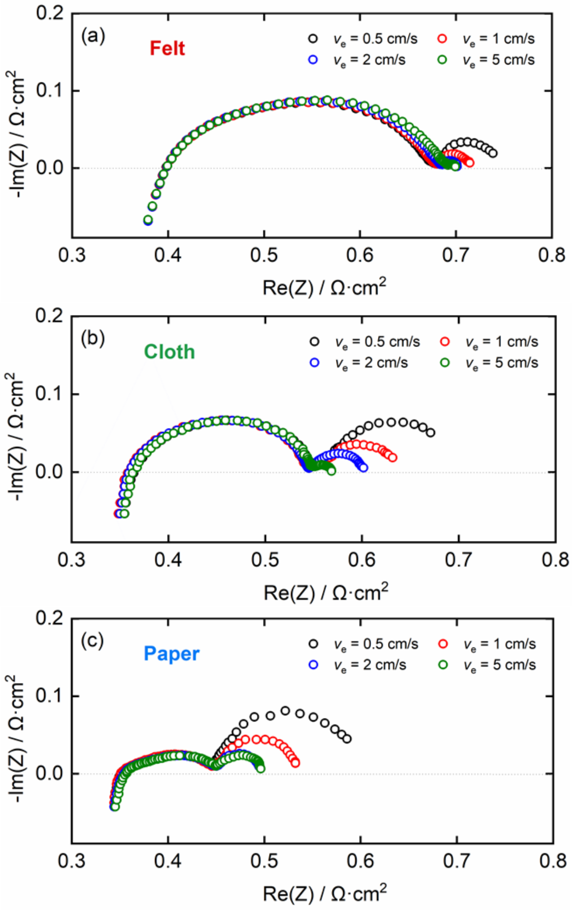

Figure S2.8 Nyquist plots obtaining through EIS measurements under varying electrolyte velocities for the (a) felt at 30% CR, (b) cloth at 20% CR, and (c) paper electrodes at 20% CR in a full-cell VRFB setup. The electrolytes for positive and negative sides are pre-charged and maintained at 50% SoC.

- **Cloth imprints on membrane**

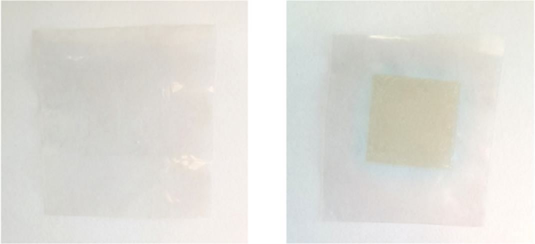

Electrode: paper
Membrane: FS-950
After 1 cycle

Electrode: paper
Membrane: FS-950
After 50 cycle

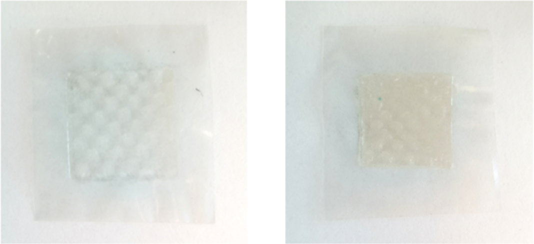

Electrode: cloth
Membrane: FS-950
After 1 cycle

Electrode: cloth
Membrane: FS-950
After 50 cycle

Figure S2.9 Optical photographs of the carbon cloth imprints on membrane before and after cycling tests.

References

[1] M. Rahman, A. Oni, E. Gemechu, A. Kumar. Assessment of energy storage technologies: A review. *Energy Conversion and Management*, 223, 113295 (2020).

[2] Y. Yao, J. Lei, Y. Shi, F. Ai, Y. Lu. Assessment methods and performance metrics for redox flow batteries. *Nature Energy*, 6, 582−588 (2021).

[3] M. Park, J. Ryu, W. Wang, J. Cho. Material design and engineering of next-generation flow-battery technologies. *Nature Reviews Materials*, 2, 16080 (2016).

[4] M. Duduta, B. Ho, V. Wood, P. Limthongkul, V. Brunini, W. Carter, Y. Chiang. Semi-Solid Lithium Rechargeable Flow Battery. *Advanced Energy Materials*, 1, 522−516 (2011).

[5] W. Wang, Q. Luo, B. Li, X. Wei, L. Li, Z. Yang. Recent Progress in Redox Flow Battery Research and Development. *Advanced Functional Materials*, 23, 970−986 (2013).

[6] B. Dunn, H. Kamath, J. Tarascon. Electrical energy storage for the grid: a battery of choices. *Science*, 334, 928−935 (2011).

[7] K. Lin, Q. Chen, M. Gerhardt, L. Tong, S. Kim, L. Eisenach, A. Valle, D. Hardee, R. Gordon, M. Aziz, M. Marsha. Alkaline quinone flow battery. *Science*, 349, 1529−1532 (2015).

[8] Z. Yuan, Y. Duan, H. Zhang, X. Li, H. Zhang, I. Vankelecomd. Advanced porous membranes with ultra-high selectivity and stability for vanadium flow batteries. *Energy & Environmental Science*, 9, 441−447 (2016).

[9] W. Li, Z. Zhang, Y. Tang, H. Bian, T. Ng, W. Zhang, C. Lee. Graphene-Nanowall-Decorated Carbon Felt with Excellent Electrochemical Activity Toward VO_2^+/VO^{2+} Couple for All Vanadium Redox Flow Battery. *Advanced Science*, 3, 1500276 (2016).

[10] R. Dmello, J. Milshtein, F. Brushett, K. Smith. Cost-driven materials selection criteria for redox flow battery electrolytes. *Journal of Power Sources*, 330, 261−272 (2016).

[11] J. Noack, L. Wietschel, N. Roznyatovskaya, K. Pinkwart, J. Tübke. Techno-Economic Modeling and Analysis of Redox Flow Battery Systems. *Energies*, 9, 627 (2016).

[12] R. Wang, Y. Li. Carbon electrodes improving electrochemical activity and enhancing mass and charge transports in aqueous flow battery: Status and perspective. *Energy Storage Materials*, 31, 230−251 (2020).

[13] A. Pezeshki, J. Clement, G. Veith, T. Zawodzinski, M. Mench. High performance electrodes in vanadium redox flow batteries through oxygen-enriched thermal activation. *Journal of Power Sources*, 294, 333−338 (2015).

[14] Z. Zhang, J. Xi, H. Zhou, X. Qiu. KOH etched graphite felt with improved wettability and activity for vanadium flow batteries. *Electrochimica Acta*, 218, 15−23 (2016).

[15] X. Zhou, T. Zhao, Y. Zeng, L. An, L. Wei. A highly permeable and enhanced surface area carbon-cloth electrode for vanadium redox flow batteries. *Journal of Power Sources*, 329, 247−254 (2016).

[16] K. Greco, A. Forner-Cuenca, A. Mularczyk, J. Eller, F. Brushett. Elucidating the Nuanced Effects of Thermal Pretreatment on Carbon Paper Electrodes for Vanadium Redox Flow Batteries. *ACS Applied Materials & Interface*, 10, 44430−44442 (2018).

[17] K. Greco, J. Bonesteel, N. Chanut, C. Wan, Y. Chiang, F. Brushett. Limited Accessibility to Surface Area Generated by Thermal Pretreatment of Electrodes Reduces Its Impact on Redox Flow Battery Performance. *ACS Applied Energy Materials*, 4, 13516−13527 (2021).

[18] L. Yue, W. Li, F. Sun, L. Zhao, L. Xing. Highly hydroxylated carbon fibres as electrode materials of all-vanadium redox flow battery. *Carbon*, 48, 3079−3090 (2010).

[19] Y. Zhao, L. Yu, X. Qiu, J. Xi. Carbon layer-confined sphere/fiber hierarchical electrodes for efficient and durable vanadium flow batteries. *Journal of Power Sources*, 402, 453–459 (2018).

[20] J. Milshtein, K. Tenny, J. Barton, J. Drake, R. Darling, F. Brushett. Quantifying Mass Transfer Rates in Redox Flow Batteries. *Journal of The Electrochemical Society*, 164, E3265–E3275 (2017).

[21] T. Wang, J. Fu, M. Zheng, Z. Yu. Dynamic control strategy for the electrolyte flow rate of vanadium redox flow batteries. *Applied Energy*, 227, 613–623 (2018).

[22] I. Mayrhuber, C. Dennison, V. Kalra, E. Kumbur. Laser-perforated carbon paper electrodes for improved mass transport in high power density vanadium redox flow batteries. *Journal of Power Sources*, 260, 251–258 (2014).

[23] C. Dennison, E. Agar, B. Akuzum, E. Kumbur. Enhancing Mass Transport in Redox Flow Batteries by Tailoring Flow Field and Electrode Design. *Journal of The Electrochemical Society*, 163, A5163–A5169 (2016).

[24] H. Jiang, B. Zhang, J. Sun, X. Fan, W. Shyy, T. Zhao. A gradient porous electrode with balanced transport properties and active surface areas for vanadium redox flow batteries. *Journal of Power Sources*, 440, 227159 (2019).

[25] W. Chen, J. Kang, Q. Shu, Y. Zhang. Analysis of storage capacity and energy conversion on the performance of gradient and double-layered porous electrode in all vanadium redox flow batteries. *Energy*, 180, 341–355 (2019).

[26] R. Cheng, J. Xu, J. Zhang, P. Leung, Q. Ma, H. Su, W. Yang, Q. Xu. Facile segmented graphite felt electrode for iron-vanadium redox flow batteries with deep eutectic solvent (DES) electrolyte. *Journal of Power Sources*, 483, 229200 (2021).

[27] S. Yoon, S. Kim, D. Kim. Optimization of local porosity in the electrode as an advanced channel for all-vanadium redox flow battery. *Energy*, 172, 26–35 (2019).

[28] Y. Kima, Y. Choi, N. Yun, M. Yang, Y. Jeon, K. Kim, J. Choi. Activity gradient carbon felt electrodes for vanadium redox flow batteries. *Journal of Power Sources*, 408, 128–135 (2018).

[29] D. Reed, E. Thomsen, B. Li, W. Wang, Z. Nie, B. Koeppel, V. Sprenkle. Performance of a low cost interdigitated flow design on a 1 kW class all vanadium mixed acid redox flow battery. *Journal of Power Sources*, 306, 24–31, (2016).

[30] J. Sun, M. Zheng, Y. Luo, Z. Yu. Three-dimensional detached serpentine flow field design for redox flow batteries. *Journal of Power Sources*, 428, 136–145 (2019).

[31] A. Bhattarai, N. Wai, R. Schweiss, A. Whitehead, T. Lim, H. Hng. Advanced porous electrodes with flow channels for vanadium redox flow battery. *Journal of Power Sources*, 341, 83–90 (2017).

[32] R. Wang, Y. Li, Y. He. Achieving gradient-pore-oriented graphite felt for vanadium redox flow batteries: meeting improved electrochemical activity and enhanced mass transport from nano- to micro-scale. *Journal of Materials Chemistry A*, 7, 10962 (2019).

[33] R. Wang, Y. Li, Y. Wang, Z. Fang. Phosphorus-doped graphite felt allowing stabilized electrochemical interface and hierarchical pore structure for redox flow battery. *Applied Energy*, 261, 114369 (2020).

[34] V. Beck, A. Ivanovskaya, S. Chandrasekaran, J. Forien, S. Baker, E. Duoss, M. Worsley. Inertially enhanced mass transport using 3D-printed porous flow-through electrodes with periodic lattice structures. *PNAS*, 118, e2025562118 (2021).

[35] J. Sun, H. Jiang, M. Wu, X. Fan, C. Chao, T. Zhao. A novel electrode formed with electrospun nano- and micro-scale carbon fibers for aqueous redox flow batteries. *Journal of Power Sources*, 470, 228441 (2020).

[36] C. Wan, R. Jacquemond, Y. Chiang, K. Nijmeijer, F. Brushett, A. Forner-Cuenca. Non-Solvent Induced Phase Separation Enables Designer Redox Flow Battery Electrodes. *Advanced Materials*, 33, 2006716 (2021).

[37] A. Forner-Cuenca, E. Penn, A. Oliveira, F. Brushett. Exploring the Role of Electrode Microstructure on the Performance of Non-Aqueous Redox Flow Batteries. *Journal of The Electrochemical Society,* 166, A2230–A2241 (2019).

[38] K. Tenny, A. Forner-Cuenca, Y. Chiang, F. Brushett. Comparing Physical and Electrochemical Properties of Different Weave Patterns for Carbon Cloth Electrodes in Redox Flow Batteries. *Journal of Electrochemical Energy Conversion and Storage*, 17, 041010 (2020).

[39] A. Wong, M. Aziz. Method for Comparing Porous Carbon Electrode Performance in Redox Flow Batteries. *Journal of The Electrochemical Society*, 167, 110542 (2020).

[40] A. Wong, S. Rubinstein, M. Aziz. Direct visualization of electrochemical reactions and heterogeneous transport within porous electrodes in operando by fluorescence microscopy. *Cell Reports Physical Science*, 2, 100388 (2021).

[41] Z. Cheng, K. Tenny, A. Pizzolato, A. Forner-Cuenca, V. Verda, Y. Chiang, F. Brushett, R. Behrou. Data-driven electrode parameter identification for vanadium redox flow batteries through experimental and numerical methods. *Applied Energy*, 279, 115530 (2020).

[42] R. Gorp, M. Heijden, M. Sadeghi, J. Gostick, A. Forner-Cuenca. Bottom-up design of porous electrodes by combining a genetic algorithm and a pore network model. *Chemical Engineering Journal*, 455, 139947 (2023).

[43] M. Sadeghi, M. Aganou, M. Kok, M. Aghighi, G. Merle, J. Barrale, J. Gostick. Exploring the Impact of Electrode Microstructure on Redox Flow Battery Performance Using a Multiphysics Pore Network Model. *Journal of The Electrochemical Society*, 166, A2121–A2130 (2019).

[44] J. Sun, M. Wu, X. Fan, Y. Wan, C. Chao, T. Zhao. Aligned microfibers interweaved with highly porous carbon nanofibers: A Novel electrode for high-power vanadium redox flow batteries. *Energy Storage Materials*, 43, 30–41 (2021).

[45] I. Zenyuk, D. Parkinson, L. Connolly, A. Weber. Gas-diffusion-layer structural properties under compression via X-ray tomography. *Journal of Power Sources*, 328, 364–376 (2016).

[46] P. Withers, C. Bouman, S. Carmignato, V. Cnudde, D. Grimaldi, C. Hagen, E. Maire, M. Manley, A. Plessis, S. Stock. X-ray computed tomography. *Nature Reviews Methods Primers*, 1, 18 (2021).

[47] M. Andisheh-Tadbir, F. Orfino, E. Kjeang. Three-dimensional phase segregation of micro-porous layers for fuel cells by nano-scale X-ray computed tomography. *Journal of Power Sources*, 310, 61–69 (2016).

[48] M. Kok, R. Jervis, T. Tranter, M. Sadeghi, D. Brett, P. Shearing, J. Gostick. Mass transfer in fibrous media with varying anisotropy for flow battery electrodes: Direct numerical simulations with 3D X-ray computed tomography. Chemical Engineering *Science*, 196, 104–115 (2019).

[49] D. Zhang, A. Forner-Cuenca, O. Taiwo, V. Yufit, F. Brushett, N. Brandon, S. Gu, Q. Cai. Understanding the role of the porous electrode microstructure in redox flow battery performance using an experimentally validated 3D pore-scale lattice Boltzmann model. *Journal of Power Sources*, 447, 227249 (2020).

[50] M. Kok, R. Jervis, D. Brett, P. Shearing, J. Gostick. Insights into the Effect of Structural Heterogeneity in Carbonized Electrospun Fibrous Mats for Flow Battery Electrodes by X-Ray Tomography. *Small*, 14, 1703616 (2018).

[51] R. Jervis, M. Kok, T. Neville, Q. Meyer, L. Brown, F. Iacoviello, J. Gostick, D. Brett, P. Shearing. In situ compression and X-ray computed tomography of flow battery electrodes. *Journal of Energy Chemistry*, 27, 1353–1361 (2018).

[52] B. Simon, A. Gayon-Lombardo, C. Pino-Muñoz, C. Wood, K. Tenny, K. Greco, S. Cooper, A. Forner-Cuenca, F. Brushett, A. Kucernak, N. Brandon. Combining electrochemical and imaging analyses to understand the effect of electrode microstructure and electrolyte properties on redox flow batteries. *Applied Energy*, 306, 117678 (2022).

[53] P. Ghimirea, A. Bhattarai, R. Schweiss, G. Scherer, N. Wai, Q. Yan. A comprehensive study of electrode compression effects in all vanadium redox flow batteries including locally resolved measurements. *Applied Energy*, 230, 974–982 (2018).

[54] R. Banerjee, N. Bevilacqua, A. Mohseninia, B. Wiedemann, F. Wilhelm, J. Scholta, R. Zeis. Carbon felt electrodes for redox flow battery: Impact of compression on transport properties. *Journal of Energy Storage*, 26, 100997 (2019).

[55] R. Gundlapalli, S. Jayanti. Effect of electrode compression and operating parameters on the performance of large vanadium redox flow battery cells. *Journal of Power Sources*, 427, 231–242 (2019).

[56] L. García-Alcalde, Z. González, A. Concheso, C. Blanco, R. Santamaría. Impact of electrochemical cells configuration on a reliable assessment of active electrode materials for Vanadium Redox Flow Batteries. *Electrochimica Acta*, 432, 141225 (2022).

[57] K. Zhang, C. Yan, A. Tang. Unveiling electrode compression impact on vanadium flow battery from polarization perspective via a symmetric cell configuration. *Journal of Power Sources*, 479, 228816 (2020).

[58] T. Chang, J. Zhang, Y. Fuh. Electrical, mechanical and morphological properties of compressed carbon felt electrodes in vanadium redox flow battery. *Journal of Power Sources*, 245, 66–75 (2014).

[59] L. Brown, T. Neville, R. Jervis, T. Mason, P. Shearing, D. Brett. The effect of felt compression on the performance and pressure drop of all-vanadium redox flow batteries. *Journal of Energy Storage*, 8, 91–98 (2016).

[60] S. Kumar, S. Jayanti. Effect of electrode intrusion on pressure drop and electrochemical performance of an all-vanadium redox flow battery. *Journal of Power Sources*, 360, 548–558 (2017).

[61] Q. Wang, Z. Qu, Z. Jiang, W. Yang. Experimental study on the performance of a vanadium redox flow battery with non-uniformly compressed carbon felt electrode. *Applied Energy*, 213, 293–305 (2018).

[62] S. Park, J. Shim, J. Yang, C. Jin, B. Lee, Y. Lee, K. Shin, J. Jeon. The influence of compressed carbon felt electrodes on the performance of a vanadium redox flow battery. *Electrochimica Acta*, 116, 447–452 (2014).

[63] M. Lu, W. Yang, X. Bai, Y. Deng, Y. He. Performance improvement of a vanadium redox flow battery with asymmetric electrode designs. *Electrochimica Acta*, 319, 210–226 (2019).

[64] N. Gurieff, V. Timchenko, C. Menictas. Variable Porous Electrode Compression for Redox Flow Battery Systems. *Batteries*, 4, 53 (2018).

[65] K. Tenny, K. Greco, M. Heijden, T. Pini, A. Mularczyk, A. Vasile, J. Eller, A. Forner-Cuenca, Y. Chiang, F. Brushett. A Comparative Study of Compressive Effects on the Morphology and Performance of Carbon Paper and Cloth Electrodes in Redox Flow Batteries. *Energy Technology*, 10, 2101162 (2022).

[66] J. Houser, J. Clement, A. Pezeshki, M. Mench. Influence of architecture and material properties on vanadium redox flow battery performance. *Journal of Power Sources*, 302, 369–377 (2016).

[67] R. Gundlapalli, S. Jayanti. Case studies of operational failures of vanadium redox flow battery stacks, diagnoses and remedial actions. *Journal of Energy Storage*, 33, 102078 (2021).

[68] R. Levie. On porous electrodes in electrolyte solutions: I. Capacitance effects. *Electrochimica Acta*, 8, 751–780 (1963).

[69] A. Pezeshki, R. Sacci, F. Delnick, D. Aaron, M. Mench. Elucidating effects of cell architecture, electrode material, and solution composition on overpotentials in redox flow batteries. *Electrochimica Acta*, 229, 261–270 (2017).

[70] J. Landesfeind, J. Hattendorff, A. Ehrl, W. Wall, H. Gasteiger. Tortuosity Determination of Battery Electrodes and Separators by Impedance Spectroscopy. *Journal of The Electrochemical Society*, 163, A1373–A1387 (2016).

[71] C. Sun, F. Delnick, D. Aaron, A. Papandrew, M. Mench, T. Jr. Resolving Losses at the Negative Electrode in All-Vanadium Redox Flow Batteries Using Electrochemical Impedance Spectroscopy. *Journal of The Electrochemical Society*, 161, A981–A988 (2014).

[72] M. Murbach, B. Gerwe, N. Dawson-Elli, L. Tsui. Impedance.py: A Python package for electrochemical impedance analysis. *Journal of Open Source Software*, 5, 2349 (2020).

[73] J. Brug, A. van der Eeden, M. Sluyters-Rehbach, J. Sluyters. The analysis of electrode impedances complicated by the presence of a constant phase element. *Journal of Electroanalytical Chemistry and Interfacial Electrochemistry*, 176 (1984) 275–295.

[74] A. Tang, J. Bao, M. Skyllas-Kazacos. Studies on pressure losses and flow rate optimization in vanadium redox flow battery. *Journal of Power Sources*, 248, 154–162 (2014).

[75] X. Zhou, T. Zhao, Y. Zeng, L. An, L. Wei. A highly permeable and enhanced surface area carbon-cloth electrode for vanadium redox flow batteries. *Journal of Power Sources*, 329, 247–254 (2016).

[76] H. Jiang, Y. Zeng, M. Wu, W. Shyy, T. Zhao. A uniformly distributed bismuth nanoparticle-modified carbon cloth electrode for vanadium redox flow batteries. *Applied Energy*, 240, 226–235 (2019).

[77] M. León, L. Castañeda, A. Márquez, F. Walsh, J. Nava. Review—Carbon Cloth as a Versatile Electrode: Manufacture, Properties, Reaction Environment, and Applications. *Journal of The Electrochemical Society*, 169, 053503 (2022).

[78] Y. Li, X. Zhang, J. Bao, M. Skyllas-Kazacos. Studies on optimal charging conditions for vanadium redox flow batteries. *Journal of Energy Storage*, 11, 191–199 (2017).

[79] M. Pugacha, M. Kondratenko, S. Briola, A. Bischi. Zero dimensional dynamic model of vanadium redox flow battery cell incorporating all modes of vanadium ions crossover. *Applied Energy*, 226, 560–569 (2018).

Chapter 3

Electrochemical Performance of Dual-layer Carbon Electrodes for Aqueous Redox Flow Batteries

Baichen Liu[a], Salvatore De Angelis[a], Vedrana Andersen Dahl[b], Søren Bredmose Simonsen[a], Johan Hjelm[a*]

[a] Department of Energy Conversion and Storage, Technical University of Denmark, Building 310, DK-2800 Kgs. Lyngby, Denmark
[b] Department of Applied Mathematics and Computer Science, Technical University of Denmark, Building 310, DK-2800 Kgs. Lyngby, Denmark

[*] Corresponding author: johh@dtu.dk

Abstract

Recognizing the urgent need of further cost reduction to drive wider adoption of redox flow batteries, it is critical to improve the reactor performance, which has been regarded as a key approach to reduce the stack size as well as the high capital cost. As one of the main contributors to reactor internal resistance, porous electrodes with properly designed structure and optimized physiochemical properties offer pathways for reduced voltage losses, including kinetic and concentration overpotentials. Recently, carbon cloth electrodes have been explored in flow battery applications owing to their bimodal pore size distributions, which opens a potential opportunity for improved mass transport behavior. The woven structure of cloth provides flexibility in the electrode designs through variation of the weave pattern, but finding a suitable trade-off between the electrolyte penetration pathways and abundant active surface area is still a challenge. In the present study, we investigate a dual-layer electrode configuration to simultaneously meet the requirements of high active surface area, low mass transfer resistance, and low pressure drop. A carbon

cloth was placed close to the flow plate to serve as electrolyte distributor to ensure efficient mass transport in a lateral flow through configuration, while a carbon paper sub-layer was placed near the membrane to provide a high density of reaction sites. Two types of carbon cloth with different weave patterns were selected in combination with the carbon paper. To decouple the electrochemical losses and provide in-depth understanding of the performance gain, electrochemical measurements were conducted in a symmetric vanadium flow battery setup. Quantitative analysis of contributions from each type of polarization was investigated under both V^{2+}/V^{3+} and VO^{2+}/VO_2^+ redox couples. The Lattice Boltzmann Method was adopted based on the 3-D reconstructed electrode structure to provide insight into the electrolyte distribution and the electrolyte velocity profile within the dual-layer electrode assembly. We found that a single-layer carbon cloth electrode imprinted its woven pattern on the ion exchange membrane after battery assembly due to the unevenness of the surface. The sub-layer of carbon paper served as a protective layer to avoid excessive stretching and mechanical failure of the membrane and resulting increase of crossover induced capacity decay. Overall, the results showed that the investigated strategy is an effective way to achieve high electrochemical performance and low pressure drop. It can be regarded as a promising approach for boosting system efficiency while maintaining long-term stability in a flow-through configuration.

3.1 Introduction

Redox flow batteries (RFBs) are considered as one of the most suitable technologies for medium to large-scale energy storage applications [1][2]. Such applications are expected to be able to support peak-shaving, enhance grid stability, and facilitate integration of intermittent renewables, such as wind and solar energy [3], in the electrical grid. In recent years, significant efforts have been made to improve flow battery performance through development of critical battery components, including electrolytes [4][5], membranes [6][7], electrodes [8][9], etc. Increasing the efficiency of the reactors and ensuring long-term operational stability represent important pathways to bringing down the high capital cost of the state-of-the-art RFBs [10].

Porous electrodes are core components within the reactor, which provide electrochemical reaction sites and electrolyte transport pathways. The electrode physico-chemical properties and microstructure are closely linked to battery performance [11]. Popular carbon-fiber porous electrodes adopted in RFBs include carbon felt [12][13], carbon paper [14][15], and carbon cloth [16][17]. They possess advantageous low chemical corrosion and high electrical conductivity, but also suffer from relatively low surface area, impacting the battery performance. Numerous studies have been conducted to improve the hydrophilicity and active surface area, such as pre-treatment approaches [18], pore etching [19], and surface modification [20][21]. However, it remains a challenge to simultaneously meet the requirements of high active surface area for reduced kinetic resistance, and a consistent pore network with appropriate pore sizes for enhanced permeability and mass transfer properties [22].

To overcome the high pressure drop in electrodes with large volumetric specific surface area (electrodes with a high fiber density, e.g., carbon paper [23]), numerous flow field designs on the flow plates used in single cell test hardware (e.g., serpentine [24][25], interdigitated [26][27], etc.) have been developed to enable "flow-by" electrolyte flow over the electrode surface and force convection into the electrode structure to enhance local mass transport. RFBs with flow field designs have been shown to exhibit higher peak power density and round-trip efficiency compared to those without flow fields (i.e., flow-through configuration) [28]. Balancing the interactions between the flow fields and porous electrodes is important to optimize the transport behavior and related losses [29]. Considering the relatively low flexibility of the electrode internal structure, more efforts have been put into optimization of flow fields including geometric channel and land sizes [30][31] and flow pathway designs [32][33] to obtain homogeneous electrolyte distributions and low mass transfer losses. A common geometry in industrial stacks is the use of planar bipolar plates without integrated flow fields. A possible method to enable higher electrolyte flow velocities at a low pressure drop penalty is to use a bimodal pore size distribution in the flow through electrode. Carbon cloths, due to the flexibility of woven pattern designs offers access to a range of bimodal pore size distributions [34][35], and provide some potential to partially take on the function of a flow field to facilitate electrolyte penetration along the woven direction at low pressure drop.

Instead of continuous random fibers to form carbon felt and paper, carbon cloth is a woven structure and consists of periodically repeating bundles of carbon fibers from longitudinal (warp) and transverse (weft) directions without binders. The size of the fiber bundles and woven methods allow versatile cloth designs, such as plain, twill, baskets, and satin [36]. Also, the fiber bundle arrangements create hierarchical pore size distributions including the intersection void between fiber bundles (e.g., ~10-100 μm), fiber-to-fiber distance (e.g., ~1-10 μm), and meso-pores on individual fiber surfaces (e.g., 2-50 nm). Due to the presence of large voids at fiber-bundle intersections and a well-defined microstructure, carbon cloth has been shown to be a high performance electrode with reduced mass transfer resistance and pressure drop in a full-cell RFB system [37]. The physical and electrochemical properties of carbon cloth with different woven patterns were compared in both aqueous [37] and non-aqueous [38] RFBs. Although the effectiveness of carbon cloth electrodes in RFBs was validated, the local mass transport behavior still needs in-depth investigation. Modeling and simulation work is an effective approach to investigate the fluid dynamics [39]. However, the non-uniform internal structure of carbon cloth adds significant complexity to the simulations using finite element methods. Zhang et al. [40] adopted the computationally inexpensive Lattice Boltzmann Method (LBM) in conjunction with X-ray computed tomography to simulate electrode permeability and velocity profiles in carbon cloth electrodes. Topological pore network models have been employed to simulate local flow distributions in porous electrodes [41][42]. In this work we further explore the influence of the cloth structure on local mass transport and how it distributes between layers in a dual-layer electrode.

Inspired by the periodic woven structure of carbon cloth, we focused on a dual-layer (DL) electrode configuration in the present study, where the carbon cloth is placed near the flow plates (corresponding to the bipolar plate in a stack) and the carbon paper placed adjacent to the membrane. The carbon cloth serves as a simplified flow field, and the through-plane electrolyte convection can support efficient mass transfer into the carbon paper. Some double-layer [43][44][45][46][47] or triple-layer electrode [48] structures in RFBs have been proposed in literature with the combination of carbon felt and carbon paper. Multi-layer carbon paper electrodes with gradient porosity [49][50], multi-segmented carbon felts [51], asymmetric electrode designs for negative and positive sides [52][53] were also proposed for enhanced reactor performance. However, the benefits were relatively limited due to the minor impacts on flow behavior from the uniform electrode structure. Wu et al. [54] proposed an electrode assembly with combinations of carbon cloth and an electrospun carbon fiber mat coupled with different flow fields. Such an electrode assembly proved to be beneficial to improve the energy efficiency under an interdigitated flow field. Here we explore the use of carbon cloth itself as a flow-field in a flow-through configuration, in combination with carbon paper as the active electrode.

In addition to the coupled influence between flow field and porous electrodes, the interactions between electrode and membrane, which are known as membrane electrode assembly (MEA) in fuel cell [55] and electrolysis [56], received less attention in RFBs. The electrolyte transport process within electrode may also change the transmembrane process of active species [57]. Lu et al. [58] proposed an asymmetric electrode compression design to adjust the convection flux through the membrane to mitigate the crossover of active species. The electrode morphology on both sides may impact the shape and integrity of the thin polymer membrane under compression, especially considering the relatively large unevenness of the carbon cloth surface. The uneven compression across the membrane surface may lead to aggravated capacity losses and even membrane failure at high degrees if deformation or stretching of the membrane.

In the present study, two carbon cloths with different woven structures were selected and combined with carbon paper. The pressure drop and electrochemical performance of the DL configuration were measured and compared to those of single-layer electrodes. Quantitative analysis for polarization losses was performed using symmetric vanadium single-cell RFBs with a flow-through flow field (FT-FF). To understand local mass transport behavior of carbon cloth, X-ray CT was employed in combination with LBM simulations to provide insight into electrode flow distribution and velocity profiles. The results showed that the DL configuration is an effective strategy to obtain decreased overall kinetic and mass transfer resistances. The full-cell overpotential reaches ~0.08 V at 100 mA/cm^2, a decrease of ~35% and ~17% compared to single-layer carbon cloth and paper, respectively.

3.2 Experimental methods

3.2.1 Electrode preparation

Two woven carbon cloth electrodes (AvCarb 1186 HCB and ELAT-H) and a non-woven carbon paper electrode (Freudenberg H23) were investigated in the present study. AvCarb 1186 is woven in 2x2 baskets, and ELAT-H is a plain weave with thinner fiber bundles compared to AvCarb 1186. All electrodes were cut to 5 cm^2 squares and thermally treated at 400 ^{o}C for 24 hours in air to ensure hydrophilicity before assembled into the battery setup. In this work, AvCarb 1186 and ELAT-H carbon cloth were combined with Freudenberg H23 carbon paper, respectively, referred to as A-FDL and E-FDL electrode assemblies. The three individual electrodes were tested, and their performance contrasted with the two double layer electrode assemblies.

3.2.2 Electrode microstructure characterization

X-ray computed tomography (CT) was used to capture the internal microstructure of the selected electrodes. The electrode sample after thermal treatment was cut to a cylinder with the diameter of ~1 cm and placed in a sample holder in a ZEISS XRadia 410 Versa. The sample holder was rotated for 360 degrees between the between the X-ray source and detector with 4X objective during scanning. A 40 kV source voltage and a 10 W power were adopted. A pixel size of 4.12 μm was obtained by adjusting the source-sample-detector distance, which was effective to capture the individual fiber of the selected electrodes with the diameter of ~10 μm. A 2x2 binning mode and a 3 s exposure time were used. After obtaining the raw data, it was reconstructed through the commercial software Avizo. A symmetric nearest neighbor filter was used with a neighborhood size of 3 pixels to remove noise. Segmentation was conducted to separate the air and fiber phases through determining a threshold of the average count between two peaks in histogram. Isolated islands were removed when <50 voxels.

Mercury Intrusion porosimetry (MIP) was adopted to estimate the pore size distributions of the selected samples through a PoreMaster 33 instrument. The used pressure range was from 1 to 60,000 kPa. Brunauer-Emmett-Teller (BET) measurement was conducted through an Autosorb-1 equipment. The electrode sample was cut to ~0.15 g for both measurements.

3.2.3 Flow cell testing

A single-cell flow battery reactor with the active area of 5 cm^2 (Fuel Cell Technologies) was assembled. Two prepared electrode samples were placed in the cavity of two incompressible polytetrafluoroethylene (PTFE) gaskets. Gaskets of different thickness (min. 25 μm) were used to adjust the electrode compression to 20±2%. A 10 μm thickness meta polybenzimidazole (m-PBI) membrane (Blue World Technologies) was sandwiched in between the two electrodes to separate the anode and cathode. To increase the membrane conductivity, the m-PBI membrane was pre-activated in 10 M H_2SO_4 solution for 24 h and then in 4 M H_2SO_4 solution for >24 h. Two FT-FFs were placed near the other side of the electrodes. Two aluminum alloy end plates and two gold-plated current collectors (an insulating layer covered one side on each current collector) were clamped from the outside with 8 bolts under 6 N·m torque.

A single-tank symmetric cell setup was established as shown in Fig. 3.1. Perfluoroalkoxy alkane (PFA) tubing and tube fittings (Swagelok) were used to connect to a peristaltic pump (Shenchen LabV1) and a sealed glass bottle stored with electrolytes. Two flow pulsation dampeners (KNF FPD 06) were adopted to stabilize the electrolyte flow. In the present study, we investigated both a negative (i.e., V^{2+}/V^{3+}) and positive (i.e., VO^{2+}/VO_2^+) vanadium symmetric cell. In order to prepare the required electrolytes, the original electrolyte (Oxkem) containing 1.6 mol/L vanadium species (V^{3+}:VO^{2+}:=1:1), 4 mol/L sulphate, and 0.05 mol/L phosphoric acid was pre-charged to 50% state-of-charge (SoC) in a two-container battery configuration. The electrolytes from two sides were purged with argon and stored separately for negative and positive symmetric cell tests. During battery tests, the symmetric cell setup was placed in a sealed cabinet under argon atmosphere (O_2 partial pressure <0.1%). A Bio-Logic SP-300 potentiostat was used to collect data from electrochemical impedance spectroscopy (EIS) and polarization measurements. EIS data was recorded at a zero-to-peak amplitude of 10 mV and a frequency range from 200 kHz to 50 mHz with 8 points per frequency decade. Polarization data was recorded by linear sweep voltammetry at 5 mV/s from open circuit voltage (i.e., 0 V) to 0.8 V.

For mass transfer coefficient (k_m) measurements, the original vanadium electrolytes were first diluted to 0.1 mol/L (V^{3+}:VO^{2+}:=1:1) using 2 mol/L H_2SO_4 to maintain the sulphate concentration, and then pre-charged to 50% SoC. We assumed the mass transport properties were independent of the types of redox couples. Hence, we only collected the positive electrolyte (i.e., VO^{2+}/VO_2^{+}) to establish a symmetric cell and assumed the k_m was equal to that from the negative side (i.e., V^{2+}/V^{3+}). Five different volumetric flow rates (e.g., 2.5, 5, 10, 15, and 20 mL/min) were used. For each flow rate, linear sweep voltammetry was performed at 5 mV/s scan rate from 0 V to max. 1.4 V until the current reached a plateau, which was regarded as the limiting current to determine the k_m. The detailed calculation was shown in *Supplementary Information*.

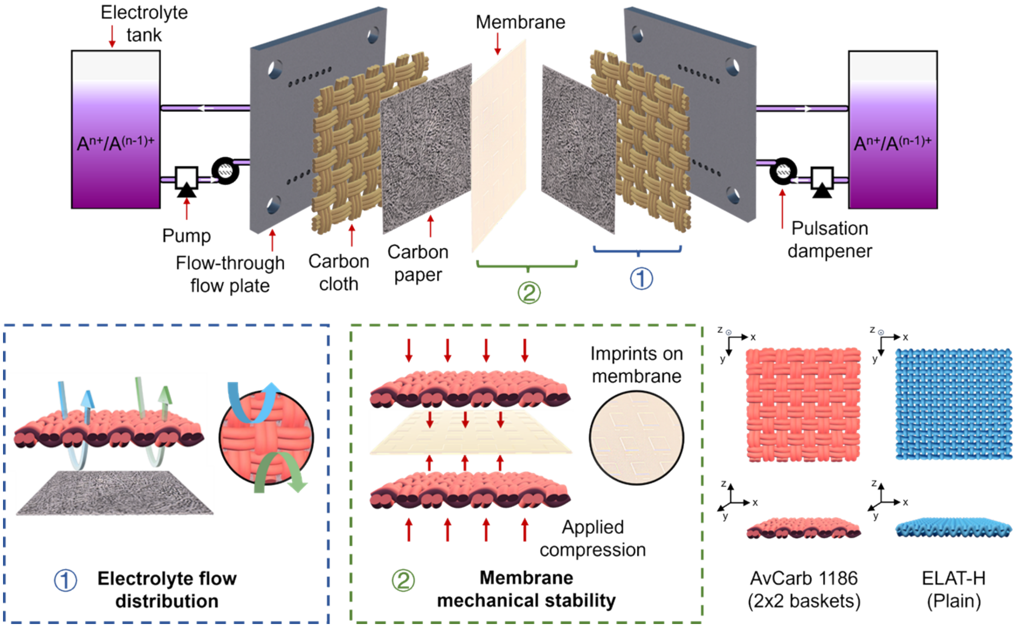

Figure 3.1 Schematic of the dual-layer electrode designs in a flow-through configuration of a symmetric cell. The woven structures of the two carbon cloth selected in this study are shown in the bottom right.

For full-cell vanadium cycling tests, 20 mL electrolytes were used in positive and negative sides of a two-container battery configuration. The current density was decreased from 160 to 60 mA/cm^2 by 20 mA/cm^2 and returned back to 80 mA/cm^2 at the end. Three charge-discharge cycles were performed at each current density. For self-discharge capacity retention tests, the electrolytes were pre-charged to 1.6 V using a constant current-constant voltage (CC-CV) sequence. The constant current was set to 100 mA/cm^2 and constant voltage period was set to run until the current decreased to 10 mA. Then, the electrolyte was allowed to continue to circulate at a superficial velocity of 2 cm/s and the cell potential was recorded for >200 h.

3.2.4 Pressure drop measurement

The electrode permeability was estimated through pressure drop measurements. A one-container battery configuration, similar to the single-tank cell described above, was adopted without the two flow pulsation dampeners. Two pressure sensors (Grundfos Direct Sensors, RPS 0-2.5) were connected at the inlet and outlet of the battery on one side to collect the pressure signal. The electrode pressure drop was obtained after subtracting the pressure drop from an empty cell without electrode assembled to eliminate the impact from tubes, fittings, etc. The working fluid in the pressure-drop measurements was deionized water (18 MΩ).

3.2.5 Membrane morphology characterization

After self-discharge capacity retention tests, the membrane under different electrode adoption was washed using demi-water, dried at room temperature, and collected. An optical profilometer (Sensofar S Neox 3D) was used to capture the imprints from the electrodes on the membrane surface after battery assembly. A detector with 10X objective in the confocal mode was adopted. The pixel size of all the images was 1.38 μm. Stitched images of 2x2 were made for all the samples to display the overall surface structure. The image data was rendered and analyzed in SensoVIEW.

3.3 Computational methods

3.3.1 Fiber orientation visualization through structure tensor method

The fiber orientations of the three selected electrodes in the present study were visualized through a structure tensor computational model established in a previous study [59][60]. For completeness, we briefly describe the structure tensor and the process of orientation visualization here. More details about the model establishment can be found in Ref. [60].

A structure tensor is a 3x3 matrix that summarizes orientation in the neighborhood around a point. The orientation was estimated through calculating the gradients and integration between the points at each voxel position. Gaussian filters were involved in the structure tensor calculation to remove noise and integrate gradients, where a noise scale of 0.5 and an integration scale of 2 were selected in the present study. A unit vector was adopted to estimate the predominant orientation direction through determining the direction of the least change in intensity, that is, the orientation of the fiber structure. In the present study, the raw data-set obtained from X-ray CT scans was imported in the fiber orientation analysis. The predominant orientation was visualized on the image through a DUO sphere colormap to emphasize the in-plane orientations.

3.3.2 Lattice Boltzmann Method

To better understand the flow distribution in the dual-layer electrode configurations, qualitative flow simulations using LBM were performed in the open-source library Palabos [61] using 16 nodes with 8 processors per node. The image data (301x301x100 voxels) of dual-layer electrode configurations were constructed digitally through separate datasets of carbon cloth and carbon paper obtained through X-ray CT after segmentation. A pressure gradient was imposed between the two sides along the cross-section of the electrodes to represent lateral flow in FT-FF under practical battery condition. It is noted that the present results are only qualitative, and more effort is needed to carefully match the simulations' boundary conditions with real-world experiments. Furthermore, a bigger volume should be simulated to avoid edge effects and be more representative of the real device. More quantitative simulations will be performed in a future study.

3.4 Results

3.4.1 Design of the dual-layer electrode configurations

The idea of the DL electrode configurations is to utilize the woven structure from carbon cloth as simple flow channels to facilitate electrode penetration without high pressure losses, and a sub-layer of carbon paper to ensure adequate active surface area. The weave and the fiber bundle diameter of the carbon cloth determines the size of the large pores between the fiber bundles, which are linked to the electrolyte penetration properties and the pressure drop. To illustrate the woven structure of the two selected carbon cloth, the 3D reconstructed volume renderings and example through-plane and in-plane slices from X-ray CT raw data are presented in Fig. 3.2. The carbon paper is also shown as a comparison. The two carbon cloths show unique periodically woven structures. AvCarb 1186 is constructed with 2x2 baskets with a weave periodicity of 4 cm^{-1}. The large fiber bundles leave relatively large voids (~500 μm, measured from X-ray CT slices) at the intersection between the bundles, which are expected to reduce the flow resistance significantly. ELAT-H is a plain-weave with the weave periodicity of 20 cm^{-1}. The pores at the intersection between the fiber bundles are ~200 μm (measured from X-ray CT slices). Compared to the two carbon cloths, Freudenberg H23 carbon paper is a non-woven electrode constructed through randomly distributed carbon fibers. It possesses relatively uniform pore size distribution with the pore diameter of ~10 μm between individual carbon fibers.

In addition, the electrode physical properties are summarized in Table 3.1. According to the results of the BET measurements, the carbon paper possesses the highest volumetric specific surface area (α_v), which renders it a suitable for use as a sub-layer to carbon cloth for providing a large amount of active reaction sites. The α_v results presented in Table 3.1 are measured from the pristine samples before thermal treatment. The results can be affected by the thermal pretreatment temperature and duration, and there is no single optimal temperature for different types of electrodes. In the present study, we used the same process of thermal treatment for all electrodes to ensure hydrophilicity. In-depth investigations are considered in the future study.

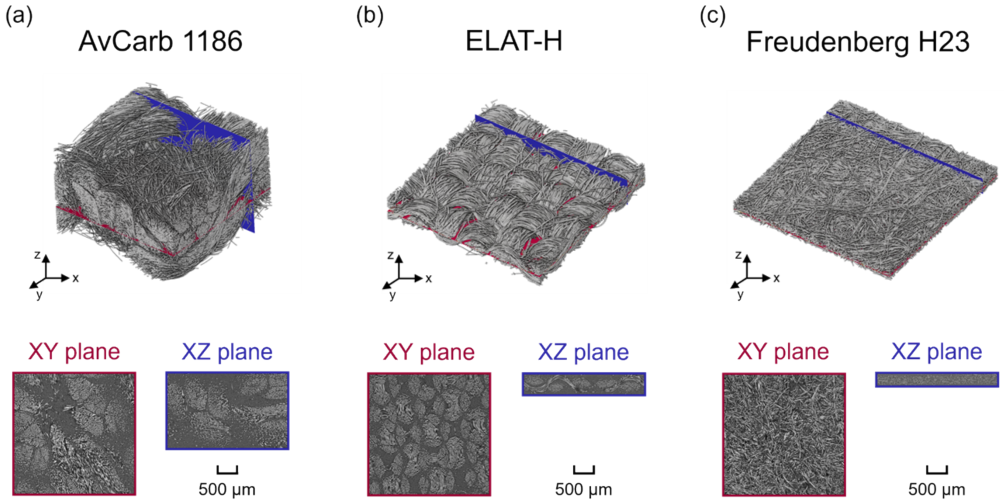

Figure 3.2 Volume renderings of the X-ray CT data for uncompressed (a) AvCarb 1186 carbon cloth, (b) ELAT-H carbon cloth, and (c) Freudenberg H23 carbon paper. XY and XZ plane slices of each electrode from X-ray CT raw data are presented.

Table 3.1 Electrode physical properties with averages (n=5)

Electrode name	AvCarb 1186 HCB	ELAT Hydrophilic	Freudenberg H23
Woven type	2x2 baskets	plain	non-woven
Weave periodicity* (cm^{-1})	4	20	n/a
Uncompressed thickness* (µm)	1270	406	210
Measured thickness# (µm)	1440±50	400±30	200±10
Average weight* (g/m^2)	525	130	95
Measured weight# (g/m^2)	512±7	131±5	92±4
Uncompressed porosity (%)	82 [38]	80*	80*
BET surface area# (m^2/g)	0.43	0.49	0.77
Volumetric surface area# (m^2/m^3)	161000	158200	367200

* Provided by the manufacture datasheet.

Measured from the samples before thermal treatment.

To investigate electrode compression effects in practical battery tests, we combined the two carbon cloths individually with the carbon paper to assemble the two dual-layer configurations (i.e., A-FDL and E-FDL). The two DL assemblies were placed in a custom-built compression tool in which an overall through-plane compression ratio of ~20% was applied. X-ray CT was employed to characterize the electrode morphology under compression, and the results are shown in Fig. S1. The compression was found to be evenly distributed between the carbon cloth and the carbon paper (in the through-plane direction) for E-FDL. However, for A-FDL, the carbon cloth was compressed by ~24%, and the carbon paper layer only by ~2%. The uneven compression of the A-FDL is likely due to that AvCarb 1186 carbon cloth is thicker and has larger internal large voids (~500 μm, measured from X-ray CT slices) between fiber bundles than ELAT-H and the carbon paper, and is thus more prone to be compressed.

After electrode microstructure characterization, pressure drop measurements were conducted to investigate the performance of the carbon cloth as an electrolyte flow-field in the DL configurations. Fig. 3.3(a) shows the pressure-drop results of the three single-layer and two double-layer electrode configurations in a FT-FF single-cell setup. The applied electrode compression ratio was maintained at ~20% in all cases. The non-linear Darcy-Forchheimer equation was used for fitting to the experimental pressure drop results, and the fitted results are shown in Fig. 3.3(b). The carbon paper exhibits extremely high pressure drop due to the high fiber density and low thickness. The permeability of the carbon paper is 3.2×10^{-11} m^2, which is lower than that of the carbon cloth (11.1×10^{-11} m^2 for AvCarb 1186 and 25.3×10^{-11} m^2 for ELAT-H). However, when coupled with a single layer of carbon cloth near the flow plate, the pressure drop of the DL configurations are greatly reduced. The permeability of A-FDL and E-FDL was found to be 10.7×10^{-11} m^2 and 14.9×10^{-11} m^2, respectively. It is noted that the permeability of A-FDL is similar to that of a single-layer AvCarb 1186. This indicates that within the A-FDL configuration, most electrolyte still flows through the carbon cloth layer despite the electrode compression, probably due to electrode thickness and the relatively large voids at the intersection between fiber bundles. In addition, it was also found that the AvCarb 1186 and A-FDL exhibit more obvious non-linear characteristics compared to the thinner ELAT-H, Freudenberg H23, and E-FDL within the measured range of the volumetric flow rate (i.e., 0-50 mL/min). Overall, the addition of carbon cloth has significant effects on reducing pressure drop compared to the single-layer carbon paper.

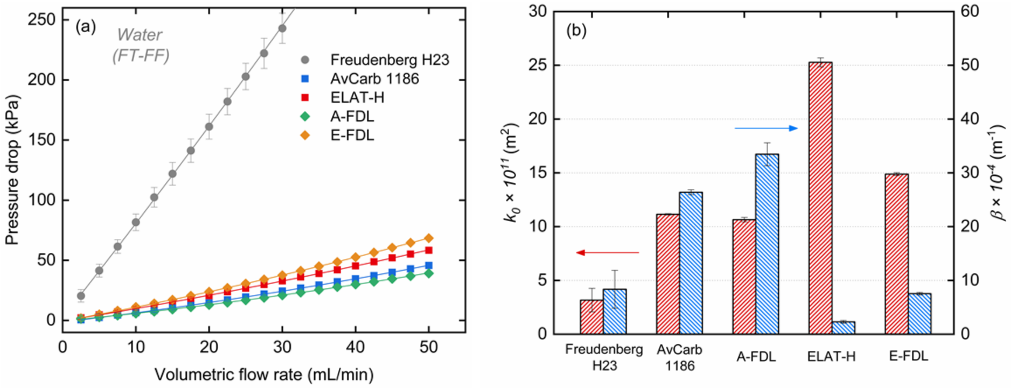

Figure 3.3 (a) Pressure drop (filled markers) versus volumetric flow rates for different electrode designs with the solvent of water under FT-FF flow patterns. The pressure drop of the empty cell without electrodes were subtracted. The best fit lines were obtained via non-linear least squares fitting of the non-linear Darcy-Forchheimer equation to the experimental data; (b) calculated permeability (red columns) and Forchheimer coefficient (blue columns) results from the fittings. The error bars correspond to a standard deviation (n=2).

3.4.2 Symmetrical cell testing and polarization analysis

The electrochemical performance of the DL electrode configurations was investigated in two separate symmetric cells. The measurements were conducted in both positive (i.e., VO^{2+}/VO_2^+) and negative (i.e., V^{2+}/V^{3+}) electrolytes, which represents the performance in relatively fast and sluggish redox couples, respectively. The performance of both redox couples is summarized in Fig. 3.4.

From EIS measurements at the same flow velocity (v_e=5 cm/s), we found that the carbon cloth electrodes exhibit a low mass transfer impedance. However, the performance is limited by high kinetic resistance due to the low active specific surface area, especially for the more sluggish redox couple (i.e., V^{2+}/V^{3+}). In contrast, the carbon paper possesses high surface area, and especially so after thermal treatment, which significantly contributes to the reduced kinetic resistance. However, the mass transport properties of carbon paper electrodes are relatively poor, yielding high pressure drop and high mass transfer resistance. For the two DL configurations, the overall resistances are both reduced compared to the single-layer of the carbon paper. Specifically, the total resistances of kinetic and mass transfer are reduced by ~40% and ~17% for A-FDL and E-FDL in V^{2+}/V^{3+} redox couples, respectively, compared to that of the carbon paper. The main reduction of the overall resistance came from the mass transfer process. When compared to the single-layer carbon cloth, the advantage of DL electrode configurations comes from the reduced kinetic resistance in both V^{2+}/V^{3+} and VO^{2+}/VO_2^+ redox couples. It proves that the DL electrode configurations effectively combine the benefits of the two types of electrodes, leading to improved electrochemical performance.

The iR-corrected polarization results for symmetric cells at a v_e of 5 cm/s are also presented in Fig. 3.4 including both V^{2+}/V^{3+} and VO^{2+}/VO_2^+ symmetric cells. In agreement with the EIS results, the DL configurations show lower overpotentials compared to the single-layer electrodes. A-FDL shows superior electrochemical performance with <0.1 V voltage loss in V^{2+}/V^{3+} symmetric cell at a current density of 500 mA/cm^2. This is also consistent with the low kinetic and mass transfer impedances observed for this dual layer electrode (A-FDL). It is noted that the overpotential of carbon paper increases rapidly at current densities greater than 400 mA/cm^2 in both V^{2+}/V^{3+} and VO^{2+}/VO_2^+ symmetric cells, which exhibits characteristics of mass transport limitations.

The above analysis puts the main emphasis on the impact of electrode configurations on the kinetic and mass transfer resistances, the ohmic resistance is subtracted in each case from the overall resistances. The ohmic resistance results in both V^{2+}/V^{3+} and VO^{2+}/VO_2^+ symmetric cells are summarized in Table 3.2. It is found that the additional layer in the DL configurations leads to the increased ohmic resistance, which is probably due to the additional contact resistance between the two layers and the ionic resistance from the increased electrode thickness. Although the added ohmic resistance of ~0.06 $\Omega\cdot$cm^2 in the DL configurations compared to the single-layer carbon cloth, the overall performance of the DL configurations is still promising due to the benefits from reduced kinetic and mass transfer resistances as well as low pressure drop.

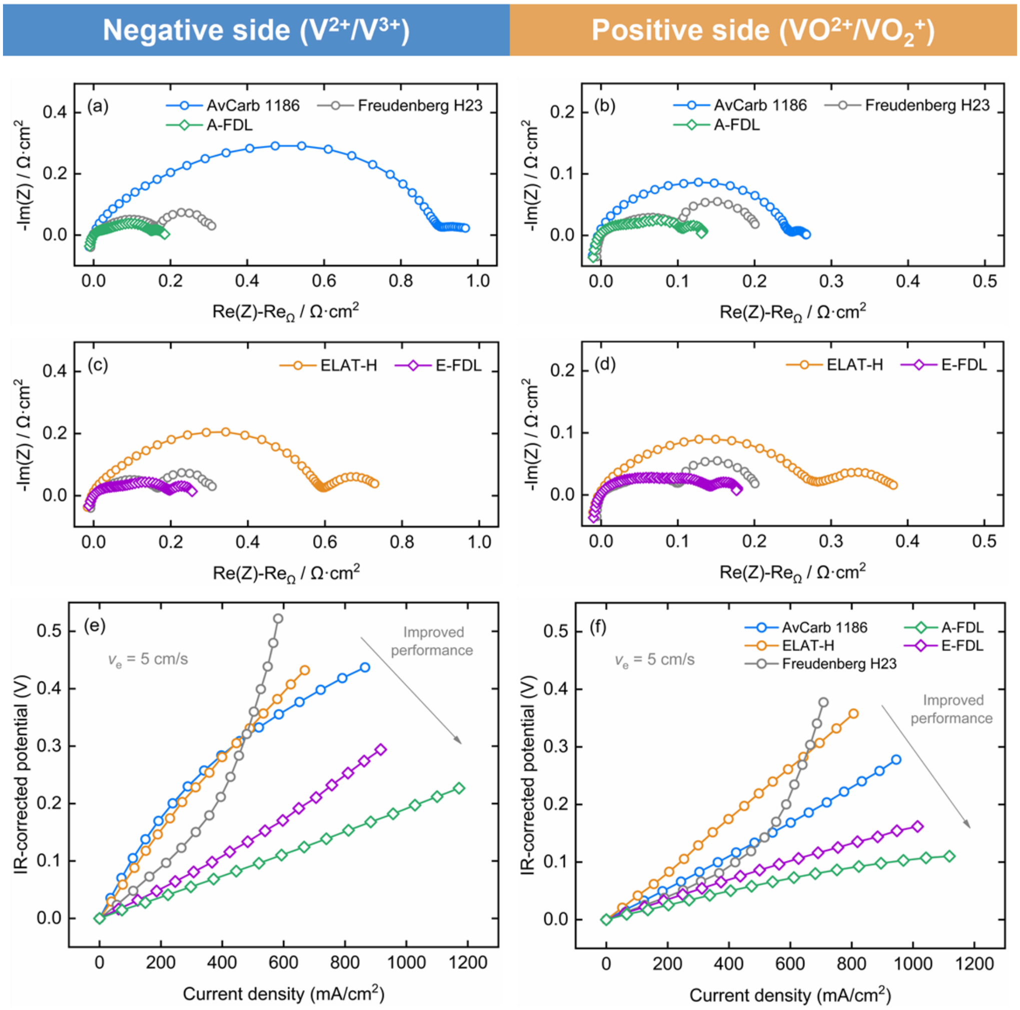

Figure 3.4 Electrochemical performance comparison between DL electrode configurations and single layer electrodes in both a negative and positive vanadium symmetric cell with 1.6 M V^{2+}/V^{3+} and VO^{2+}/VO_2^+, respectively. EIS spectra are shown in (a)-(d) and iR-corrected polarization curves are shown in (e)-(f). All the measurement were conducted at the electrolyte velocity of 5 cm/s.

To obtain the mass transfer coefficient of each electrode configuration, limiting current density measurements were conducted at five different flow rates in a single-tank positive symmetric cell with diluted electrolyte (0.1 mol/L VO^{2+}/VO_2^+). k_m can subsequently be obtained by fitting to the data as a function of flow velocity and the observed limiting current at different v_e. The results of the single-layer carbon cloth and the two DL electrode configurations are shown in Fig. 3.5. The two DL electrode configurations can reach higher current at low cell potential regions (i.e., at low overpotentials), compared to the single-layer carbon cloth. This is due to the reduced kinetic resistances through the carbon paper layer. However, when the current reaches the plateau at high cell potential, the limiting current densities of the A-FDL at different volumetric flow rate of the electrolytes were found to be lower than those of the AvCarb 1186. The mass transfer limiting current is influenced by the added carbon paper layer. Interestingly, for the E-FDL, the limiting current densities are higher compared to the single-layer ELAT-H at the volumetric flow rates of 10, 15, and 20 mL/min. Although the added carbon paper layer still has negative impacts on mass transfer process at low flow rates (i.e., 2.5 and 5 mL/min), it seems the mass transfer limitation is less likely to suffer a decrease at high flow rates. Therefore, the proportionality constant of k_m as a function of the superficial velocity is the highest (i.e., 0.97) for the E-FDL.

Table 3.2 Ohmic resistance from high-frequency region of EIS

Electrode	AvCarb 1186	ELAT-H	Freudenberg H23	A-FDL	E-FDL
Ohmic resistance ($\Omega\cdot cm^2$) in V^{2+}/V^{3+}	0.42	0.48	0.48	0.49	0.55
Ohmic resistance ($\Omega\cdot cm^2$) in VO^{2+}/VO_2^+	0.55	0.57	0.58	0.60	0.62

After obtaining k_m, the concentration overpotential can be calculated assuming zero concentration of active species at the fiber surface under limiting current conditions. The detailed calculations can be found in *Supplementary Information*. Hereby, the overall full-cell overpotential analysis was constructed on the basis of the measured mass transfer coefficient, and ohmic losses from high-frequency region of EIS. The activation overpotentials for V^{2+}/V^{3+} and VO^{2+}/VO_2^+ redox couples are calculated by subtracting concentration overpotentials and ohmic losses from the overall polarizations. After subtraction, the results are divided by 2 considering the same activation overpotential on both sides in a symmetric cell.

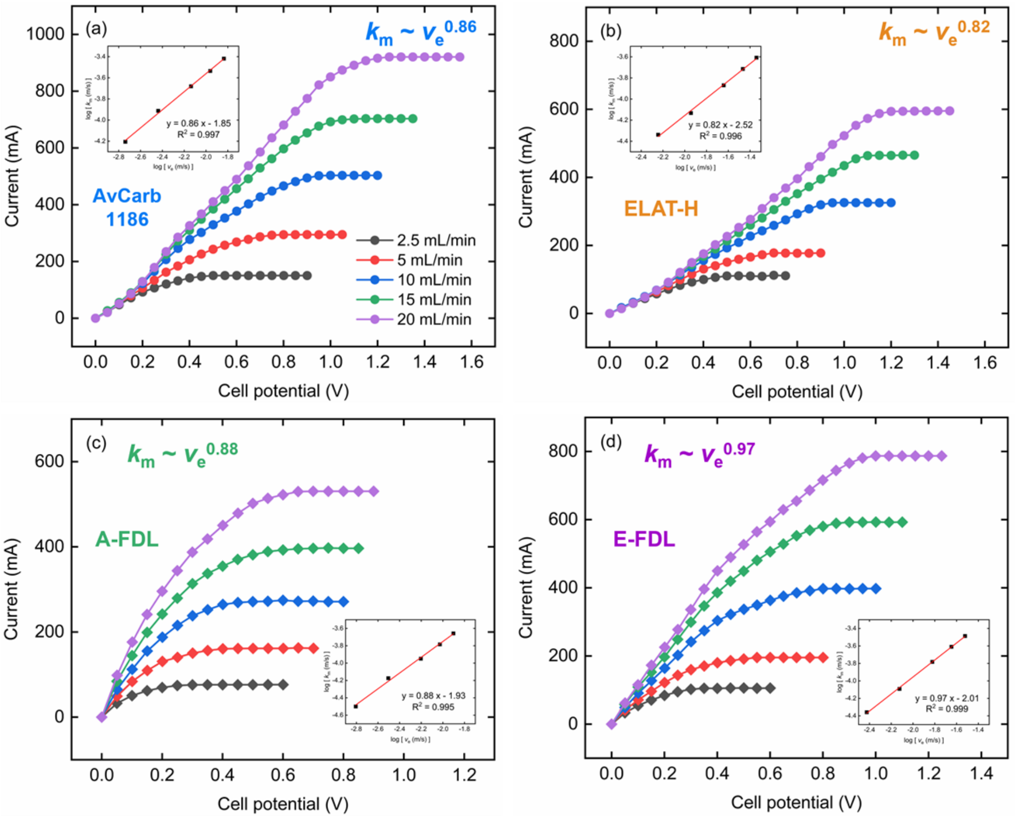

Figure 3.5 Limiting current density measurements in a diluted positive vanadium symmetric cell with 0.1 mol/L VO^{2+}/VO_2^+ for (a) AvCarb 1186, (b) ELAT-H, (c) A-FDL, and (d) E-FDL at 5 different volumetric flow rates. The limiting current density is extracted at the cell potential where the current reaches a plateau. The mass transfer coefficient (k_m) is fitted as a function of superficial electrolyte velocity (v_e) and the fitted proportionality constant of k_m is presented on the graph. Details of the calculation are shown in *Supplementary Information*.

The overall full-cell overpotential results are shown in Fig. 3.6. The three single-layer electrodes and two DL assemblies are compared in three cases with different applied current density and electrolyte flow rate. The results at a current density of 100 mA/cm^2 and at v_e=5 cm/s are shown in Fig. 3.6(a). We found that the high performance of DL configurations compared to the other three single-layer electrodes mainly arises due to a reduced activation overpotential of V^{2+}/V^{3+}, and also low concentration overpotential. Although the ohmic loss slightly increased due to the adoption of an additional electrode layer, the full-cell overall overpotential is still reduced by ~35% and ~30% for A-FDL and E-FDL, respectively, compared to the single-layer carbon cloth. At a higher current density of 300 mA/cm^2, the overall cell overpotential becomes higher, and the DL electrode configurations still maintain the best performance. When changing the flow velocity (v_e) of 1 cm/s at 300 mA/cm^2, it is assumed that the mass transport properties are only influenced through flow conditions and electrode structure, regardless of active redox couples. Hence, the activation overpotential and ohmic loss are expected to be independent of changes in flow rate. The cell overpotential results are shown in Fig. 3.6(c). Under such extreme conditions, the concentration overpotential of single-layer carbon paper becomes significant. The DL electrode configurations still exhibit promising electrochemical performance.

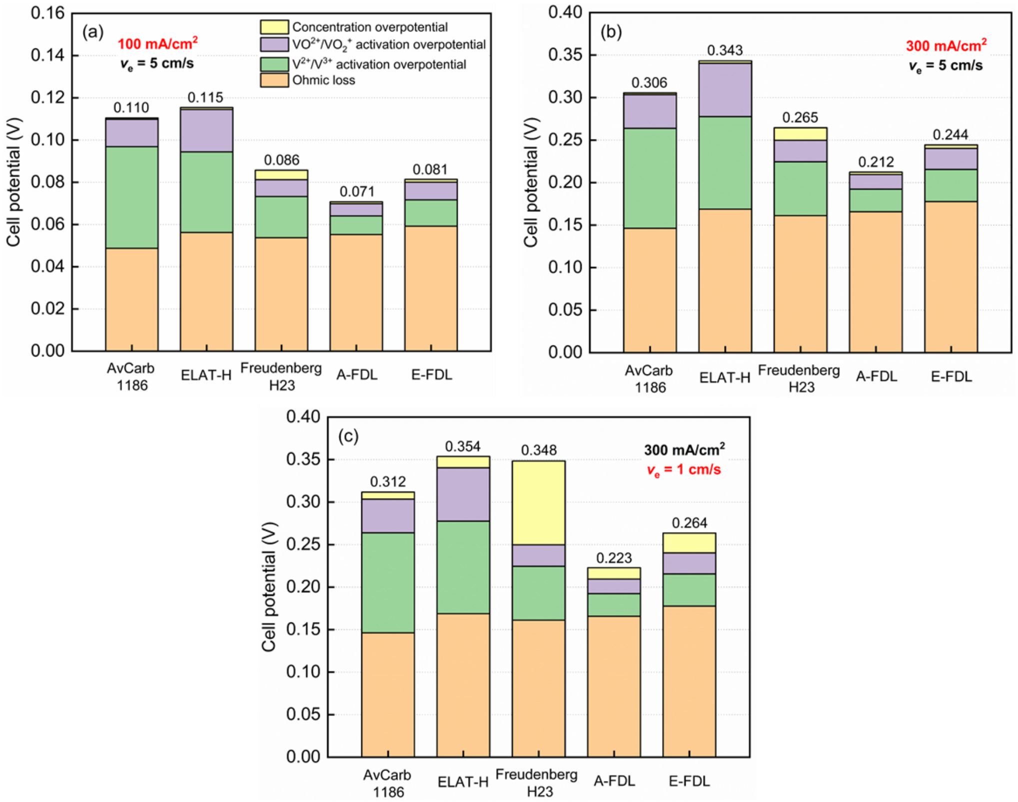

Figure 3.6 (a) Column analysis of the cell potential for comparison between DL electrode configurations and single layer electrodes at (a) 100 mA/cm^2 and v_e of 5 cm/s, (b) 300 mA/cm^2 and v_e of 5 cm/s, and (c) 300 mA/cm^2 and v_e of 1 cm/s.

3.4.3 Fiber orientation and flow distribution map

To better understand the impact of the electrode microstructure on the battery performance, fiber orientation analysis was conducted using a structure tensor method for each of the electrodes selected in the present study. A fiber orientation map under a DUO sphere colormap is presented on the raw X-ray CT image for each electrode. Representative through-plane slices of each electrode is shown in Fig. 3.7. The carbon cloth possesses two typical in-plane directions for different bundles of fibers. The sizes of the fiber bundles of AvCarb 1186 are larger than those of ELAT-H. For the carbon paper, we found that the internal fibers are not completely randomly distributed. Some closely contacted fibers are aligned in a particular direction, presenting a bunched stripe-like pattern. When collecting all information of the pre-dominant direction as points on a unit sphere for each electrode (see Fig. S3.3), it can be found that the fiber orientations for all the three electrodes are mostly distributed in the in-plane directions compared to the through-plane directions. The fiber orientations of the two carbon cloths are mainly in two directions, while the fiber orientations of the carbon paper are evenly distributed in all in-plane directions. Less fibers oriented in through-plane directions are expected to bring higher through-plane hydraulic permeability as compared to the in-plane directions. It is noted that the fiber orientation map presented here may introduce some additional orientation information from the pore regions, due to the noise around the neighborhood of the pore regions in raw X-ray CT images. A noise scale of 0.5 is selected in the present study and the orientation maps may vary slightly due to the changes in the selected noise scale.

To better understand the flow distribution in the DL electrode configuration, qualitative flow simulations using the LBM were conducted for the combination of a layer of ELAT-H carbon cloth and a layer of Freudenberg H23 carbon paper (i.e., E-FDL). The segmented X-ray CT image data is cropped and combined with the ELAT-H on top and Freudenberg H23 underneath, as shown in Fig. 3.8(a). The volume rendering of the velocity magnitude in Fig. 3.8(b) qualitatively shows that the flow velocity is greatest in the large channels of the carbon cloth while it is much lower in the carbon paper and within the fiber bundles of the cloth. Fig. 3.8(c) shows different slices of the normalized velocity magnitude along the flow direction. In all slices, the maximum velocity is observed in the middle of the cloth's channels, between the different bundles.

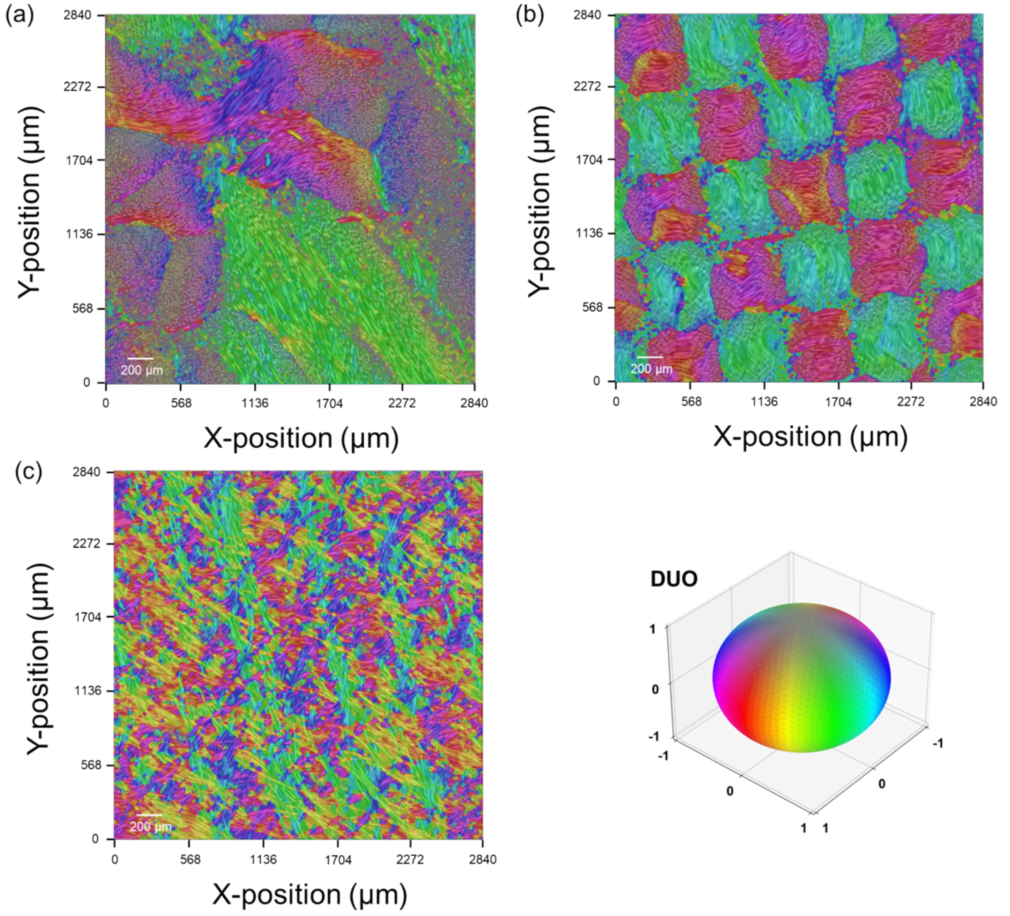

Figure 3.7 Through-plane slices of fiber orientation map for (a) AvCarb 1186, (b) ELAT-H, and (c) Freudenberg H23. The predominant orientation information is visualized as color with the overlay of raw X-ray CT images. Fan coloring (DUO in sphere colormap) is adopted to emphasize the orientation in XY plane, and the colormap is shown in the bottom right.

Note that the presented results are only qualitative. More effort is needed to carefully match the boundary conditions with practical experiments. Furthermore, a bigger volume should be simulated to avoid edge effects and be more representative of the real device. More quantitative simulations will be performed in a future study.

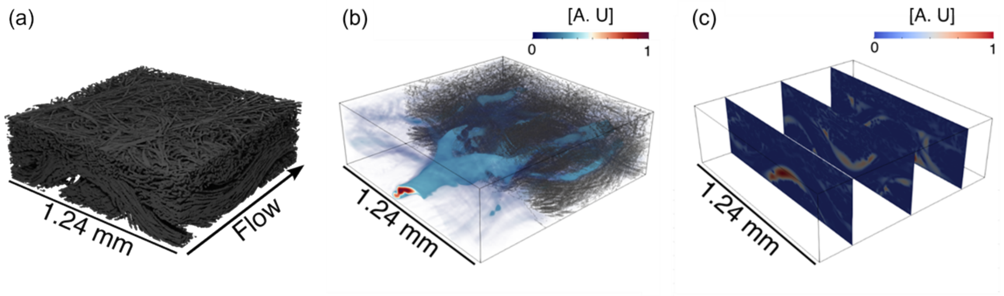

Figure 3.8 (a) Three-dimensional rendering of the constructed volume used for the flow simulations, showing the carbon cloth (ELAT-H) at the bottom and the carbon paper (Freudenberg H23) at the top. (b) Volume rendering of the normalized velocity magnitude in the DL configuration. In (b), values close to zero are presented in transparency. (c) Two-dimensional slices of the normalized velocity magnitude field, obtained along the flow direction. In both (b) and (c) the values are normalized using the maximum and minimum values of the computed velocity field.

3.4.4 Electrode imprint effects on thin-film membranes

After battery assembly, we found that the electrodes leave imprints on the surface of the 10-μm thick m-PBI membrane used in the present study. This is due to the applied compression ratio on the electrodes during battery assembly and the unevenness of the electrode surface, especially for the carbon cloth electrodes. Deep imprints may vary the membrane thickness in some regions under compression and increase the surface area, affecting the capacity decay process during long-term battery operation. In extreme cases, excessive compression may lead to membrane crack and battery failure. The adoption of a relatively flat carbon paper layer near the membrane is expected to function as a protection layer to the membrane.

To investigate the membrane surface morphology after battery assembly and the impacts of the electrode imprints on the battery performance, an optical profilometer is adopted to investigate the membrane surface morphology after battery compression. A comparison between the membrane assembled with ELAT-H and E-FDL electrodes is shown in Fig. 3.9. Each membrane was assembled with the selected electrode in a battery setup for >200 h at the compression ratio of 20% before morphology characterization. For comparison, the optical microscope images on both sides of the pristine m-PBI membrane and the 3D rending image are shown in Fig. S3.5 and Fig. S3.6, respectively. From Fig. S3.6, we can find that the pristine membrane surface is relatively flat before battery assembly. It is interesting that the 10-μm m-PBI membrane exhibits distinct morphologies on its two sides, with one side featuring spherical bumps. We speculate that the small bumps are caused by the casting process during the manufacturing of the m-PBI membrane on the side of the surface close to the air, which deserves further exploration.

From Fig. 3.9, it can be found that the ELAT-H carbon cloth leaves patterned imprints on the m-PBI membrane. In Fig. 3.9(a), the dark regions in the optical microscope image of ELAT-H assembled membrane represents area with low light intensity. These regions are areas with steep tilts that not enough light coming from, showing the high roughness of the membrane surface as a result of the imprints. Similarly, in the 3D topography maps of the membrane surface, it is observed that the membrane surface morphology is less affected by the assembly of the cloth electrode when there is a carbon paper layer placed adjacent to the membrane. The vacant areas in the images are not measured regions with not enough light intensity information. It is noted that the color ranges of the membrane topology exceed the membrane thickness (i.e., 10-μm in the present study). This is because the membrane inevitably curls to some extent during the measurements, even for the pristine sample as shown in Fig. S3.6. It does not reflect the thickness of the membrane itself. Although curled membrane observed in the ex-situ measurement, the regions receiving more stress which comes from the protruding part of the carbon cloth are expected to become thinner under battery compression.

To better understand the relationship between the imprints on membrane and the battery performance, we conducted self-discharge measurements in a full-cell vanadium RFB at the v_e of 2 cm/s with the initial cell potential at 1.6 V for both AvCarb 1186 and A-FDL, ELAT-H and E-FDL, respectively. It is noticed that there is no obvious difference of the capacity retention between the ELAT-H and E-FDL. However, there is a ~2% capacity discrepancy between the AvCarb 1186 and A-FDL after 150 h self-discharge process, proving that the negative effect of deep membrane imprints from electrodes with uneven surface (e.g., AvCarb 1186 carbon cloth) on the long-term operating battery stability.

Despite a carbon paper protection layer is placed adjacent to the membrane in A-DFL, we can still see the imprints of the AvCarb 1186 after battery assembly in the optical photographs, although it is greatly mitigated.

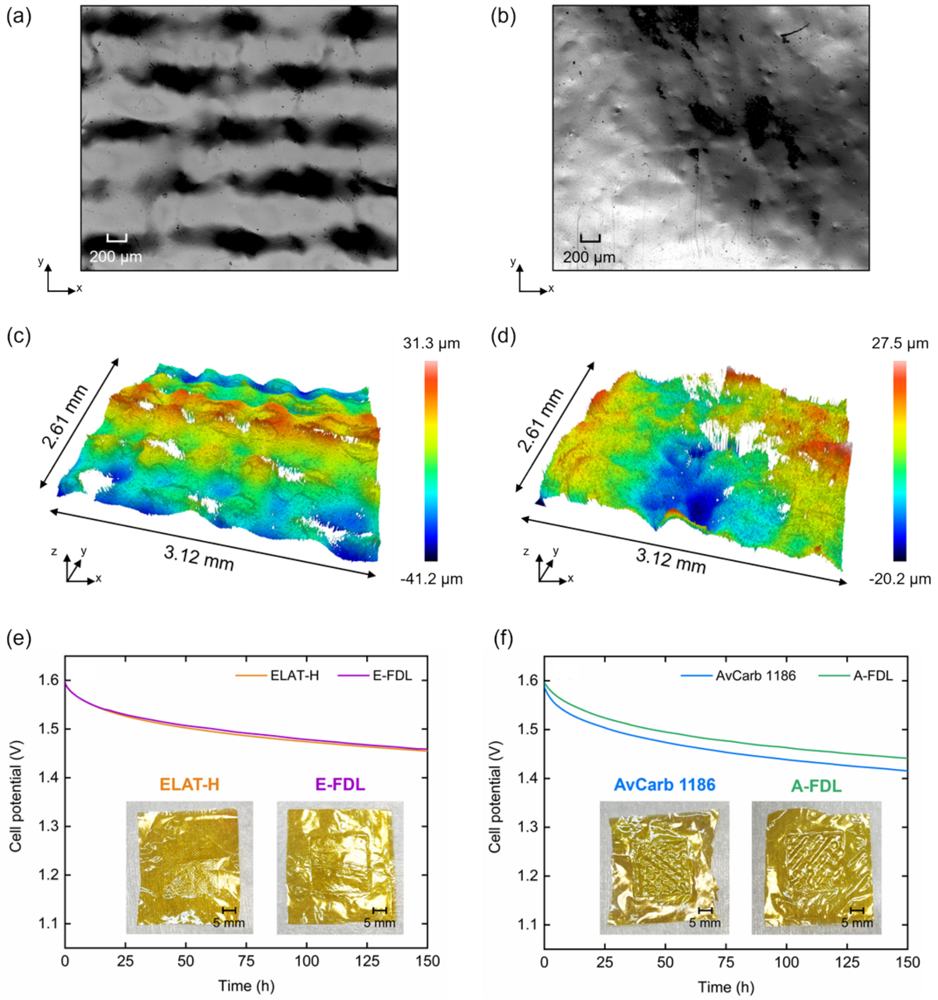

Figure 3.9 Bright filed optical microscope images of the m-PBI membrane after battery tests for >200 h with the combined electrode of (a) ELAT-H and (b) E-FDL. 2x2 stitched images are made to present the overall membrane surface information. The 3D topography maps of the membrane surface morphology are shown in (c) and (d), respectively. The self-discharge battery test results are shown in (e) and (f) with the v_e of 2 cm/s. Photographs of the four membranes are shown as insets in the graphs.

3.5 Discussions

3.5.1 Effects of the flow direction and electrode configuration

In the present study, we proposed a DL electrode configuration to investigate the feasibility of the carbon cloth as a simplified flow field. We notice that the woven structure of the carbon cloth has great impacts on the flow distribution and the electrochemical performance. Herein, we discuss the effects of the woven direction of the carbon cloth, and the effects of number of layers of the carbon cloth on the battery performance. The pressure drops and EIS results are shown in Fig. 3.10.

The carbon cloth electrodes are cut along the direction of 45^{o} rotation. Compared to the regularly cut carbon cloth electrodes, the pressure drop of both AvCarb 1186 and ELAT-H are elevated due to the more tortuous electrolyte flow pathways in the 45^{o} rotated carbon cloths. The pressure drop increase of the AvCarb 1186 is more obvious than that of the ELAT-H, due to the large bundle sizes of AvCarb 1186 may provide high flow resistance after rotation. Although the pressure drop is increased, the EIS results are quite similar for both single-layer carbon cloth and DL electrode configurations, which means the tortuous electrolyte flow does not bring a great benefit to the electrochemical mass transfer performance.

Secondly, we investigated the effects of number of layers of the carbon cloth electrodes. If the 2 layers of the carbon cloth are stacked together, the pressure drops are nearly a half of that of single-layer carbon cloth for both AvCarb 1186 and ELAT-H due to the doubled cross-sectional area. It also indicates that there is no big impact from the electrolyte flow between the two layers of the carbon cloth. For the EIS measurements, the additional layer of the carbon cloth brings extra surface area, which is effective to reduce the kinetic resistances. However, the increased ohmic resistances from the additional layer brings greater overall resistances compared to the single-layer carbon cloth. Herein, the DL electrode configurations present a better balance between kinetic and mass transfer resistances compared to double-layer carbon cloths. We also investigated EIS performance for multi-layer carbon paper, and the results are shown in Fig. S3.7. It is found that the ohmic resistance increased by an addition layer of the carbon paper electrode is not as obvious as that of the carbon cloth, which may be due to the extra contact resistance between the carbon cloth electrodes by the surface unevenness and less contact points of the carbon cloth.

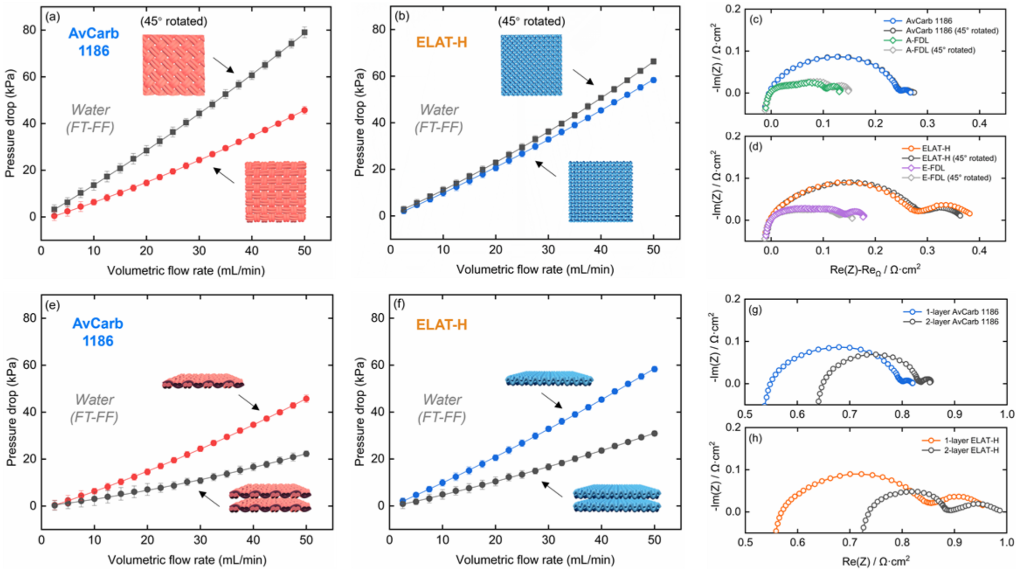

Figure 3.10 Effects of the (a-d) flow direction and (e-h) number of layers on pressure drop and electrochemical performance of the two carbon cloth electrodes. The pressure drop data (dots) is measured with the solvent of water under FT-FF, and the fittings (lines) are calculated according to the Darcy-Forchheimer equation. The EIS measurements are conducted in a positive vanadium symmetric cell with 1.6 mol/L VO^{2+}/VO_2^+ at the v_e of 5 cm/s. The error bars in pressure drop measurements correspond to a standard deviation (n=2).

3.5.2 Full-cell cycling tests

In order to comprehensively demonstrate the battery performance of the DL electrode configurations, the full-cell vanadium cycling tests were conducted to compare the single-layer carbon cloth and DL electrode configurations at varying current densities. The v_e is selected as 2 cm/s in each cycling test, and the results are shown in Fig. 3.11. Here, representative charge and discharge curves at each current density are presented, and the complete cycling results are shown in Fig. S3.8.

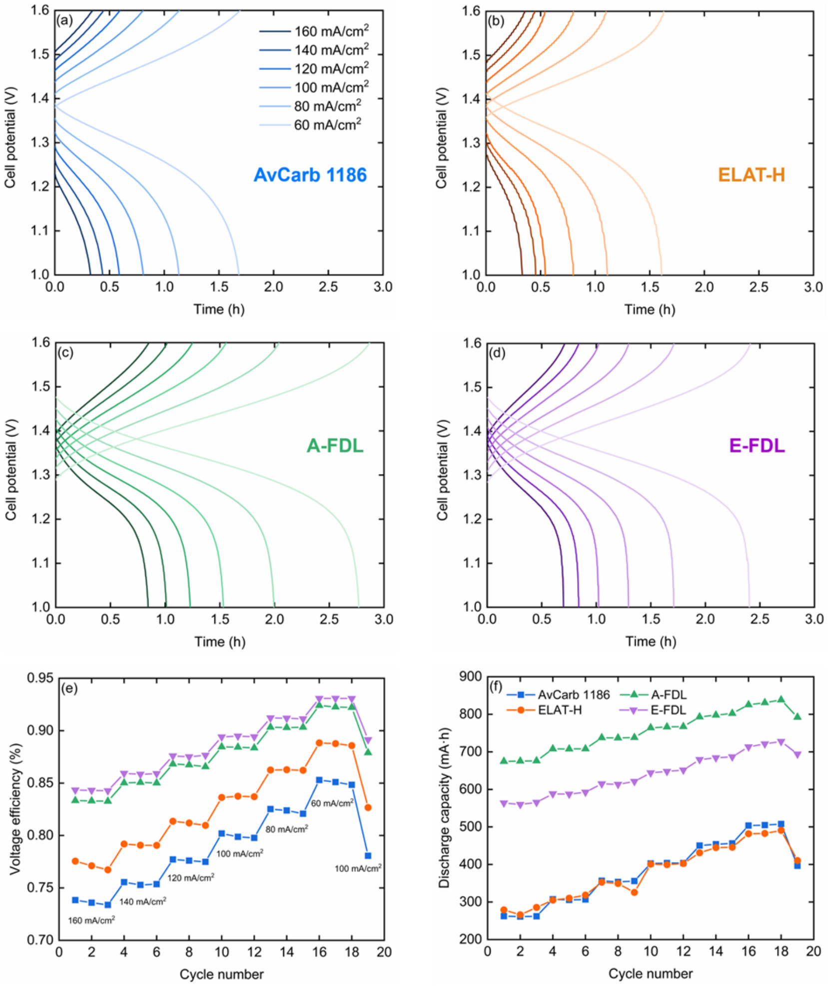

Figure 3.11 Full-cell vanadium charge-discharge cycling test results at varying current densities for (a) AvCarb 1186, (b) ELAT-H, (c) A-FDL, and (d) E-FDL. The second charge and discharge curves at each current density are presented. The voltage efficiency and discharge capacity of each electrode during the whole cycling tests are presented in (e) and (f), respectively. The v_e is selected as 2 cm/s in each cycling test.

In Fig. 3.11, it is evident that the performance of the single-layer AvCarb 1186 and ELAT-H carbon cloth electrodes is similar. Both of them are restricted in performance due to the low active specific surface area. However, the DL electrode configurations performs much better with higher voltage efficiency and discharge capacity. Specifically, the A-FDL and

E-EDL maintain ~90% of the voltage efficiency at 80 mA/cm^2, and the discharge capacity is almost doubled compared to that of the single-layer carbon cloth. The results show that the proposed strategy in the present study is an effective approach to boost battery performance while achieving low pressure drops.

3.6 Conclusions

In this work we investigated a dual-layer electrode configuration with the combination of carbon cloth and carbon paper. Due to the presence of hierarchical pore size distributions, carbon cloth is placed near the flow field to support high linear flow velocities at low pressure drop, which leads to efficient mass transfer of reactant to the sub-layer of carbon paper. Carbon paper is placed near the membrane to provide sufficient active sites for reactions due to the feature of high surface area. Compared to the single-layer electrode, the DL electrode configurations combines the advantages of the carbon cloth with low pressure drop and favorable mass transfer properties, and carbon paper with reduced kinetic resistance. In addition, the local flow distribution of the DL electrode configuration is simulated through LBM and it can be found that the flow velocity is higher within large channels of the carbon cloth. The carbon paper placed adjacent to the membrane plays a role as a protection layer to avoid deep electrode imprints on the 10-micron m-PBI membrane used in the present study. Overall, the proposed strategy has been proven to be effective to achieve low pressure drop and high full-cell electrochemical performance with the benefits mainly from a decrease of both the mass transport and kinetic overpotential of the V^{2+}/V^{3+} redox couple.

3.7 Supplementary Information

- **Compression effects on dual-layer electrode configurations**

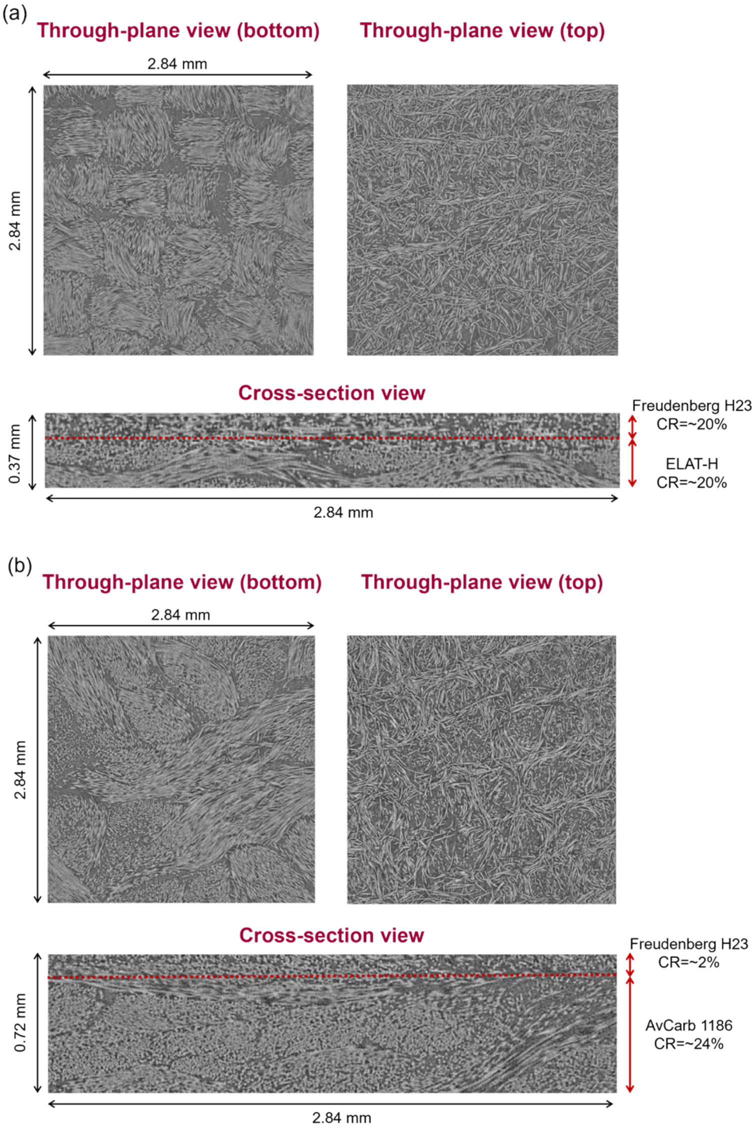

Figure S3.1 Through-plane and in-plane slices from X-ray μ-CT raw data for the compressed (a) E-FDL and (b) A-FDL in the present study. The overall applied compression ratio (CR) is 20% for each dual-layer configuration.

- **Calculattion of the k_m and concentration overpotential**

In order to gain insights into the mass transfer properties, limiting current density measurements were conducted in positive symmetric cell with diluted electrolyte (0.1 mol/L VO^{2+}/VO_2^{+}). The local mass transfer coefficient (k_m) is considered as a function of the superficial electrolyte flow rate (v_e), and can be estimated by the following equation:

$$k_m = a \times (v_e)^b \tag{S3.1}$$

where a and b denote empirical constants.

The a and b can be fitted after obtaining the limiting current density (i_L) at different volumetric flow rates. Specifically, 5 different volumetric flow rates (2.5, 5, 10, 15, and 20 mL/min) are applied for each electrode in the symmetric cell with diluted electrolyte. The limiting current is appropriately extracted at the point when the current reaches a plateau. After obtaining limiting currents, the k_m can be estimated by the following equation:

$$k_m = \frac{i_L}{nFc_r} \tag{S3.2}$$

where n denotes the electron transfer number (=1 in this study);
F denotes the Faraday constant;
c_r denotes the concentration of the active species (=0.05 mol/L in this study).

Hence, the a and b can be fitted by plotting $\log(k_m)$ as the function of $\log(v_e)$. Then, the concentration overpotential can be calculated at any superficial flow rate (v_e) by the following equation:

$$\eta_{con} = \left| \frac{RT}{F} \ln(1 - \frac{i}{nFc_r k_m}) \right| \tag{S3.3}$$

where R denotes the gas constant;
T denotes the temperature;
i denotes the applied current density.

A representative limiting current density result for Freudenberg H23 carbon paper is shown in Fig. S3.2. Here, k_m is fitted as 00014×$(v_e)^{0.72}$ in the symmetric cell.

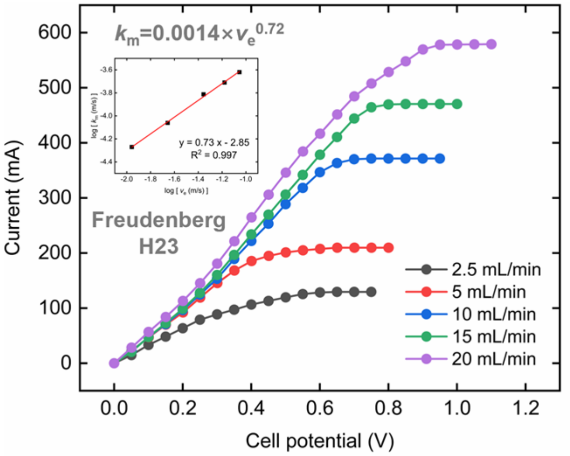

Figure S3.2 Limiting current density measurements in a symmetric cell with 0.1 M VO^{2+}/VO_2^+ for single layer Freudenberg H23 carbon paper at different volumetric flow rates. The mass transfer coefficient (k_m) is fitted as a function of superficial electrolyte velocity (v_e) and the fitted proportionality constant of k_m is presented on the graph.

- **Fiber orientation analysis**

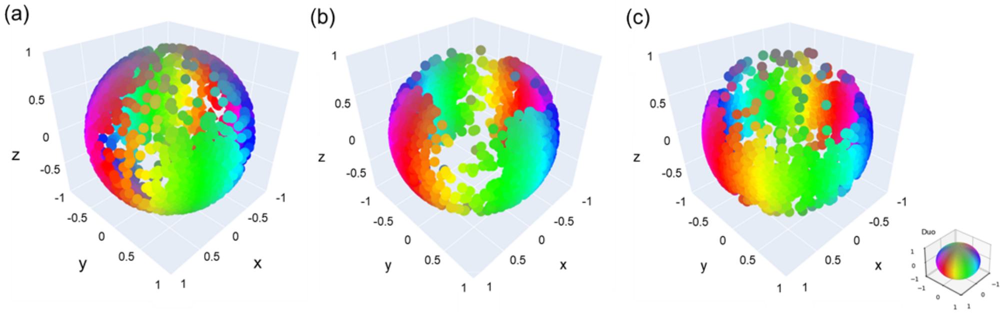

Figure S3.3 Visualization of dominant fiber orientations for (a) AvCarb 1186, (b) ELAT-H, and (c) Freudenberg H23 as points on a unit sphere. Fan coloring (DUO in sphere colormap) is adopted, which is shown in bottom right corner.

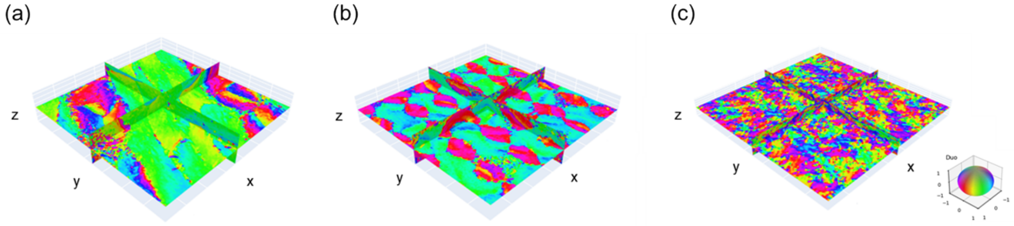

Figure S3.4 Representative through-plane and in-plane slices of fiber orientation maps for (a) AvCarb 1186, (b) ELAT-H, and (c) Freudenberg H23. Fan coloring (DUO in sphere colormap) is adopted, which is shown in bottom right corner.

- **Electrode Imprints on membrane**

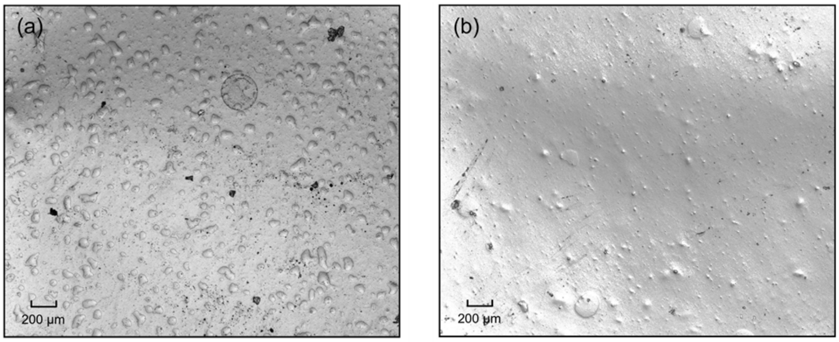

Figure S3.5 Bright filed optical microscope images of the pristine m-PBI membrane on both sides. 2x2 stitched images are made to present the overall membrane surface information.

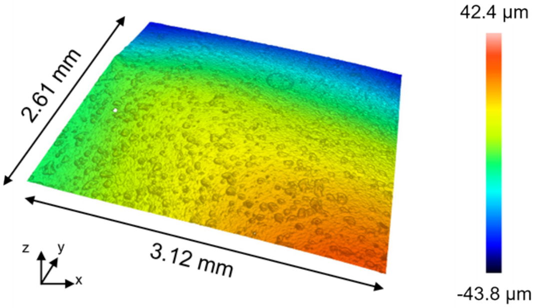

Figure S3.6 3D topography maps of the pristine m-PBI membrane surface morphology.

- **Effects of number of layers of carbon paper on electrochemical performance**

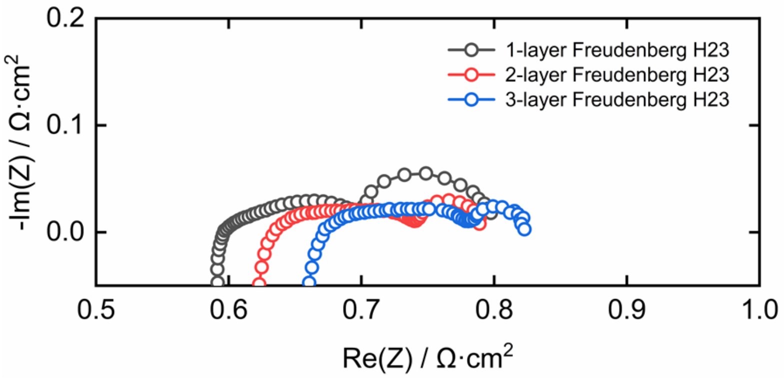

Figure S3.7 Effects of number of layers of Freudenberg H23 carbon paper on electrochemical performance. The EIS measurements are conducted in a positive vanadium symmetric cell with 1.6 M VO^{2+}/VO_2^+ at the v_e of 5 cm/s.

Table S3.1 Ohmic resistance from high-frequency region of EIS after removal inductance

Electrode	1-layer	2-layer	3-layer	4-layer	5-layer
Ohmic resistance ($\Omega\cdot cm^2$) in VO^{2+}/VO_2^+	0.58	0.62	0.66	0.69	0.71

- **Cycling tests**

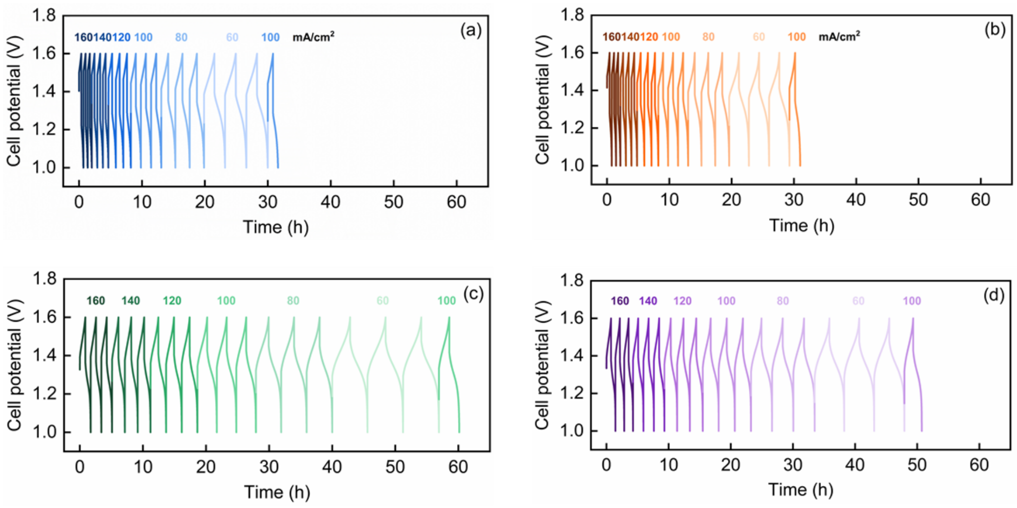

Figure S3.8 Overall full-cell vanadium charge-discharge cycling tests results for (a) AvCarb 1186, (b) ELAT-H, (c) A-FDL, and (d) E-FDL.

References

[1] M. Rahman, A. Oni, E. Gemechu, A. Kumar. Assessment of energy storage technologies: A review. *Energy Conversion and Management*, 223, 113295 (2020).

[2] Y. Yao, J. Lei, Y. Shi, F. Ai, Y. Lu. Assessment methods and performance metrics for redox flow batteries. *Nature Energy*, 6, 582−588 (2021).

[3] B. Dunn, H. Kamath, J. Tarascon. Electrical energy storage for the grid: a battery of choices. *Science*, 334, 928−935 (2011).

[4] K. Lin, Q. Chen, M. Gerhardt, L. Tong, S. Kim, L. Eisenach, A. Valle, D. Hardee, R. Gordon, M. Aziz, M. Marsha. Alkaline quinone flow battery. *Science*, 349, 1529−1532 (2015).

[5] R. Fornari, M. Mesta, J. Hjelm, T. Vegge, P. Silva. Molecular engineering strategies for symmetric aqueous organic redox flow batteries. *ACS Materials Letters*, 7, 239−246 (2020).

[6] A. Pasadakis-Kavounis, F. Arslan, M. Almind, D. Aili, J. Hjelm. Tuning polybenzimidazole-derived crosslinked interpenetrating network membranes for vanadium redox flow batteries. *Batteries & Supercaps*, 6, e20230017 (2023).

[7] Z. Yuan, Y. Duan, H. Zhang, X. Li, H. Zhang, I. Vankelecomd. Advanced porous membranes with ultra-high selectivity and stability for vanadium flow batteries. *Energy & Environmental Science*, 9, 441−447 (2016).

[8] C. Wan, R. Jacquemond, Y. Chiang, K. Nijmeijer, F. Brushett, A. Forner-Cuenca. Non-Solvent induced phase separation enables designer redox flow battery Electrodes. *Advanced Materials*, 33, 2006716 (2021).

[9] C. Wan, D. Barreiro, A. Forner-Cuenca, J. Barotta, M. Hawker, G. Han, H. Loh, A. Masic, D. Kaplan, Y. Chiang, F. Brushett, F. Martin-Martinez, M. Buehler. Exploration of biomass-derived activated carbons for use in vanadium redox flow batteries. *ACS Sustainable Chemistry & Engineering*, 8, 9472−9482 (2020).

[10] J. Noack, L. Wietschel, N. Roznyatovskaya, K. Pinkwart, J. Tübke. Techno-economic modeling and analysis of redox flow battery systems. *Energies*, 9, 627 (2016).

[11] R. Wang, Y. Li. Carbon electrodes improving electrochemical activity and enhancing mass and charge transports in aqueous flow battery: Status and perspective. *Energy Storage Materials*, 31, 230−251 (2020).

[12] Z. Zhang, J. Xi, H. Zhou, X. Qiu. KOH etched graphite felt with improved wettability and activity for vanadium flow batteries. *Electrochimica Acta*, 218, 15−23 (2016).

[13] R. Banerjee, N. Bevilacqua, A. Mohseninia, B. Wiedemann, F. Wilhelm, J. Scholta, R. Zeis. Carbon felt electrodes for redox flow battery: Impact of compression on transport properties. *Journal of Energy Storage*, 26, 100997 (2019).

[14] K. Greco, J. Bonesteel, N. Chanut, C. Wan, Y. Chiang, F. Brushett. Limited Accessibility to Surface Area Generated by Thermal Pretreatment of Electrodes Reduces Its Impact on Redox Flow Battery Performance. *ACS Applied Energy Materials*, 4, 13516−13527 (2021).

[15] Saleem Abbas, Sheeraz Mehboob, Hyun-Jin Shin, Oc Hee Han, Heung Yong Ha. Highly functionalized nanoporous thin carbon paper electrodes for high energy density of zero-gap vanadium redox flow battery. *Chemical Engineering Journal*, 378, 122190 (2019).

[16] A. Forner-Cuenca, F. Brushett. Engineering porous electrodes for next-generation redox flow batteries: recent progress and opportunities. *Current Opinion in Electrochemistry*, 18, 113−122 (2019).

[17] H. Jiang, Y. Zeng, M. Wu, W. Shyy, T. Zhao. A uniformly distributed bismuth nanoparticle-modified carbon cloth electrode for vanadium redox flow batteries. *Applied Energy*, 240, 226−235.

[18] K. Greco, A. Forner-Cuenca, A. Mularczyk, J. Eller, F. Brushett. Elucidating the nuanced effects of thermal pretreatment on carbon paper electrodes for vanadium redox flow batteries. *ACS Applied Materials & Interface*, 10, 44430−44442 (2018).

[19] X. Zhou, T. Zhao, Y. Zeng, L. An, L. Wei. A highly permeable and enhanced surface area carbon-cloth electrode for vanadium redox flow batteries. *Journal of Power Sources*, 329, 247−254 (2016).

[20] Y. Zhao, L. Yu, X. Qiu, J. Xi. Carbon layer-confined sphere/fiber hierarchical electrodes for efficient and durable vanadium flow batteries. *Journal of Power Sources*, 402, 453–459 (2018).

[21] E. Boz, P. Boillat, A. Forner-Cuenca. Taurine electrografting onto porous electrodes improves redox flow battery performance. *ACS Applied Materials & Interfaces*, 14, 41883–41895 (2022)

[22] J. Sun, M. Wu, H. Jiang, X. Fan, T. Zhao. Advances in the design and fabrication of high-performance flow battery electrodes for renewable energy storage. *Advances in Applied Energy*, 2, 100016 (2021).

[23] L. Arenas, C. León, F. Walsh. A critical review—the versatile plane parallel electrode geometry: an illustrated review. *Journal of The Electrochemical Society*, 167, 023504 (2020).

[24] Q. Xu, T. Zhao, P. Leung. Numerical investigations of flow field designs for vanadium redox flow batteries. *Applied Energy*, 105, 47–56 (2013).

[25] J. Sun, B. Liu, M. Zheng, Y. Luo, Z. Yu. Serpentine flow field with changing rib width for enhancing electrolyte penetration uniformity in redox flow batteries. *Journal of Energy Storage*, 49, 104135 (2022).

[26] Y. Zhang, F. Li, F. Lu, X. Zhou, Y. Yuan, X. Cao, B. Xiang. A hierarchical interdigitated flow field design for scale-up of high-performance redox flow batteries. *Applied Energy*, 238, 435–441 (2019).

[27] J. Sun, M. Zheng, Z. Yang, Z. Yu. Flow field design pathways from lab-scale toward large-scale flow batteries. *Energy*, 1173, 637–646 (2019).

[28] X. Ke, J. Prahl, J. Alexander, J. Wainright, T. Zawodzinski, R. Savinell. Rechargeable redox flow batteries: flow fields, stacks and design considerations. *Chemical Society Reviews*, 47, 8721–8743 (2018).

[29] V. Muñoz-Perales, P. García-Salaberri, A. Mularczyk, S. Ibáñez, M. Vera, A. Forner-Cuenca, *ChemRxiv* (2023), https://doi.org/10.26434/chemrxiv-2023-2zthc.

[30] R. Gundlapalli, S. Jayanti. Effect of channel dimensions of serpentine flow fields on the performance of a vanadium redox flow battery. *Journal of Energy Storage*, 23, 148–158 (2019).

[31] M. Gerhardt, A. Wong, M. Aziz. The effect of interdigitated channel and land dimensions on flow cell performance. *Journal of The Electrochemical Society*, 165, A2625–A2643 (2018).

[32] V. Muñoz-Perales, M. Heijden, P. García-Salaberri, M. Vera, A. Forner-Cuenca. Engineering lung-inspired flow field geometries for electrochemical flow cells with stereolithography 3D printing. *ACS Sustainable Chemistry & Engineering*, (2023).

[33] J. Sun, M. Zheng, Y. Luo, Z. Yu. Three-dimensional detached serpentine flow field design for redox flow batteries. *Journal of Power Sources*, 428, 136–145 (2019).

[34] A. Forner-Cuenca, E. Penn, A. Oliveira, F. Brushett. Exploring the role of electrode microstructure on the performance of non-aqueous redox flow batteries. *Journal of The Electrochemical Society*, 166, A2230–A2241 (2019).

[35] L. Baumgartner, C. Koopman, A. Forner-Cuenca, D. Vermaas. When flooding is not catastrophic—woven gas diffusion electrodes enable stable CO_2 electrolysis. *ACS Applied Energy Materials*, 5, 15125–15135 (2022).

[36] M. León, L. Castañeda, A. Márquez, F. Walsh, J. Nava. Review—carbon cloth as a versatile electrode: manufacture, properties, reaction environment, and applications. *Journal of The Electrochemical Society*, 169, 053503 (2022).

[37] A. Wong, M. Aziz. Method for Comparing porous carbon electrode performance in redox flow batteries. *Journal of The Electrochemical Society*, 167, 110542 (2020).

[38] K. Tenny, A. Forner-Cuenca, Y. Chiang, F. Brushett. Comparing physical and electrochemical properties of different weave patterns for carbon cloth electrodes in

redox flow batteries. *Journal of Electrochemical Energy Conversion and Storage*, 17, 041010 (2020).

[39] O. Esan, X. Shi, Z. Pan, X. Huo, L. An, T. Zhao. Modeling and simulation of flow batteries. *Advanced Energy Materials*, 10, 2000758 (2020).

[40] D. Zhang, A. Forner-Cuenca, O. Taiwo, V. Yufit, F. Brushett, N. Brandon, S. Gu, Q. Cai. Understanding the role of the porous electrode microstructure in redox flow battery performance using an experimentally validated 3D pore-scale lattice Boltzmann model. *Journal of Power Sources*, 447, 227249 (2020).

[41] M. Heijden, R. Gorp, M. Sadeghi, J. Gostick, A. Forner-Cuenca. Assessing the versatility and robustness of pore network modeling to simulate redox flow battery electrode performance. *Journal of The Electrochemical Society*, 169, 040505 (2022).

[42] Y. Luo, W. Lv, M. Zheng. A multi-scale model for local polarization prediction in flow batteries based on deep neural network. *Journal of Energy Storage*, 68, 107842 (2023)

[43] C. Zeng, S. Kim, Y. Chen, Y. Fu, J. Bao, Z. Xu, W. Wang. Characterization of electrochemical behavior for aqueous organic redox flow batteries. *Journal of The Electrochemical Society*, 169, 120527 (2022).

[44] M. Manahan, Q. Liu, M. Gross, M. Mench. Carbon nanoporous layer for reaction location management and performance enhancement in all-vanadium redox flow batteries. *Journal of Power Sources*, 222, 498–502 (2013).

[45] W. Chen, J. Kang, Q. Shu, Y. Zhang. Analysis of storage capacity and energy conversion on the performance of gradient and double-layered porous electrode in all vanadium redox flow batteries. *Energy*, 180, 341–355 (2019).

[46] Q. Ma, W. Fu, L. Zhao, Z. Chen, H. Su, Q. Xu. A double-layer electrode for the negative side of deep eutectic solvent electrolyte-based vanadium-iron redox flow battery. *Energy*, 265, 126291 (2023).

[47] Q. Ma, C. Mao, L. Zhao, Z. Chen, H. Su, Q. Xu. A pore-scale study for reactive transport processes in double-layer gradient electrode as negative side of a deep eutectic solvent electrolyte-based vanadium-iron redox flow battery. *Electrochimica Acta*, 431, 141110 (2022).

[48] M. Raja, H. Khan, S. Sankarasubramanian, D. Sonawat, V. Ramani, K. Ramanujam. Binder-free thin graphite fiber mat sandwich electrode architectures for energy-efficient vanadium redox flow batteries. *Catalysis Today*, 370, 181–188 (2021).

[49] H. Jiang, B. Zhang, J. Sun, X. Fan, W. Shyy, T. Zhao. A gradient porous electrode with balanced transport properties and active surface areas for vanadium redox flow batteries. *Journal of Power Sources*, 440, 227159 (2019).

[50] Y. Kima, Y. Choi, N. Yun, M. Yang, Y. Jeon, K. Kim, J. Choi. Activity gradient carbon felt electrodes for vanadium redox flow batteries. *Journal of Power Sources*, 408, 128–135 (2018).

[51] R. Cheng, J. Xu, J. Zhang, P. Leung, Q. Ma, H. Su, W. Yang, Q. Xu. Facile segmented graphite felt electrode for iron-vanadium redox flow batteries with deep eutectic solvent (DES) electrolyte. *Journal of Power Sources*, 483, 229200 (2021).

[52] W. Wang, X. Wang. Investigation of Ir-modified carbon felt as the positive electrode of an all-vanadium redox flow battery. *Electrochimica Acta*, 52, 6755–6762 (2007).

[53] P. Mazur, J. Mrlik, J. Pocedic, J. Vrana, J. Dundalek, J. Kosek, T. Bystron. Effect of graphite felt properties on the long-term durability of negative electrode in vanadium redox flow battery. *Journal of Power Sources*, 414, 354–365 (2019).

[54] Q. Wu, Y. Lv, L. Lin, X. Zhang, Y. Liu, X. Zhou. An improved thin-film electrode for vanadium redox flow batteries enabled by a dual layered structure. *Journal of Power Sources*, 410–411, 152–161 (2019).

[55] Y. Li, Q. Wen, J. Qin, S. Zou, F. Ning, C. Bai, S. Pan, H. Jin, P. Xu, M. Shen, Y. Song, X. Zhou. A high-efficient and low-consumption nanoimprint method to prepare large-area and high-quality Nafion array for the ordered MEA of fuel cell. *Chemical Engineering Journal*, 451, 138722 (2023).

[56] L. Wan, M. Pang, J. Le, Z. Xu, H. Zhou, Q. Xu, B. Wang. Oriented intergrowth of the catalyst layer in membrane electrode assembly for alkaline water electrolysis. *Nature Communications*, 13, 7956 (2022).

[57] X. Zhou, T. Zhao, L. An, Y. Zeng, L. Wei. Critical transport issues for improving the performance of aqueous redox flow batteries. *Journal of Power Sources*, 339, 1–12 (2017).

[58] M. Lu, W. Yang, X. Bai, Y. Deng, Y. He. Performance improvement of a vanadium redox flow battery with asymmetric electrode designs. *Electrochimica Acta*, 319, 210–226 (2019).

[59] N. Jeppesen, L. Mikkelsen, A. Dahl, A. Christensen, V. Dahl. Quantifying effects of manufacturing methods on fiber orientation in unidirectional composites using structure tensor analysis. *Composites: Part A*, 149, 106541 (2021).

[60] N. Jeppesen, V. Dahl, A. Christensen, A. Dahl, L. Mikkelsen. Characterization of the fiber orientations in non-crimp glass fiber reinforced composites using structure tensor. *IOP Conference Series: Materials Science and Engineering*, 942, 012037 (2020).

[61] J. Latt, O. Malaspinas, D. Kontaxakis, A. Parmigiani, D. Lagrava, F. Brogi, M. Belgacem, Y. Thorimbert, S. Leclaire, S. Li, F. Marson, J. Lemus, C. Kotsalos, R. Conradin, C. Coreixas, R. Petkantchin, F. Raynaud, J. Beny, B. Chopard. Palabos: Parallel Lattice Boltzmann Solver. *Computers & Mathematics with Applications*, 81, 334–350 (2021).

Chapter 4

Integrating Micro-flow Fields into Electrode Architecture via Non-solvent Induced Phase Separation for High Performance Redox Flow Batteries

Baichen Liu[a,b], Vanesa Muñoz[c], Simona Buzzi[b], Rémy Richard Jacquemond[b], Johan Hjelm[a], Antoni Forner-Cuenca[b*]

[a] Department of Energy Conversion and Storage, Technical University of Denmark, Building 310, DK-2800 Kgs. Lyngby, Denmark
[b] Department of Chemical Engineering and Chemistry, Eindhoven University of Technology, 5600 MB Eindhoven, The Netherlands
[c] Departamento de Ingeniería Térmica y de Fluidos, Universidad Carlos III de Madrid, 28911, Leganés, Spain

[*] Corresponding author: a.forner.cuenca@tue.nl

Abstract

Non-solvent induced phase separation (NIPS) is a manufacturing route in the field of membrane technology, which is widely used to fabricate asymmetric membranes. Recently this route has also been used to fabricate non-fibrous porous electrodes. In the present study, inspired by the flow field designs widely used in RFBs to guide the electrolyte flow paths for low pressure drop, uniform electrolyte distribution, and high electrochemical performance, we propose a strategy to imprint micro-patterned flow fields directly into the electrode architecture during NIPS processing to improve mass transfer properties. To verify the effectiveness of the micro-patterned electrodes, here, we investigated two selected micro-pattern designs. The groove-patterned electrodes were combined with flow-through flow fields (FTFFs) for in-plane mass transport optimization, and the pillar-

patterned electrodes were combined with interdigitated flow fields (IDFFs) for through-plane flow optimizations. It was found that the pillar-patterned electrodes with the combination of interdigitated flow field presented high overall electrochemical performance with greatly reduced mass transport resistances. At an electrolyte velocity of 10 cm/s, the total resistances for kinetic and mass transfer were less than 0.1 $\Omega\cdot\mathrm{cm}^2$ in symmetric iron cell tests, which shows great potential for adoption in next generation high-performance RFB systems.

4.1 Introduction

To facilitate increasing penetration of intermittent renewables in the energy mix, there is a growing need for energy storage technologies. Redox flow batteries (RFBs) have attracted significant attention in recent years due to their suitable characteristics for long-duration stationary energy storage applications. However, the wider adoption of RFB systems is still limited by the capital cost [1], to which the reactor stack is a large contributor [2]. Further cost reduction can be achieved by reducing kinetic, mass-transfer, and ohmic losses to improve the stack performance. Porous electrodes are key components within the battery stack, providing active sites for electrochemical reactions, and transport pathways for active species [3]. Commercially available carbon-fiber electrode architectures include carbon paper, carbon felt, and carbon cloth [4]. They have a highly porous structure, but their relatively low surface area and low hierarchical fiber orientation increase both electrochemical and pumping losses. There is still a need to develop a low-cost porous electrode that meets the requirements of high active surface area and facile electrolyte transport to enhance battery performance and system efficiency.

In membrane technology, the NIPS method is widely adopted to produce asymmetric membranes [5]. This technique has now been adapted to prepare non-fibrous porous electrodes through an additional carbonization process [9]. The microstructure of NIPS electrodes is largely influenced and controlled by the solvent/non-solvent exchange rate at the interface between a polymer solution and a coagulation bath [10]. If the phase exchange process is fast, instantaneous demixing will happen. A solid film is formed very rapidly after immersion in the non-solvent bath. This type of demixing generally shows a highly porous, finger-shaped, macrovoid structure [11]. Due to the presence of the macrovoid pores, this structure can provide low pressure drop and good mass transport properties, but relatively low surface area. When the phase exchange process is slow, segregation is delayed. This type of segregation generally results in a sponge-like, relatively dense structure [12]. This sponge-like structure has the advantage of small pore size and high surface area, but also has poor hydraulic permeability and high mass-transfer losses. The trade-off between surface area and permeability needs to be further optimized.

In flow battery single cell designs, the flow plates are often engraved with flow field designs and placed in contact with the electrode on each side of the battery [13]. Typical flow field designs used in flow batteries include serpentine flow fields (SFF) [14] and interdigitated flow fields (IDFF) [15]. The presence of the flow fields can force the electrolyte flow in specific pathways in flow-by and flow-through configurations. Compared to the flow-through designs without flow fields, it shows lower pressure drop, more uniform electrolyte distributions, and better electrochemical performance. In the present study, inspired by the flow field designs on flow plates, we propose a strategy to directly integrate the micro-flow fields into the electrode architecture during the NIPS process, aiming to enhance mass transfer properties of the sponge-like NIPS structure. NIPS polymer films were cast onto molds with specific micro-patterns, and the resulting micro-channels can be preserved in the electrodes after carbonization. the fabrication process is shown in Fig. 4.1. To verify the effectiveness of the micro-patterned electrodes, we investigated two selected micro-patterned designs. We combined the groove-patterned electrodes with flow-through flow fields (FTFFs) to facilitate in-plane mass transfer, while the pillar-patterned electrodes were paired with interdigitated flow fields (IDFFs) for through-plane flow within the rib region. Two geometric sizes of the micro-patterns were considered in each design. The pore sizes and distributions of the micro-patterned electrodes were determined by mercury intrusion porosimetry. The hydraulic permeability of the electrodes was evaluated by half-cell pressure drop measurements, and the electrochemical specific surface area was determined through electrochemical impedance spectroscopy under non-faradaic conditions. In addition, we performed electrochemical battery tests with symmetric iron flow cells (0.5 mol/L Fe^{2+}/Fe^{3+}, 2 M HCl) cells and vanadium full-cells (1.6 mol/L vanadium active species at 50% state-of-charge). It was found that due to the small pore size (e.g., ~1 μm) and narrow pore size distribution of the sponge-like NIPS structure, the main contribution to the total losses in electrodes without micro-patterns in electrochemical performance comes from mass-transfer.

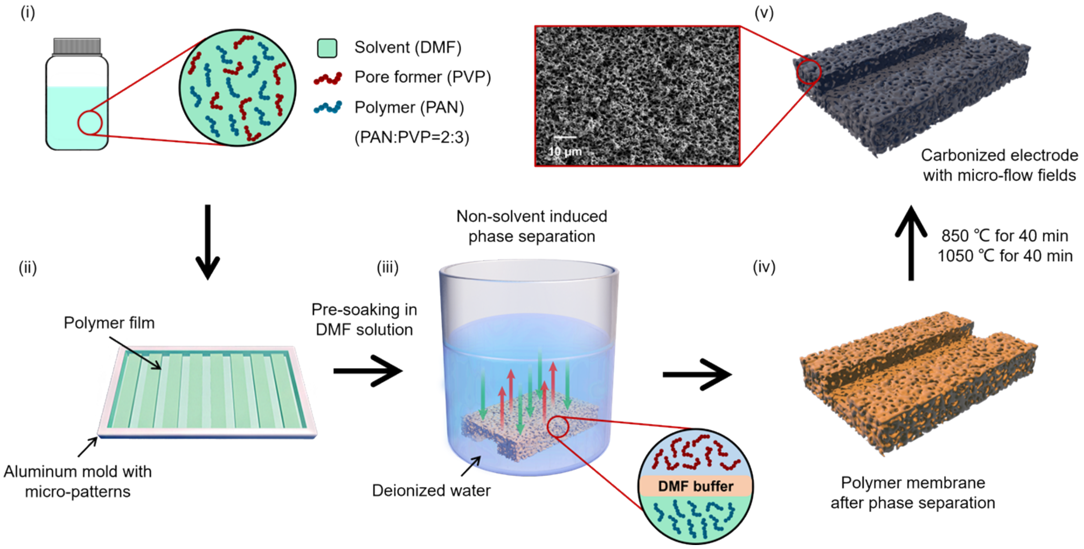

Figure 4.1 Schematic illustration of the fabrication process of the sponge-like NIPS electrodes with micro-flow fields. The major steps include: (i) preparation of the polymer solution with the mixture of PAN and PVP dissolved in DMF; (ii) casting of the polymer solution on aluminum mold with micro-patterns; (iii) immersion of the solution into non-solvent (deionized water) coagulation bath for > 12 h after pre-soaking in DMF solution for 5 s; (iv) removal of pristine membrane from the coagulation bath; and (v) obtaining sponge-like NIPS electrode with micro-flow fields after stabilization and carbonization of the polymer membrane. The SEM image of the sponge-like structure is shown in (v).

4.2 Experimental

4.2.1 Electrode preparation

PAN (Mw ≈ 150,000 Da, Sigma-Aldrich) and PVP (Mw ≈ 1,300,000 Da, Sigma-Aldrich) were added in a 100 mL Pyrex bottle and dissolved in DMF (⩾99.9%, Sigma-Aldrich) solvent. PAN and PVP were selected here as the carbon precursor and pore-foaming agent to obtain ladder-like porous graphitic structure after thermal treatment. The mass ratio of PAN and PVP was selected as 2:3 to ensure balanced pore connection network and surface area based on a previous study [11]. A PTFE magnetic stirring bar was added in the bottle, and the bottle was sealed by parafilm tape to avoid evaporation. It was placed on a hot plate magnetic stirrer at 80 ℃ and mixed at 120 rpm for > 6 h until a clear yellowish solution was obtained. The bottle was placed on a roller bench at room temperature for >12 h to ensure thoroughly homogeneous mixing of the solution and removal of gas bubbles.

Aluminum molds with specific micro-patterns were designed and manufactured. Two different geometric sizes of the groove and pillar patterns were considered in the present study, we prepared four micro-patterned aluminum molds, two for each groove and pillar pattern design. We denote the molds as large and small, i.e., L and S, in the present study. The size of the large mold was 1000 microns for the groove width or pillar diameter, and the size of the small one was 500 microns.

The molds were placed side-by-side in a fumehood. A surplus of the polymer solution was poured into each mold, and the extra solution was spread from one side to the other using a glass slice, while taking care not to introduce air bubbles in the process. After membrane casting, the polymer films along with the aluminum molds were placed into a DMF bath for 5 s to initiate the pre-soaking process, which introduced a thin film of DMF solution on the membrane surface to slow down the demixing process during the phase exchange.

A glass container filled with >3 L of demi-water was used to be the coagulation bath. The polymer films after pre-soaking in DMF, with molds attached, were gently placed horizontally into the container to avoid disrupting the water. After leaving it overnight, the formed solid membrane films were gently separated from the aluminum molds. The membranes were boiled in ultrapure water to rinse away the remaining solvents, PVP, and low-weight PAN. The formed membranes were dried with paper, and then placed between Teflon sheets in a vacuum oven at 80 ^{o}C for overnight. A ceramic block was applied on the top to prevent the membranes from deformation.

After the drying process, the PAN electrodes were placed in a chamber oven for thermal stabilization. This process could help to further solidify the polymer structure, enhancing their mechanical properties. The membranes were placed between alumina paper sheets and ceramic plates, with added weight for uniform compression. They were stabilized in air at 270 °C for an hour and cooled down naturally afterwards.

After stabilization, carbonization was performed. The PAN electrodes were transferred to a tubular oven and heated in a nitrogen environment. The heating process involved a gradual increase from room temperature to 850 °C, holding at this temperature for 45 min, then further raising the temperature to 1050 °C for another 45 min, followed by natural cooling to room temperature. In the end, the PAN electrode sheets were set on a cutting board and divided into smaller sections (1.7 × 1.5 cm^2) using a sharp blade.

4.2.2 Ex-situ characterization

Scanning electron microscopy (JEOL JSM-IT100) was used to capture the microstructure features of the sponge-like NIPS electrodes at a 10 kV acceleration. Mercury intrusion porosimetry (AutoPore IV 9500) was used to capture the pore size distribution using ~100 mg electrode samples at a 5 cm^3 volume penetrometer.

4.2.3 Pressure drop measurement

Pressure drop measurements were carried out to evaluate the pressure drop and electrode permeability. Two pressure sensors were placed at the inlet and outlet of the battery cell, and the working fluid was deionized water for all of the pressure drop tests. The pressure drop of the empty cell (the same battery system without electrodes assembled) was excluded in each test, to make sure the pressure drop obtained was exclusively from the electrodes. The non-linear Darcy-Forchheimer equation [16] was fitted to the obtained pressure drop data to obtain the permeability.

4.2.4 Flow cell electrochemical testing

All the flow cell tests were conducted at room temperature using a cell with the geometric size of 2.55 cm^2. In symmetric iron flow cell tests, $FeCl_2 \cdot 4H_2O$, $FeCl_3 \cdot 6H_2O$, and HCl were mixed in deionized water. The SoC was 50% and the total concentration of the active species was set to 0.5 mol/L dissolved in 2 mol/L hydrochloric acid solution as supporting electrolyte. The membrane used was a FS-950 cation exchange membrane with a thickness of 50 μm. To ensure accurate electrolyte flow rates, the pump was calibrated with ultrapure water at each rate before measurements. Electrode compression was kept between 10% and 20% for all samples. EIS and polarization curves were conducted to evaluate the electrochemical performance at varying linear electrolyte flow velocities. To make comparison for both flow-through and interdigitated flow fields, we used four different linear electrolyte velocities, 1, 2, 5, and 10 cm/s, for both flow-through and interdigitated flow fields. The overall volumetric flow rate for IDFF under the same linear electrolyte velocity is much higher than for a FTFF.

In vanadium full-cell tests, a full-cell setup was used with the geometric size of 2.55 cm^2. The original vanadium electrolytes (OXKEM) consisted of 1.61 mol/L $V^{3.5+}$, 4.05 mol/L SO_4^{2-}, and 0.05 mol/L PO_4^{3-}. Pre-charging of the electrolytes to 50% SoC was conducted before each test. A FS-950 cation exchange membrane with a thickness of 50 μm was used. EIS and discharge polarization curves were collected to evaluate the electrochemical performance.

4.3 Results and discussion

4.3.1 Morphology of the NIPS electrodes with micro-flow fields

After carbonization of the electrodes, SEM was utilized to image the electrode microstructure. The groove and pillar patterns were successfully integrated into the electrode structure. We found that there is a significant degree of electrode shrinkage after the carbonization process. The observed shrinkage ratios in the channel or pillar regions are approximately between 20-25%. The regions between two adjacent channels or pillars demonstrated a higher shrinkage ratio of nearly 50%. Hence, the micro-patterned designs of the original aluminum molds need to consider the shrinkage of electrodes after carbonization. Due to the shrinkage effects, some deformation occurs within the micro-pattern regions, especially for the groove patterns. This also needs to be considered in the design to maintain flatness and good mechanical properties of the electrode.

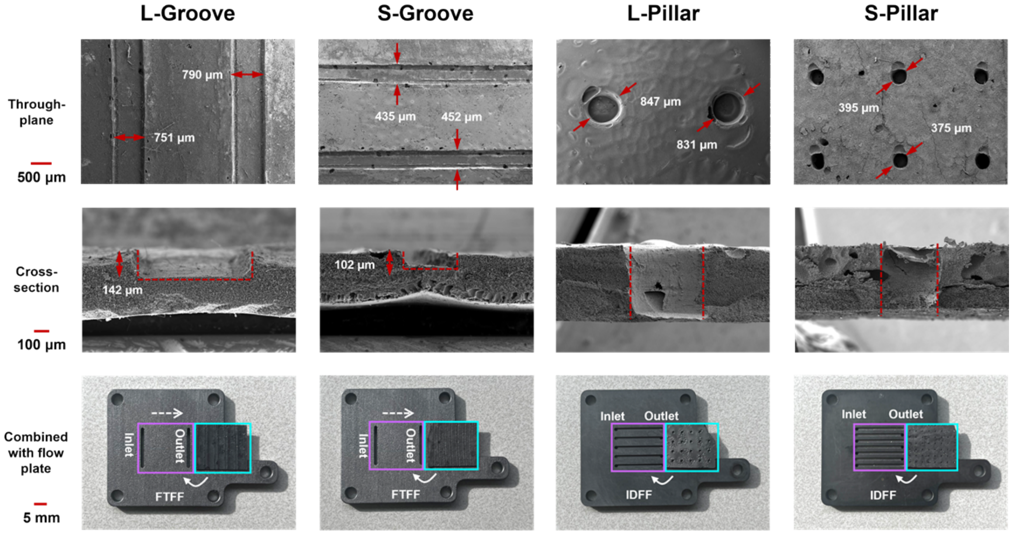

Figure 4.2 Through-plane (top row) and cross-sectional (middle row) SEM images of sponge-like NIPS electrodes with micro-flow fields. The optical photographs of the electrodes with combination of the flow plate are presented in the bottom row. In the present study, the electrodes with micro-groove and micro-pillar patterns are combined with FTFF and IDFF, respectively.

4.3.2 Balance between electrode pressure drop and surface area

From the pressure drop measurement, it can be found that the no pattern sponge-like NIPS electrode exhibits high pressure drop under FTFF, due to the relatively dense structure and the small pore sizes. The electrodes with groove and pillar patterns display a greatly reduced pressure drop both with FTFF and IDFF. Specifically, the permeability results of the L-Groove and S-Groove are ~60% and ~130% increased compared to the no pattern electrodes under FTFF, respectively. Also the L-Pillar and S-Pillar designs yield improved permeabilities by ~90% and ~ 40% as compared to the no pattern electrodes under IDFF, respectively.

Additionally, the electrochemical active surface area (ECSA) was determined through electrochemical impedance spectroscopy (EIS) in a 2 mol/L HCl solution. We used a simplified transmission line model [17] in combination with an series inductor and resistor as the equivalent circuit model to fit for to the data to obtain the double-layer capacitance

[18], which was used to calculate the volumetric specific surface area (α_v). It was found that the α_v for all the sponge-like NIPS electrodes are above 40 m^2/m^3, which is attributed to the small pore size and narrow pore size distribution of the sponge-like NIPS electrodes. The high α_v reduces the kinetic resistance of the electrode, which is the main advantage of this structure. For the groove or pillar patterned electrodes, the α_v is smaller than that of the no pattern electrodes due to the removal of mass from the electrode structure. Hence, the trade-off between electrode pressure drop and surface area needs to be considered when designing the micro-pattern electrodes.

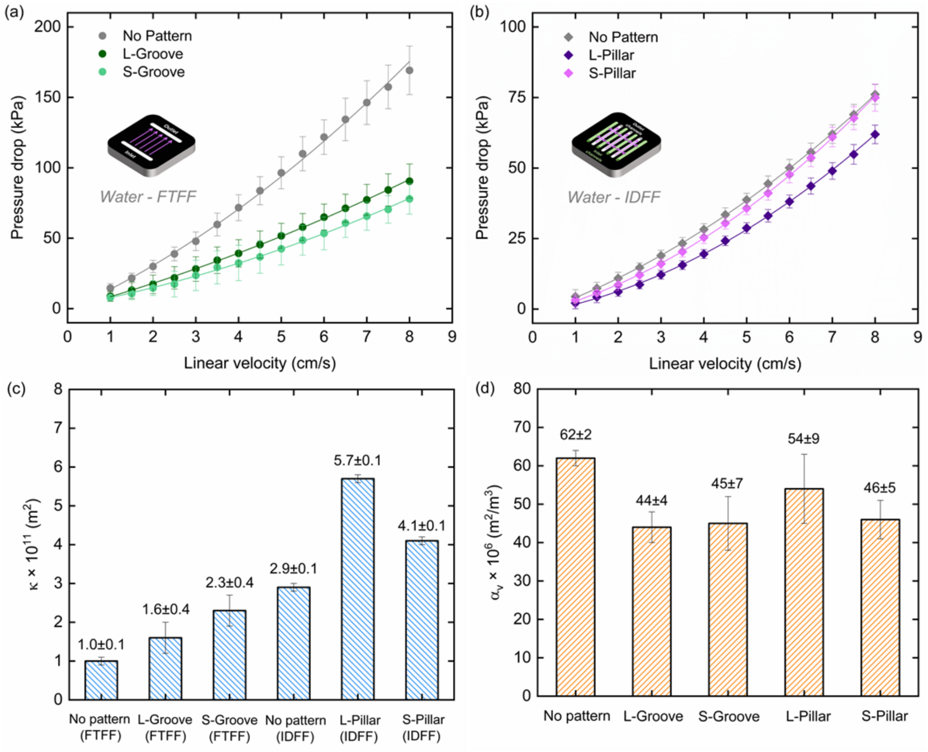

Figure 4.3 Pressure drops (dots) versus linear velocity of the sponge-like NIPS electrodes with (a) micro-groove patterns in FTFF and (b) micro-pillar patterns in IDFF within the single-cell. The fits (lines) are based on the non-linear Darcy-Forchheimer equation. The obtained permeability (κ) results are summarized in (c). (d) Volumetric specific surface area (α_v) obtained through EIS measurements in 2 mol/L HCl solution. The error bars correspond to one standard deviation (n=2).

4.3.3 Performance of the electrodes with micro-groove patterns

For a comparative analysis, we adopted the non-patterned sponge-like NIPS electrode as our reference benchmark and compare the performance of the different electrodes in a flow-through configuration (see fig 4.3 a). For the no pattern structure, the high pressure drop at a velocity of 10 cm/s resulted in electrolyte leakage, hence the results are not presented here. For the other three velocities, we found that the kinetic resistance is very small, which is due to the high surface area of the sponge-like structure. However, the mass transport resistance is very high for the no pattern NIPS electrode even at high flow velocities (up to 5 cm/s).

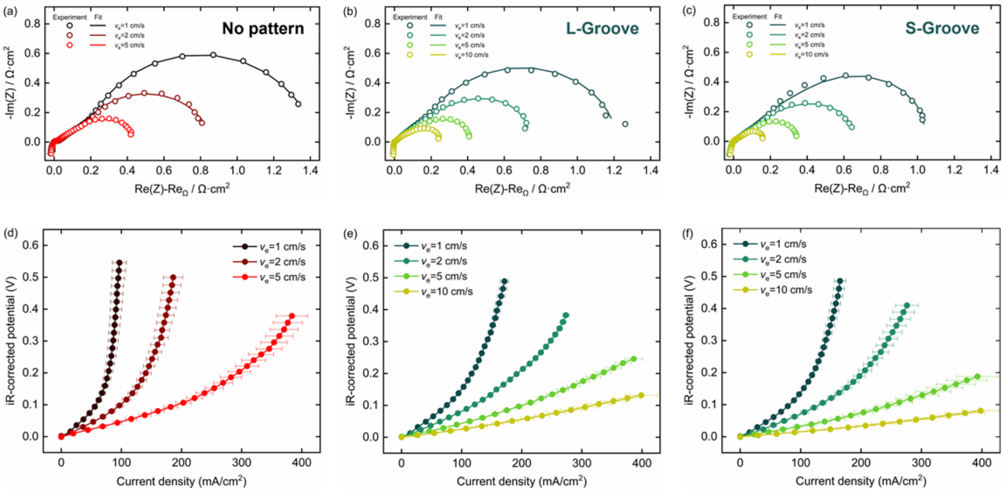

Figure 4.4 Electrochemical performance of the sponge-like NIPS electrodes with micro-grooves in a 0.5 mol/L Fe^{2+}/Fe^{3+} symmetric cell with FTFF. The performance of NIPS with no pattern is presented for comparison. Nyquist plots obtained through EIS measurements (dots) and the fittings (lines) at different electrolyte superficial velocities are shown in (a)-(c). IR-corrected polarization curves are shown in (d)-(f). The error bars in polarization curves correspond to one standard deviation (n=2).

Then we evaluated the electrochemical performance of the electrodes with L-Groove patterns. The grooves were aligned perpendicular to the flow direction in the present study. In the current battery design, there are 4 large grooves within one NIPS electrode. With this design, flow velocities up to 10 cm/s become feasible due to the diminished pressure drop. We also found that in the polarization curves, the mass transport limitation region occurs at higher current densities, which may be a result of the enhanced local mass transfer due to the presence of the grooves.

The performance of the electrode embedded with S-Groove patterns is also evaluated. There are 7 small grooves within one NIPS electrode in the present battery design. The mass transport resistance can be further reduced through the S-Groove patterns.

4.3.4 Performance of the electrodes with micro-pillar patterns

The electrochemical performance of the pillar patterned electrodes combined with IDFF flow plates were evaluated. To make comparison, we also use the no pattern NIPS electrode with sponge-like structure as a reference here. The IDFF designs help to reduce the mass transport resistance compared to the FTFF designs. And the velocity of 10 cm/s is possible here without battery leakage.

The performance of the electrode with large pillar patterns is presented in Fig. 4.5. There are 20 large pillars in the current electrode design. For the alignment of the large pillars between the inlet and outlet channels of the IDFF, we employed IDFF designs with wider rib width of 2 mm. As a result, there are 3 inlet channels and 2 outlet channels in the wide-rib IDFF. Incorporating large pillar patterns in the electrodes substantially reduced the mass transport resistance. Impressively, even at a flow velocity of 1 cm/s, the electrode yields good electrochemical performance in this configuration.

Furthermore, we evaluated the electrode integrated with S-Pillar designs. There are 48 small pillars in the current electrode design. The mass transport resistance is further reduced compared to the large pillars. Notably, the combined resistance from kinetic and mass transport measures less than 0.1 $\Omega\cdot cm^2$ at a linear electrolyte velocity of 10 cm/s.

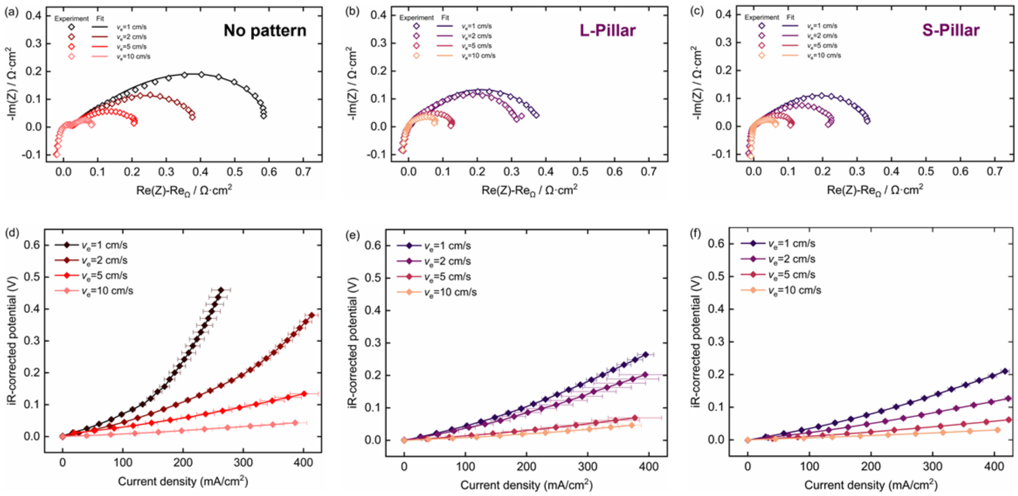

Figure 4.5 Electrochemical performance of the sponge-like NIPS electrodes with micro-pillars in a 0.5 mol/L Fe^{2+}/Fe^{3+} symmetric cell with IDFF. The performance of NIPS with no pattern is presented for comparison. Nyquist plots obtained through EIS measurements (dots) and the fittings (lines) at different electrolyte superficial velocities are shown in (a)-(c). IR-corrected polarization curves are shown in (d)-(f). The error bars in polarization curves correspond to a standard deviation (n=2).

4.3.5 Vanadium full-cell tests

Finally, we selected the best-performing electrode for each design, that is, S-Groove and S-Pillar, and compare the electrochemical performance with a commercial carbon paper electrode (e.g., 2-layer Freudenberg H23) at the electrolyte velocity of 5 cm/s in a vanadium full cell. We can find that pristine carbon paper shows high resistances due to the low active surface area and poor hydrophilicity. The S-Groove electrode with FTFF design has lower overall resistances, and mass transport resistance is the major contribution. The S-Pillar electrode with IDFF design is the best performed combination here. The overall resistance (including an ohmic resistance of 0.46 $\Omega \cdot cm^2$) is less than 0.6 $\Omega \cdot cm^2$, which exhibits < 0.1 V overpotential losses at the current density of 200 mA/cm^2 in the discharge polarization measurement.

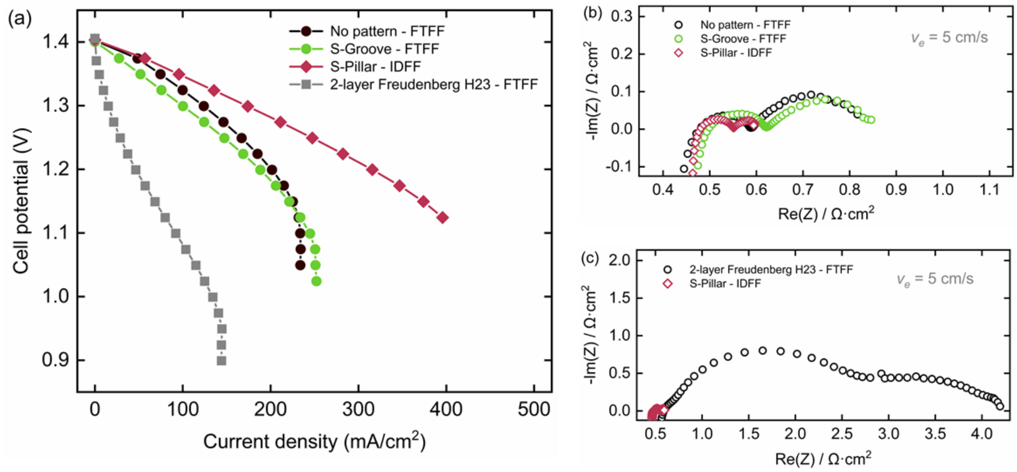

Figure 4.6 Electrochemical performance of sponge-like NIPS electrodes with micro-flow fields in a 1.6 mol/L full-cell vanadium RFB at 50% SoC. Polarization curves are shown in (a), and EIS spectra is shown in (b)-(c). The electrolyte superficial velocity is 5 cm/s.

4.4 Conclusions

In the present study, non-solvent induced phase separation was adopted to prepare sponge-like electrodes. Micro-flow fields including groove and pillar patterns were integrated into the electrode architecture during the phase separation process. The results show that the sponge-like NIPS electrodes possess small pore sizes and narrow pore size distribution, which contributes to the high volumetric specific surface area and a large pressure drop. The electrodes with micro-flow fields facilitate electrolyte penetration yields significantly reduced pressure drop and improved mass transfer. The results show that the electrodes with groove and pillar patterns displayed lower pressure drop and improved mass transfer properties. Specifically, when combined with the IDFF, the pillar-patterned electrodes demonstrate superior electrochemical efficiency, significantly minimizing mass transport resistances. In symmetric iron cell tests with an electrolyte linear velocity of 10 cm/s, the combined resistance for both kinetic and mass transport is below 0.1 Ω·cm^2. Compared to the activated commercial electrode (e.g., 2-layer Freudenberg H23 carbon paper, thermally treated at 450 ^{o}C for 12 h), the ohmic resistance corrected cell resistance was reduced by

~60%, which shows great potential for performance enhancement of next generation RFB reactors.

References

[1] M. Guarnieri, P. Mattavelli, G. Petrone, G. Spagnuolo. Vanadium redox flow batteries: Potentials and challenges of an emerging storage technology. *IEEE Industrial Electronics Magazine*, 10, 20−31 (2016).

[2] J. Noack, L. Wietschel, N. Roznyatovskaya, K. Pinkwart, J. Tübke. Techno-Economic Modeling and Analysis of Redox Flow Battery Systems. *Energies*, 9, 627 (2016).

[3] A. Forner-Cuenca, E. Penn, A. Oliveira, F. Brushett. Exploring the Role of Electrode Microstructure on the Performance of Non-Aqueous Redox Flow Batteries. *Journal of The Electrochemical Society*, 166, A2230–A2241 (2019).

[4] A. Forner-Cuenca, F. Brushett. Engineering porous electrodes for next-generation redox flow batteries: recent progress and opportunities. *Current Opinion in Electrochemistry*, 18, 113−122 (2019).

[5] H. Wang, J. Jung, J. Kim, S. Kim, E. Drioli, T. Lee. A novel green solvent alternative for polymeric membrane preparation via nonsolvent-induced phase separation (NIPS). *Journal of membrane science*, 574, 44−54 (2019).

[6] J. Jung, J. Kim, H. Wang, E. Di Nicolo, E. Drioli, Y. Lee. . Understanding the non-solvent induced phase separation (NIPS) effect during the fabrication of microporous PVDF membranes via thermally induced phase separation (TIPS). *Journal of Membrane Science*, 514, 250−263 (2016).

[7] I. Maggay, M. Yu, D. Wang, C. Chiang, Y. Chang, A. Venault. Strategy to prepare skin-free and macrovoid-free polysulfone membranes via the NIPS process. *Journal of membrane science*, 665, 120597 (2022).

[8] D. Wang, J. Lai. Recent advances in preparation and morphology control of polymeric membranes formed by nonsolvent induced phase separation. *Current Opinion in Chemical Engineering*, 2, 229−237 (2013).

[9] C. Wan, R. Jacquemond, Y. Chiang, K. Nijmeijer, F. Brushett, A. Forner-Cuenca. Non-Solvent Induced Phase Separation Enables Designer Redox Flow Battery Electrodes. *Advanced Materials*, 33, 2006716 (2021).

[10] C. Yang, G. Zhu, Z. Yi, Y. Zhou, J. Gao. Critical contributions of additives on the fabrication of asymmetric isoporous membranes from block copolymers: A review. *Chemical Engineering Journal*, 424, 128912 (2021).

[11] R. Jacquemond, C. Wan, Y. Chiang, Z. Borneman, F. Brushett, K. Nijmeijer, A. Forner-Cuenc. Microstructural engineering of high-power redox flow battery electrodes via non-solvent induced phase separation. *Cell Reports Physical Science*, 3, 7 (2022).

[12] C. Wan, R. Jacquemond, Y. Chiang, A. Forner-Cuenca, F. Brushett. Engineering Redox Flow Battery Electrodes with Spatially Varying Porosity Using Non-Solvent-Induced Phase Separation. *Energy Technology*, 11, 2300137 (2023).

[13] X. Ke, J. Prahl, J. Alexander, J. Wainright, T. Zawodzinski, R. Savinell. Rechargeable redox flow batteries: flow fields, stacks and design considerations. *Chemical Society Reviews*, 47, 8721−8743 (2018).

[14] J. Sun, M. Zheng, Y. Luo, Z. Yu. Three-dimensional detached serpentine flow field design for redox flow batteries. *Journal of Power Sources*, 428, 136–145 (2019).

[15] S. Tsushima, T. Suzuki. Modeling and simulation of vanadium redox flow battery with interdigitated flow field for optimizing electrode architecture. *Journal of The Electrochemical Society*, 167, 020553 (2020).

[16] K. Tenny, A. Forner-Cuenca, Y. Chiang, F. Brushett. Comparing Physical and Electrochemical Properties of Different Weave Patterns for Carbon Cloth Electrodes in Redox Flow Batteries. *Journal of Electrochemical Energy Conversion and Storage*, 17, 041010 (2020).

[17] J. Landesfeind, J. Hattendorff, A. Ehrl, W. Wall, H. Gasteiger. Tortuosity Determination of Battery Electrodes and Separators by Impedance Spectroscopy. *Journal of The Electrochemical Society*, 163, A1373–A1387 (2016).

[18] J. Brug, A. van der Eeden, M. Sluyters-Rehbach, J. Sluyters. The analysis of electrode impedances complicated by the presence of a constant phase element. *Journal of Electroanalytical Chemistry and Interfacial Electrochemistry*, 176 (1984) 275–295.

Chapter 5

Conclusion and Outlook

5.1 Conclusion

The work presented in this thesis is centered around the engineering of high-performance porous electrodes for next-generation low-cost redox flow batteries. The key findings are summarized as follows:

- The relationship between electrode microstructure and battery performance was investigated based on three representative carbon-fiber, binder-free electrodes (i.e., felt, paper, and cloth) under a practical battery compression region of 0-50% CRs. We found that for the carbon cloth, pore compression mainly occurred under the large pores at intersections between fiber bundles. The permeability was reduced from 2.1×10^{-10} m^2 at 0% CR to 2.7×10^{-11} m^2 at 50% CR as the result of the deformed pores and tortuous electrolyte pathways under applied compression. For the vanadium full-cell RFB performance, the optimal balance of the highest achievable current density extracted at the overpotential of 50 mV through iR-corrected polarizations) and satisfactory pressure drop for the felt, paper, and cloth came about at 30%, 20% and 20% CR, respectively. Under moderate compression, the cloth presented a good balance between the electrochemical performance and pressure drop. It maintained >85% VE under 120 mA/cm^2 at the CR of 20% with low pump consumption.
- In the dual-layer electrode configuration with the combination of carbon cloth and carbon paper, carbon cloth was placed adjacent to the flow field, which led to efficient mass transfer of reactant to the sub-layer of carbon paper at a low pressure drop. The local flow distribution was simulated using LBM and it was found that the flow velocity is higher within the large channels of the carbon cloth. From electrochemical tests in a symmetric vanadium flow cell, it was shown that the enhanced performance of the dual-layer electrode configuration in a full-cell RFB was due to a decrease of

both the mass transport and kinetic overpotentials of the V^{2+}/V^{3+} redox couple. We also found that the carbon paper placed adjacent to the membrane avoided deep electrode imprints from carbon cloth on the 10-micron m-PBI membrane used in the present study.

- Due to the flexibility of the NIPS electrode manufacturing, it provides an opportunity to integrate micro-flow field channels into the electrode architecture. A sponge-like NIPS electrode with high surface area was fabricated through delayed demixing during the phase exchange process. The performance and pressure-drop of micro-patterned designs (i.e., groove and pillar) with two different feature sizes were tested with FTFF and IDFF, respectively. It was found that the pristine sponge-like NIPS electrodes possessed small pore size (e.g., ~1 μm) and a narrow pore size distribution. The major contribution to the overall losses came from the mass-transfer resistance. The electrodes with groove and pillar patterns displayed reduced pressure drop and improved mass transport properties. Pillar-patterned electrodes in combination with IDFF presented the highest overall electrochemical performance with a combined kinetic and mass transfer resistance of less than 0.1 $\Omega \cdot cm^2$ in symmetric iron flow cell tests.

5.2 Outlook

The findings of this thesis provide some guidance for future studies. Possible directions could be:

- In this thesis, thermal pre-treatment methods with single temperature and duration time (400 °C for 24 h) were used for all the electrodes used in **Chapter 2** and **Chapter 3** before flow cell assembly. We noticed a tremendous increase of the BET surface area for the carbon paper electrode (i.e. Freudenberg H23) after thermal treatment. A much smaller increase was observed for carbon felt and cloth electrodes. This may be due to the different carbonization or graphitization degrees during the manufacturing process for these electrodes, which needs further exploration to understand the thermal etching better and to find optimal etching conditions.

- In **Chapter 3**, we employed LBM to simulate the flow distribution and velocity profile within the DL electrode configurations. The present simulation is considered to be only qualitative due to the relatively small simulation volume used, which leads to a risk of significant edge-effects. Larger simulation volumes are needed for a more accurate model to carefully match the boundary conditions with practical experiments. Also, in **Chapter 4**, similar validated simulations are needed to provide detailed insight into the local flow distributions of the pillar and groove regions in the NIPS electrodes to understand the origin of the improved performance of these electrodes.

- In this thesis, all the electrochemical tests were performed in a lab-scale RFB set up with the active geometric area of 5 or 2.55 cm^2. A scale-up process (e.g., to 100 cm^2) for fabrication of the NIPS electrodes in **Chapter 4** with appropriate mechanical properties should be considered in a future study. Also, design pathways with co-optimized flow field and electrode architecture from lab-scale toward large-scale RFBs need further investigation.